Waves in Solar Atmosphere and their Role in Dynamics of the Corona

A Thesis

Submitted for the Award of the Degree of

Doctor of Philosophy (Science)

To

Jadavpur University

by

Ajanta Datta

Indian Institute of Astrophysics,
Bangalore 560 034.

Department of Physics,
Jadavpur University,
Kolkata 700 032.

May 2017

CERTIFICATE FROM THE SUPERVISORS

This is to certify that the thesis entitled **'Waves in Solar Atmosphere and their Role in Dynamics of the Corona'** submitted by **Mrs. Ajanta Datta**, who got her name registered on **09/05/2012 (Index no. 81/12/Phy/21)**, for the award of Ph.D. (Science) degree of Jadavpur University, is absolutely based upon her own work under the supervisions of Prof. Dipankar Banerjee and Prof. Subhankar Ray and that neither this thesis nor any part of it has been submitted for either any degree/diploma or any other academic award anywhere before.

D. Banerjee

.....

(Signature of the Supervisor,
date with official seal)

Prof. Dipankar Banerjee

Indian Institute of Astrophysics,
Bangalore 560 034.
email:dipu@iiap.res.in

Subhankar Ray

.....

(Signature of the Supervisor,
date with official seal)

Prof. Subhankar Ray

Department of Physics,
Jadavpur University,
Kolkata 700 032.
email:sray.ju@gmail.com

भारतीय तारकीकी संस्थान
INDIAN INSTITUTE OF ASTROPHYSICS
विज्ञान और प्रौद्योगिकि विभाग
DEPARTMENT OF SCIENCE & TECHNOLOGY
भारत सरकार GOVT OF INDIA
कोरमंगला KORAMANGALA
बेंगलौर BANGALORE-560 034
भारत INDIA

Department of Physics
Jadavpur University
Kolkata-700 032

Declaration of Authorship

I, Ajanta Datta (Index no. 81/12/Phy/21, registered on 09.05.2012), hereby declare that the matter contained in this thesis is the result of the investigations carried out by me at Indian Institute of Astrophysics, Bangalore, and at Department of Physics, Jadavpur University under the supervision of Profs. Dipankar Banerjee and Subhankar Ray. This work has not been submitted for the award of any other degree, diploma, associateship, fellowship, etc. of any other university or institute.

Signed:

Date:

Dedicated to

my mother and my daughter

Acknowledgements

This is a small note expressing my gratitude to all who believed in me, more than I do. This thesis would not be possible without their constant encouragement and support.

I express my deepest gratitude to my supervisors Prof. Dipankar Banerjee and Prof. Subhankar Ray. I am indebted to Prof. Dipankar Banerjee for his constant support and encouragement. It is challenging, starting research after a long gap. But, his friendly and patient approach made it possible to overcome this. My special thanks are due to Prof. Subhankar Ray. His teaching, advice and encouragement have been of much value to my work.

I thank the authorities of Indian Institute of Astrophysics (IIA) and Jadavpur University (JU) for providing me all the necessary facilities for my research work.

I thank the Chairman, the Director and successive Principals Dr. T.C. Manjunath and Dr. C.K. Chaitanyakumar, of my college, HKBK College of Engineering for permitting me to do Ph.D. under QIP programme and providing a weekly off-day to visit IIA. I cordially thank my all colleagues at HKBK College of Engineering for a comfortable working environment. I specially thank, Dr. Chandra Kumar K., the head of our department for his encouragement and help, as and when needed.

It is a wonderful experience to be a member of a team which is full of young and enthusiastic people. I thank all the members of *'Dipu-gang'* of IIA, for their instant and continuous help. It was a pleasure to work with Krishna, Vaibhav, Sudip, I have learned a lot from these young friends. I wish them all success in their life.

I gratefully acknowledge for helps I received from Balai, Pijush, Smaranika, Subhra at Kolkata. I also thank all my friends at JU. I thank Indranath specially, for his numerous help at the beginning. I express my gratitude to Ramakrishna Mission

Institute of Culture, for providing a comfortable accommodation in a peaceful environment during my course work.

I also wish to convey my regards to Prof. Chanchal Uberoi of Indian Institute of Science, under whom I had opportunity to develop the research aptitude.

I am indebted to my mother, who has always taught me to give my hundred percent and not to compare my achievements with others.

I am blessed and honored to raise my daughter, Ipsita. I thank her for her encouragement. Her *'go Maa'* has motivated me like nothing else. I am proud of everything she is and everything she will be.

And last but not the least, I would like to thank my husband, Basudeb. I can't thank him enough for his constant support, encouragement, motivation during all ups and downs of this journey.

I thank once again all for supporting me in the most ambitious endeavour of my life.

List of Publications

1. Propagating disturbances along a coronal loop from simultaneous EUV imaging and spectroscopic observations
   Ajanta Datta, S. Krishna Prasad, Dipankar Banerjee, 2015, *Research in Astronomy and Astrophysics*, **15(7)**,1027-1035.

2. Flows and waves in braided solar coronal magnetic structures
   V.Pant, **A.Datta**, D.Banerjee, 2015, *The Astrophysical Journal Letters*, **801**, L2

3. Twisting and untwisting motion during a prominence eruption as seen from SDO/AIA and STEREO/EUVI
   V.Pant, **A.Datta**, D.Banerjee, K. Chandrashekhar, S. Ray, 2016, under review with *The Astrophysical Journal*

4. Statistical study of frequency dependent damping of magneto-acoustic waves
   A.Datta, S.Mandal, S.Ray, D.Banerjee, 2017, in preparation.

Abstract

Solar atmosphere is stratified and exhibits dynamic structures with confined hot plasmas. The corona consists of dynamic magnetic structures, in the form of closed and open loops with an enhanced plasma density. Moreover, these elastic and compressible structures support different types of waves, playing the role of the wave guide. The waves can be described using magnetohydrodynamics (MHD).

In this thesis, we detect and study propagating disturbances (PDs) along active region loops using simultaneous imaging and spectroscopy. An image sequence recorded in Fe IX/Fe X 171Å channel, from *Transition Region and Coronal Explorer* (TRACE) and spectral data in the different extreme ultraviolet (EUV) lines obtained from *Coronal Diagnostic Spectrometer* (CDS) are analysed. Space-time map constructed from the TRACE image sequence shows the presence of PDs close to the loop foot point propagating with an apparent speed of 39 km s^{-1} along an active region loop in an off-limb position. Wavelet analysis confirms the periodicity is equal to 5.4 min. The corresponding spectroscopic data from CDS, at a location away from the foot point, show oscillations in all three line parameters roughly at the same period. At locations farther from the foot point, the line width oscillation seems to disappear while the Doppler velocity oscillation becomes prominent. We attribute this to the signature of propagating slow waves that get affected by flows/other events close to the foot point. We detect PDs in other loops from simultaneous observations by TRACE and CDS/-SOHO. The spectroscopic observations confirm the presence of PDs in the transition region, as well as in the corona. From the phase relationship of oscillations in intensity and Doppler velocity, we identify these PDs as magneto-acoustic waves.

PDs dissipate as they travel along the supporting structure. Different mechanisms are responsible for such dissipation, like thermal conduction, compressive viscosity, area stratifiction, optically thin radiation and gravitational stratification. Dissipations due to thermal conduction and compressive viscosity depend on the frequency of the PDs. We identify PDs along polar plumes and interplumes. We find the damping lengths of PDs of various periodicities and perform a statistical study of frequency dependency of

damping length and compare the observed variations with the theoretical predictions. We found that thermal conduction may not be the major contributor in damping.

The other well accepted mechanism of coronal heating is impulsive heating by nanoflares ((Parker 1988)). Nanoflares are defined as localized impulsive bursts of $5 - 100$ s duration. The random movements of footpoints of bipolar fields create tangential discontinuities, which are destroyed by rapid reconnection of magnetic fields. Hence, the bipolar fields above the surface of the sun are filled with nanoflares. We study the high frequency dynamics in the braided magnetic structure of an active region (AR 11520) moss as observed by High-Resolution Coronal Imager (Hi-C). We detect quasi periodic flows and waves in these structures. We search for high frequency dynamics while looking at power maps of the observed region. We find that shorter periodicities (30 - 60 s) are associated with small spatial scales which can be resolved by Hi-C only. We detect quasi periodic flows with a wide range of velocities from 13 - 185 km s^{-1} associated with the braided regions. This can be interpreted as plasma outflows from reconnection sites. We also find presence of short period and large amplitude transverse oscillations associated with the braided magnetic region. Such oscillations could be triggered by reconnection or such oscillation may trigger reconnection.

Prominences and/or filaments are ubiquitous in the solar corona. They manifest as cool plasma structure embedded in the hot corona. Prominences have different properties which are primarily based on the magnetic structure of the region in which they are formed. Prominences can remain stable for a long time. Depending on different parameters like a twist in the magnetic field, mass loading and ambient magnetic field they become unstable and erupt. Prominence eruptions are usually associated with Coronal Mass Ejections (CMEs), which are huge eruptions of plasma and magnetic field into heliosphere and are the main cause of geomagnetic disturbances (see Parenti (2014) and references therein). We report and analyse twisting and untwisting motions of different parts of a prominence during and after eruption. We find that small scale twists of prominence legs propagate along the spine and initiate roll motion. We also follow the evolution of background loops and interpret its role in prominence eruption. We find that the prominence threads untwist and the twist propagates upward with the speed of $\sim$ 83 kms^{-1}. We also estimate the lower value of twist to be $\sim 4\pi$, which is enough to destabilise the prominence. We analyse the CME associated with

this prominence and find the signatures of the twist being carried away.

Contents

List of Figures

List of Tables

Chapter 1

Introduction

The Sun, our nearest stellar neighbour, has awed us since ancient time. As the origin of life and energy, the Sun is described in Rig Veda as: "All that exists was born from Surya, the God of gods." Understanding the Sun from scientific perspective have started with Galileo and have made a long and captivating journey since then. The study of the Sun reveals the origin of solar energy and effect of different solar events in earth's atmosphere.

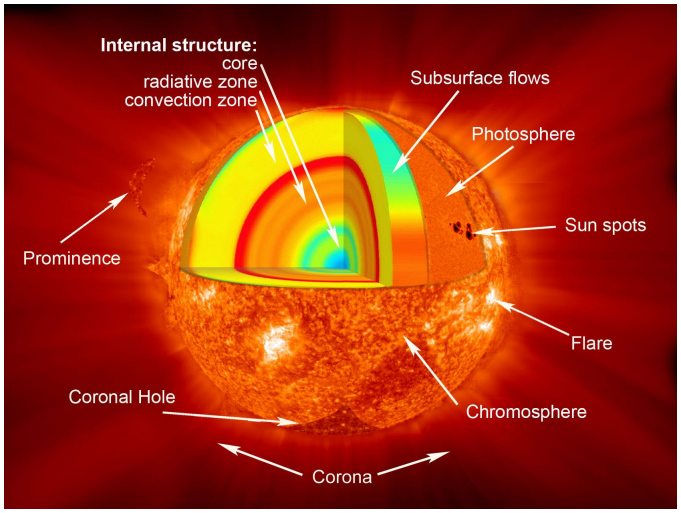

FIGURE 1.1: Layers of solar atmosphere along with different structures. The cut-out portion shows the different layers of solar interior. *Image Credit: NASA/Jenny Mottar*

1.1 Solar atmosphere

The innermost part of the Sun is the core. Energy of the Sun is generated in this region by nuclear fusion. This energy is transported first by radiation and then by convection to the surface. The layers above the Sun's surface constitute the solar atmosphere. It comprises three layers, namely photosphere, chromosphere, and corona (Fig. 1.1). Density, temperature, magnetic field strength and structure vary considerably from one layer to another.

The first layer of the solar atmosphere is known the photosphere, which is extended to a height of about 400 km above the solar surface. Bright granules and supergranules are cell like structures of size $\approx$ 100 km to 1000 km and 30000 km respectively, visible in the photosphere. Sunspots are region of strong magnetic field, which appear dark as the strong magnetic field prevent convection of hotter material to the surface.

The chromosphere is the next layer. Starting at the height of 400 km, it continues till about 2100 km. Spicules and prominences are seen in this layer. Spicules are jet-like structures with lifetime of the orders of minutes. They eject materials to the corona at a speed of about 20 - 30 kms^{-1}. Prominences are dense cloud as extended above the surface. These structures remain for few days (active prominences) to few months (quiescent prominences) before eruption.

Above the chromosphere, the outermost layer, the corona extends over millions of kilometer. The thin layer between cool, dense chromosphere and hot, thin corona is known as the transition region. The temperature variation through these layers are intriguing. The temperature of the photosphere is 6000 K at the bottom and then drops to 4000 K at the top of the layer. Then onwards the temperature increases gradually through the chromosphere and steeply through the thin transition region to $\approx 10^6$ K at the corona (left panel of Fig. 1.2). Due to the low density of the corona, approximately 10^{-4} fraction of the Sun's total energy output is sufficient to maintain the temperature of the corona. But the mode of transportation and mechanism of efficient dissipation of the energy are still a matter of debate and

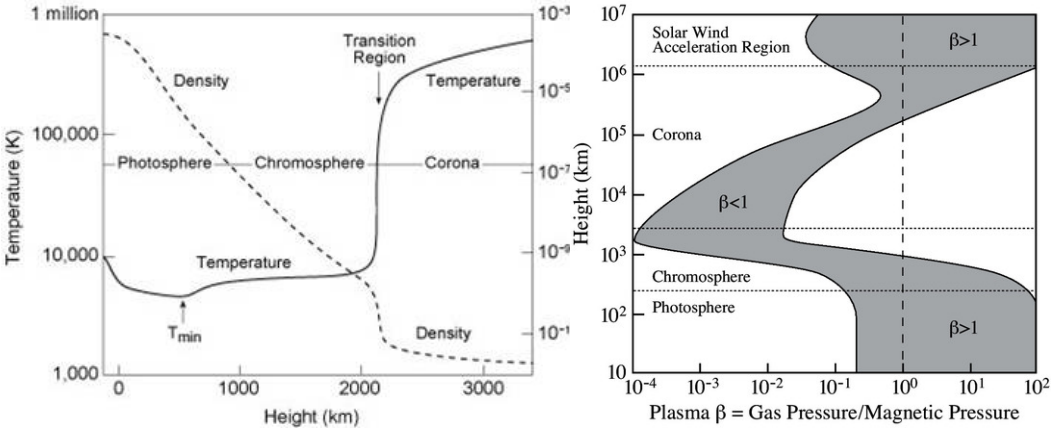

FIGURE 1.2: (*left panel*) Variation of temperature and density through solar atmosphere, (*right panel*) variation of plasma β with height.

known as the coronal heating problem.

1.2 Solar Corona

The corona is the hottest and largest part of the solar atmosphere. Plasma β, i.e. the ratio of the gas pressure to the ratio of the magnetic pressure is usually very small for this region (right panel of Fig. 1.2). So, this region is magnetic field dominated and can be considered as force free. The solar coronal plasma is mainly fully ionized hydrogen with concentration $\approx 10^{15}$ m^{-3}. Hence, corona is observed by spectral lines of highly ionized calcium or iron. Magnetic field in the corona is estimated to be $\approx$ 1 - 40 G, depending on the regions. Coronal plasma is gravitationally stratified with a characteristic distance of about 50 - 60 Mm.

The study of corona is important to answer key fundamental questions, namely the coronal heating problem, acceleration of solar wind and, enormous energy and mass release during Coronal Mass Ejection (CME). Historically, corona is observed during solar eclipses with ground based telescopes. But, such events are rare and durations are short. Apart from this, ground based observations are affected by scattering and absorption due to Earth's atmosphere. With the advent of many space based observatories, now corona is studied with UV, EUV and X-ray telescopes and white light coronagraphs of space based observatories.

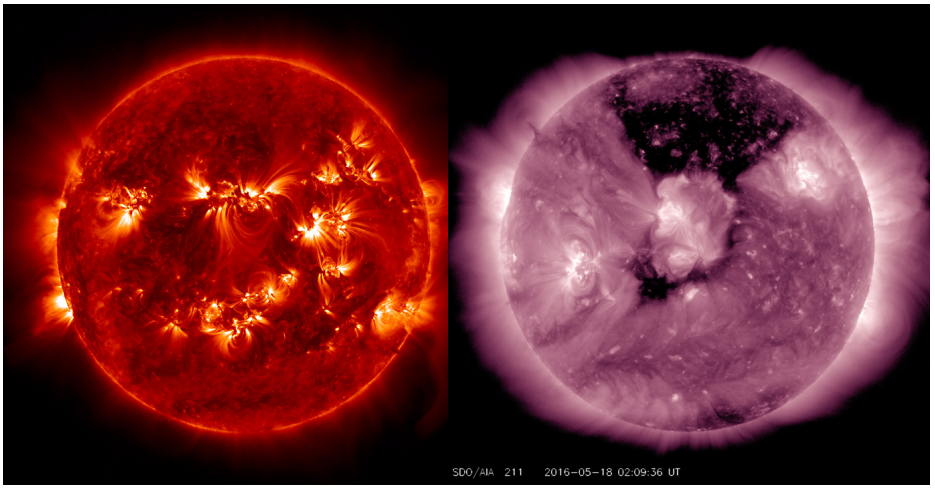

FIGURE 1.3: (*left panel*) Coronal active regions showing closed magnetic fields. Plasma follow the magnetic field and appear bright when viewed in extreme ultraviolet (EUV), and (*right panel*) Dark coronal hole as viewed in EUV. *Image credit: Solar Dynamics Observatory*/NASA.

1.2.1 Coronal Dynamics in Different Scales

The corona consist of different types of structures, which vary widely in length scale and time scale. The corona can be divided into three major regions, active regions, coronal holes and quiet sun region (Fig. 1.3). Active regions are dominated by closed magnetic field structures. These structures expand in the corona to a height of few tens to few hundreds of Mm and then turn back to solar surface. Coronal loops are believed to follow these magnetic fields (Fig. 1.4). The temperature and density of the loop plasma are higher than the inter-loop region plasma. The typical life time of coronal loops is from a few hours to a day. However, the active regions live much longer. Apart from coronal loops, there are hot, fuzzy moss regions. These regions can be observed by instruments having high spatial and time resolution. Coronal holes are dominated by open magnetic structures. These regions are comprised of hot and rarefied plasma. Plumes are seen in polar coronal holes. These bright quiescent structures follow the open magnetic fields. They are observed up to a height of ten or more solar radii and remain unchanged for days. Photospheric unipolar magnetic regions are the origins of plumes. Another type of open structure, formed by magnetic fields of opposite polarities, are known as streamers. The quiet sun region comprise a mixture of both, closed and open magnetic field regions. Apart from these, there are jets of various scales and speeds,

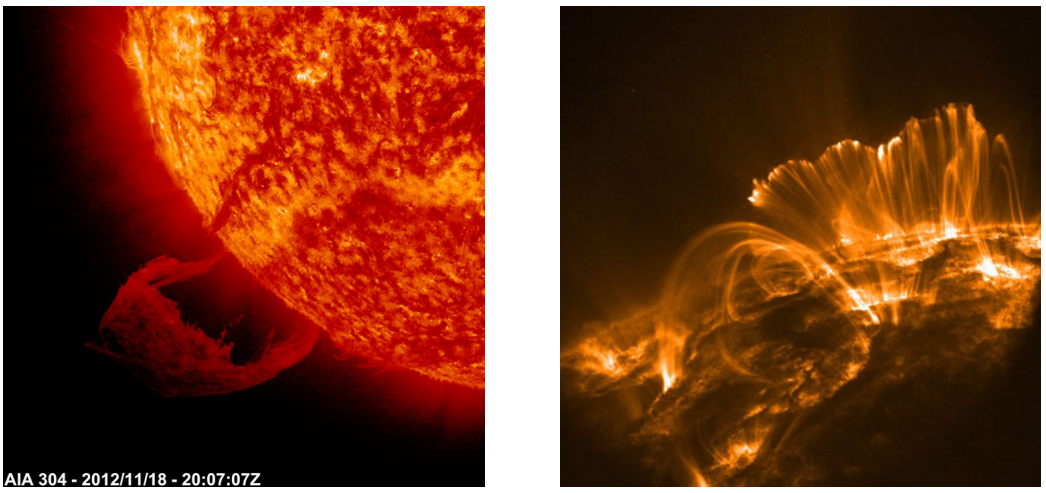

FIGURE 1.4: (*left panel*) Prominence appeared bright when viewed in AIA 304 Åchannel, and (*right panel*) bright coronal loops as viewed in AIA 171 Å. *Image credit: Solar Dynamics Observatory*/NASA.

and prominences in the corona (Fig. 1.4). Prominences are 100 times cooler and denser than the surrounding hot coronal plasma. These thermally isolated system have a unique role in coronal dynamics. Promineces have life time of few days to few months, after that they dissappear due to slow decay or by sudden eruption caused by some instabilties. Flare activities and coronal mass ejections (CMEs) can be associated with prominence eruption (Gopalswamy *et al.* 2006; Martin 1980)).

1.2.2 Waves in Solar Corona

Different types of waves are supported in the corona due to the presence of elastic and compressible plasma. As the plasma β of corona is very low (left panel of Fig. 1.2), the waves in this magnetically dominated plasma can be explained by Magnetohydrodynamics (MHD). These waves have time periods from few seconds to several minutes and plasma density, temperature, bulk velocity, and frozen in magnetic field are perturbed due to these waves. There are two characteristic speeds associated with MHD waves depending on the magnetic field B_0, plasma density ρ_0 and gas pressure p_0. These are the local sound speed $C_s = (\gamma p_0/\rho_0)^{1/2}$, and Alfvén speed, $C_A = B_0/(\mu_0\rho_0)^{1/2}$.

There are three basic MHD waves: Incompressible Alfvén waves with speed equals to Alfvén speed, Compressible fast magnetoacoustic wave with speed greater than C_s and slow magnetoacoustic wave with speed lower than C_s (Priest 1984). Detection and study of these waves have immense importance in understanding the coronal dynamics. Informations of different parameters of MHD waves, periods, wavelength, amplitude, speed etc. combined with theoretical modeling of wave phenomena, lead to determination of mean parameters of the corona (Nakariakov and Verwichte 2005). Not only as a tool, MHD waves have a vital role in coronal dynamics also. The photospheric perturbations propagate as MHD waves through the magnetic flux tubes, as these are excellent wave guide. The dissipation of MHD waves demands special attention. These waves couple with each other, resonantly interact with coronal loops or can form shock waves. Dissipation of MHD waves is accepted as one of the mechanisms of coronal heating.

1.3 Motivation and Outline of the Thesis

Different coronal structures and phenomena vary widely in their length and time scales. They have various roles in complex coronal dynamics and each of them are important in their own way. In this thesis, we have studied few such coronal phenomena and tried to justify their roles in diverse dynamics of the corona.

Slow propagating intensity disturbances (PDs) is one of the examples of coronal wave activities. Propagating intensity disturbances were first observed by Ofman *et al.* (1997), in polar plumes using white light channel of SoHO/UVCS. Using EIT/SoHO, Deforest and Gurman (1998) found such disturbances in coronal plumes. These quasi periodic disturbances of periodicities 10 - 15 minutes, are found to be propagating outwards with projected speed of 75 - 150 km s^{-1}. Such disturbances were observed later along active region loops (Berghmans and Clette 1999). De Moortel *et al.* (2002) showed PDs along loops in the sunspot region have 3 min periodicity, whereas non sunspot region loops show mainly 5 min periodicity. There are many such observations using data from imaging telescope

TRACE. The average periodicity was found to be about 5 min and average propagation speed about 100 km s^{-1}. These studies suggested these PDs are due to slow magnetoacoustic waves. Later, Wang *et al.* (2009a) detected these oscillations as simultaneous variations in intensity and Doppler shift, using spectroscopic data from EIS. The in-phase oscillations of intensity and Doppler shift confirmed their magnetoacoustic nature. But a new debate about the nature of this PDs started as the spectroscopic data revealed oscillations in line width along with intensity and Doppler shift (De Pontieu and McIntosh 2010). They demonstrated that this is due to quasi periodic upflows. Verwichte *et al.* (2010) showed slow waves also could be the cause of such oscillations in line width. These indicate that a study using combined data from imaging and spectroscopic observations would be more appropriate for a more conclusive identification of PDs. In this context, we have studied PDs using imaging and spectroscopic observations. We have emphasized to identify their true nature and also their nature of propagation through different layers of solar atmosphere. These results are presented in the Chapter 3.

Coronal heating problem is one of the longest puzzle in solar physics. Most widely accepted mechanisms of coronal heating are dissipation of waves and magnetic reconnection. Photospheric drivers displace the foot point of loop and hence a magnetic twist builds up. The twist dissipates resulting heat due to reconnection. As the time scale of loop displacement is much longer than the Alfvén time scale, this is considered as DC (Direct Current) mechanisms. On the other hand, if driver displaces the loop foot point in a shorter scale, waves are generated. These waves dissipate resulting heating of the corona. This mechanism is known as AC (Alternating Current) mechanism. These mechanisms are the motivations of our next studies.

Polar plumes are open magnetic field structures extended radially outward. Propagating slow waves are found in this structures. Apart from coronal heating, these waves play a role in accelerating the solar wind. These waves decay as the propagate along the guiding structures due to various reasons, thermal conduction and gravitational stratifications are two main factors. It has been observed that the damping length depends on frequency (Krishna Prasad *et al.* 2014). Coronal holes are considered as the source of solar wind acceleration. We have chosen several

plume and interplume structures near coronal holes and studied the damping of slow waves along these structures. In Chapter 4 we have explored the frequency dependence damping of slow waves.

Impulsive heating by nanoflares (Parker 1988) during reconnection is another well accepted mechanism of coronal heating. Nanoflares are defined as localized impulsive bursts of 5-100 s duration. The random movements of footpoints of bipolar fields create tangential discontinuities, which are destroyed by rapid reconnection of magnetic fields. Hence, the bipolar fields above the surface of the sun are filled with nanoflares. Cargill and Klimchuk (2004) has extended this nanoflare model considering the coronal loops consist many small strands. High frequency waves may play a significant role in coronal heating (Porter *et al.* 1994). In spite of early prediction of existence of high frequency ($\approx$ 1 Hz) intensity oscillations (Ionson 1978), unavailability of observation with high time resolution hindered their detection. High frequency intensity oscillations are reported from ground based observations of high time resolution (Pasachoff and Landman 1984; Singh *et al.* 1997). From the images of solar corona in the Fe XIV and Fe X lines, recorded during solar eclipse, Singh *et al.* (2009) reported intensity oscillations of 20 s and 27 s periodicity. Using the high cadence ($\approx$ 3.14 s) observations of the extreme-ultraviolet imaging spectrometer (EIS) on board the Hinode O'Shea and Doyle (2009) found oscillations of the range $2 - 154$ mHz in active region. Higher frequency oscillations are found to be concentrated near the edge of the plage areas. Recently Hi-C rocket experiment observed an active region moss in an EUV channel centered at 193 Å, with high spatial and time resolution. With newly developed image enhancing method, we have studied a braided region to detect high frequency longitudinal and transverse oscillations. The results of this study is presented in the Chapter 5.

Prominences are ubiquitous in corona. These cool structures are embedded in hot corona. They are observed as bright structure when observed in chromospheric lines and dark when observed in coronal lines. Historically prominences are referred as filaments when observed at an on disk position. Prominences are classified, based on the regions they are found, as polar crown prominences, active region prominences, quiescent prominences, intermediate prominences (Parenti

2014). Different parameters, e.g. ambient magnetic field, twist in the magnetic field, mass loading can make prominences unstable and cause prominence eruption. Prominence eruptions are usually associated with Coronal Mass Ejections (CMEs), which are huge eruptions of plasma and magnetic field into heliosphere and are the main cause of geomagnetic disturbances (see Parenti 2014; **?**, and references there in). The most probable initial signature of a CME is a fluxrope (FR). FR's are twisted magnetic field structure embedded in a dark coronal cavity (Fan and Gibson 2003; Fan 2010; Filippov *et al.* 2015; Gibson *et al.* 2006; Reeves *et al.* 2012). Coronal cavities are difficult to observe as they are surrounded by bright coronal loops. They are visible only if the axis is directed along the line of sight.

Cool prominence materials can be accumulated in the helical flux tubes, so to study prominence is an effective method to study FR, as well as CME. We have followed different small scale and large scale dynamics before, during and after a prominence eruption. We have concentrated our study mainly on magnetic twist build up and transfer of the twist to the CME. This study is presented in the Chapter 6.

In Chapter 7 we have summarized the main observations and conclusions drawn from our study. We have also highlighted possible future works as a continuation of present study.

Chapter 2

Instruments and Data Reduction

Observatories are integral part of any astronomical study. Ground based observatories are playing important role in astronomical observations since ancient times. In recent years with the advent of satellite technology, space based observatories have marked their presence in the regime of astronomical observations. Observational astronomy from the Earth's surface is limited by the filtering and distortion of electromagnetic (em) radiation due to the Earth's atmosphere. It is also restricted to optical and radio wavelengths. Space based observatories have specific advantages over Earth based ones in these. A telescope, which is orbiting the Earth, are not affected by twinkling and light pollution from artificial light sources on the Earth. In this thesis I have primarily used space based instruments.

Data collected from four different instruments are used for the studies presented in this thesis. A brief description along with specifications of these four instruments are given in this chapter.

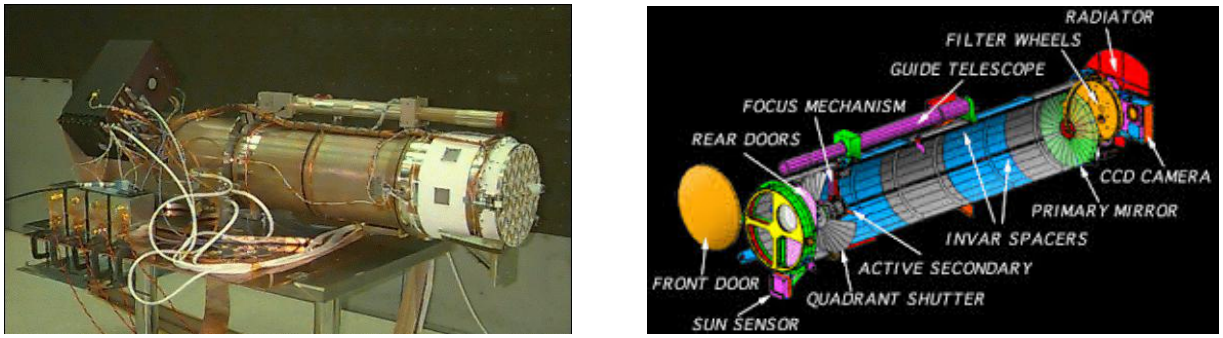

FIGURE 2.1: (*left panel*) Photo of the TRACE instrument during the test phase, (*right panel*) a schematic diagram of TRACE instrument. (image credit: LMSAL)

2.1 The Transition Region And Coronal Explorer (TRACE)

The Transition Region And Coronal Explorer (TRACE) is a NASA Small Explorer (SMEX) mission to image the solar atmosphere from the photosphere to the corona at high spatial and temporal resolution (Handy *et al.* 1999). The TRACE spacecraft was launched on April 2, 1998 (UT) into a Sun-synchronous (98°) orbit of 600×650 km. The spacecraft is in a polar orbit which allows continuous uninterrupted observations for approximately 9 months (mid February to mid November) each year, the remaining 3 months is the eclipse season where the view from part of the orbit is occulted by the Earth's atmosphere. TRACE is operated in coordination with Solar and Heliospheric Observatory (SoHO) from an Experimental Operational Facility (EOF) at Goddard Space Flight Centre (GSFC). The instrument collects images of solar plasmas from 10^4 to 10^7 K, with one arc second resolution and excellent temporal resolution and continuity.

The TRACE instrument consists of a 30 cm diameter Cassegrain telescope and a filter system feeding a CCD detector. Fig 2.1. shows the image of the TRACE telescope along with a schematic diagram indicating the different parts of the telescope. The TRACE telescope uses four normal-incidence coatings for the EUV and UV on quadrants of the primary and secondary mirrors. The segmented coatings on solid mirrors form identically sized and perfectly coaligned images. Pointing is internally stabilised to 0.1 arc second against spacecraft jitter. A Lumogen-coated

TABLE 2.1: The List of EUV and UV channels used in TRACE.

Channel(Å)	Width (Å)	Primary ion(s)	T (10^3k)
5000	Broad	Continuu	4-6.4
1700	200	Continuum	4-10
1600	275	C I, Fe II, cnt	4-10
1550	20	C IV	60-250
1216	84	H I Ly-α	10-30
173	6.4	Fe IX	160-2000
195	6.5	Fe XII	500-2000
284	10.7	Fe XV	1250-4000

1024×1024 CCD detector collects images over an 8.5×8.5 arc minute field-of-view (FOV). A powerful data handling computer enables very flexible use of the CCD array including adaptive target selection, data compression, and fast operation for a limited FOV. It observes in several UV and EUV channels, For all the channels, the primary ion(s) responsible for the emissivity in each channel, and their characteristic temperatures are listed in Table 2.1.

The TRACE instrument data are recorded as FITS files containing in-line JPEG compressed images, as downlinked from the spacecraft. Data is decompressed using the analysis routine *read_trace*. *trace_prep.pro* routine is used for data reduction. Detailed instructions for data reduction is available at http://www.lmsal.com/TRACE website.

2.2 Coronal Diagnostic Spectrometer (CDS)

The Solar & Heliospheric Observatory (SOHO), is a project of international collaboration between ESA and NASA to study the Sun from its deep core to the outer corona and the solar wind. SOHO was launched on December 2, 1995. The satellite is situated in a halo orbit around the L1 Lagrangian point 1.5 million kilometers from the Earth to provide an uninterrupted view of the sun. The twelve instruments on board SOHO were provided by European and American scientists.

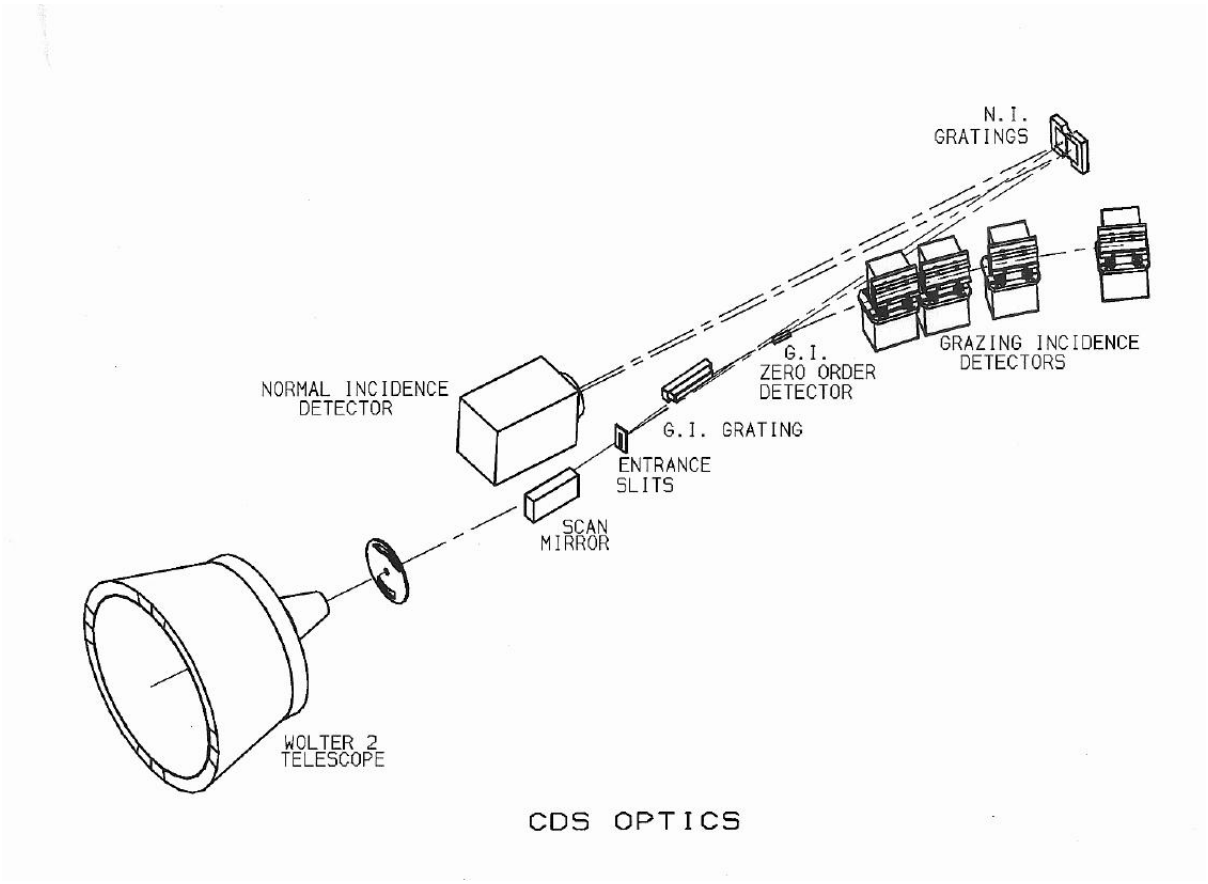

FIGURE 2.2: The CDS Optical layout shows both the Normal Incidence and Grazing Incidence spectrometers. (image credit: http://solar.bnsc.rl.ac.uk)

The Coronal Diagnostic Spectrometer (CDS) Harrison *et al.* (1995) is designed to measure plasma characteristics with spatial, temporal and spectral resolutions and ranges appropriate to study the structure and evolution of the solar atmosphere. It determines this information through the study of emission line characteristics in the extreme ultra-violet (EUV). The performance requirements of the CDS included the need to observe emission lines between 150 Åand 800 Å, so as to cover ions formed between 10^4 and a few $\times 10^6$ K. This, and the other scientific requirements of CDS, cannot be achieved by a single instrument. Consequently, the CDS is a double spectrometer having the wide wavelength range of a grazing incidence device plus the stigmatic imaging performance of a normal incidence instrument. The CDS uses a grazing incidence Wolter-Schwartzchild type 2 telescope to simultaneously feed a normal incidence spectrometer (NIS) and a grazing incidence spectrometer (GIS) through a common slit. Fig.2.2 shows the optical elements of CDS. Its spatial resolution is better than 3″(3000 km spatial extent), the spectral

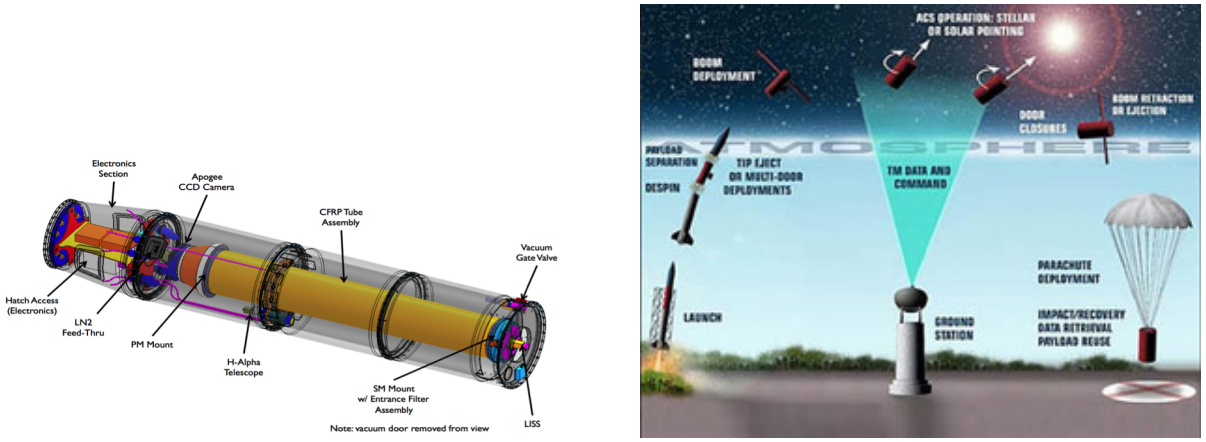

FIGURE 2.3: (*Left panel*) A schematic image of Hi-C telescope and (*right panel*) a cartoon showing the rocket experiment of launching the Hi-C telescope. (image credit: http://hic.msfc.nasa.gov/)

resolving power varies between $\delta\lambda/\lambda = 2000$ and $\delta\lambda/\lambda = 10000$, and the temporal resolution is a few seconds. The wavelength ranges observed are 307.60Å-379.40Å(NIS1), 513.03Å - 632.69Å(NIS2), 151.43Å - 221.07Å(GIS1), 256.45Å - 341.03Å(GIS2), 392.62Å - 491.99Å(GIS3), 658.99Å - 784.71Å(GIS4). To prepare the CDS data for analysation standard CDS software are used. Refer to CDS Software Notes (http://solar.bnsc.rl.ac.uk/swnotes) for more information.

2.3 Hi-C

The High Resolution Coronal Imager (Hi-C) instrument launched July 11, 2012 aboard a Black Brant sounding rocket (Fig. 2.3), from White Sands Missile Range. The instrument, a Ritchey–Chretien telescope (Fig. 2.3), has a single narrowband EUV channel centered on 193 Å. The images are recorded on a 4096×4096 back-illuminated CCD. The imaging system has a resolution of $0.103''$/pixel (14 times higher resolution than the Solar Dynamics Observatory) with 5.5s cadence; hence the images collected during this first launch are the highest resolution images of the million-degree solar corona to date. During its 10 minute fight, it reached an altitude of 283 km. The Hi-C images are co-aligned to correct for jitter of the rocket and pointing drift. Also dust affected pixels are corrected by interpolating from

nearest neighbor. Additional information regarding data processing can be found in Kobayashi *et al.* (2014). Data can be acquired from https://hic.msfc.nasa.gov/.

2.4 AIA/SDO

The Solar Dynamics Observatory (SDO) (Pesnell *et al.* 2012) is the first mission to be launched for NASA's Living With a Star (LWS) Program. The main objective of SDO is to enhance our understanding on the Sun's influence on Earth and Near-Earth space by studying the solar atmosphere in higher spatial and temporal resolution, in different wavelengths simultaneously. SDO was launched on February 11, 2010, 10:23 am EST on an Atlas V from SLC 41 from Cape Canaveral. The satellite is in an inclined geosynchronous orbit that allows the contact with a single, dedicated ground station for a continuous downlink the large amount of data, which result due to high cadence and spatial resolution. The orbit is inclined at 28.5°, with nearly continuous view of the Sun, apart from two eclipse seasons (due to shadow of Earth) per year during which there will be daily interruptions in the observations. The Atmospheric Imaging Assembly (AIA) is one of the three instruments on board SDO (Lemen *et al.* 2012). AIA consists of four telescopes, provides full disk images, on 10 EUV channels almost simultaneoooously. The spatial resolution of AIA images is 1.5″and time cadence is 12 seconds. Fig. 2.4 shows the four telescopes mounted on theable sdo satellite. The different observational channels are listed in Table 2.2.

To prepare the AIA data for analysation standard AIA software are used. There are 0 level data AIA data at Level 1.0 have already been processed to remove bad pixels and spikes. However, such data at Level 1.0 are not coaligned and have slightly different plate scales and roll angles, making analysis of data from multiple AIA channels problematic. To remedy these issues, the data need to be converted to Level 1.5, which can be done using the *aia_prep.pro* routine available through SSW.

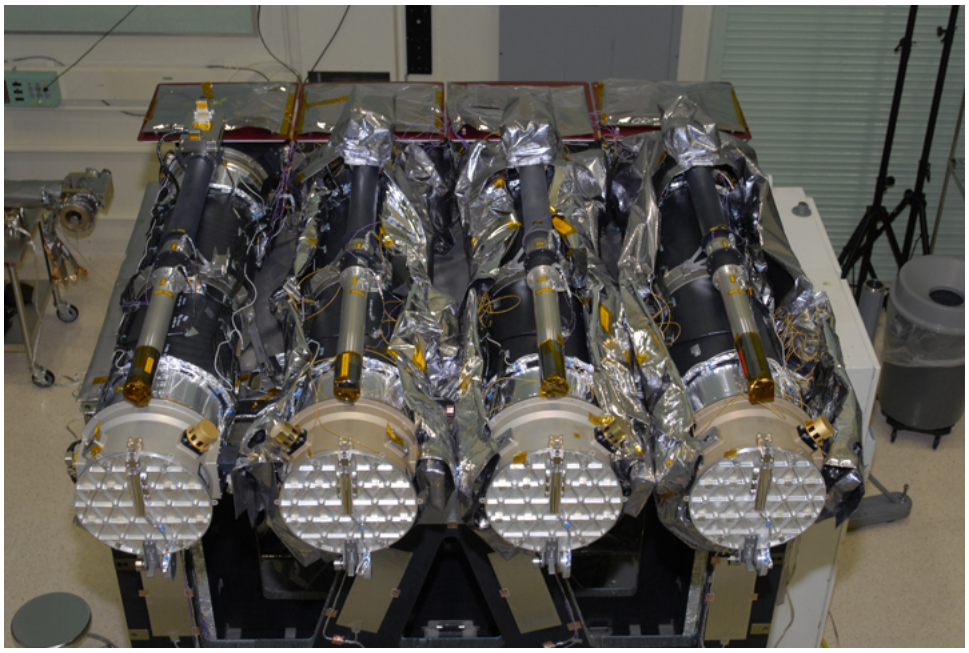

FIGURE 2.4: The four AIA telescopes mounted on the SDO spacecraft during integration at NASA's Goddard Space Flight Centre. *Image credit:* Lemen *et al.* (2012)

TABLE 2.2: The list of seven EUV and three UV-visible channels used in AIA. The primary ion(s), the region of atmosphere that can observed and their characteristic temperatures are given. Adapted from Lemen *et al.* (2012)

Channel	Primary ion(s)	Region of atmosphere	Char. log(T)
4500 Å	continuum	photosphere	3.7
1700 Å	continuum	temperature minimum, photosphere	3.7
304 Å	He II	chromosphere, transition region	4.7
1600 Å	C IV+cont.	transition region , upper photosphere	5.0
171 Å	Fe IX	quiet corona, upper transition region	5.8
193 Å	Fe XII, XXIV	corona and hot flare plasma	6.2, 7.3
211 Å	Fe XIV	active-region corona	6.3
335 Å	Fe XVI	active-region corona	6.4
94 Å	Fe XVIII	flaring corona	6.8
131 Å	Fe VIII, XXI	transition region, flaring corona	5.6, 7.0

Chapter 3

Propagating Disturbances along Coronal Loops from EUV imaging and Spectroscopic Observations

The Imaging and spectroscopic observations compliment each other in study of waves and oscillations in coronal structures. JOP 165 observation programme was designed to synchronise simultaneous observations by imaging, spectroscopy and magnetogram. An active region (AR 10457) was followed as it moved from one limb to the other. To study the correlation of magneto-acoustic waves in different regions of solar atmosphere, we have chosen four spectral lines from CDS, namely He I , O V , Mg X and Si XII . The presence of propagating disturbances are identified at the foot points, also away from foot points for off-limb and on-disk loops from simultaneous observations using TRACE and CDS. The propagation velocities found from TRACE observations, indicate these disturbances are slow magneto-acoustic in nature. The phase relation between intensity and Doppler velocity oscillations also support that. The in-phase intensity oscillations for all the four spectral line show that these disturbances are propagating from the lower layer of the solar atmosphere to the corona[1].

[1]Part of this study is published in Datta *et al.* (2015)

3.1 Introduction

Propagating Disturbances (PDs) are well observed phenomena along different coronal structures. The first observational report on PDs along coronal loops was by Berghmans and Clette (1999). Since then a number of authors have studied PDs in active region loops (for *e.g.,* see the review by de Moortel 2009; Krishna Prasad *et al.* 2012b; Su *et al.* 2013). Such studies have gained importance in the recent times for their probable role in coronal heating (De Moortel 2008) and for their application as a diagnostic tool through coronal seismology (Uchida 1970; Roberts *et al.* 1984; De Moortel and Nakariakov 2012). PDs are reported from the analysis of spectroscopic data also (*e.g.,* Banerjee *et al.* 2000, 2001, 2009; Wang *et al.* 2009a,b) through the detection of oscillations in intensity and Doppler velocity. They are mostly interpreted as propagating slow magneto-acoustic waves based on the observed properties.

Imaging and spectroscopic observations are unique in their own way, but a combined study gives a better understanding of the observed PDs. O'Shea *et al.* (2002) reported both upward and downward propagating disturbances in upper corona from a combined analysis of data from TRACE and CDS/SOHO. Del Zanna (2003) has shown a clear relation between emission in the corona, transition region and the photosphere using observations from TRACE and CDS/SOHO. Marsh *et al.* (2003, 2004) detected slow magneto-acoustic waves of periodicity 5 *min* along coronal loops using the same set of instruments. Recently, De Pontieu and McIntosh (2010) have studied PDs using data from TRACE and *Hinode*/EIS and suggested that the interpretation of PDs as waves is not unique. They further indicate that a quasi periodic upflow can give similar observational evidences in intensity and can be misinterpreted when studied from the imaging data alone. These authors also found that the usual intensity and velocity oscillations expected for the slow waves, are in fact accompanied by in-phase oscillations in line width and the spectral line profiles periodically show a significant blue-shifted component, a signature of quasi-periodic upflow. Tian *et al.* (2011) have also observed these in-phase oscillations in spectral line intensity, Doppler velocity, and line width suggesting that the observed oscillatory behavior is due to quasi periodic up-flows. However, the

flow interpretation is not supported by all. Verwichte *et al.* (2010) have demonstrated that slow waves can cause line asymmetries when averaged over a time period. Wang *et al.* (2012) observed blue-wing asymmetry in hot coronal lines and suggested that the propagating intensity and Doppler velocity oscillations are due to variations of the core component, not due to the high velocity minor component. This argument supports the slow wave interpretation. Krishna Prasad *et al.* (2012a) have studied PDs using combined observations from *Hinode*/EIS and AIA/SDO. They have observed oscillations in spectral line intensity and Doppler velocity but not in line width. They also did not find any visible asymmetry in the line profile.

Nishizuka and Hara (2011) have reported, using data from *Hinode*/EIS, both continuous outflows and waves by analyzing the line profiles at the base and higher locations of the outflow. Ofman *et al.* (2012) and Wang *et al.* (2013) have done three dimensional modeling of a bipolar Active Region (AR) and observed that excitation of damped slow magneto-sonic waves that propagate along the loops is possible due to onset of flows with subsonic speeds. In the present scenario of several views about propagating disturbances combined analyses, involving imaging and spectroscopic observations, have become more relevant. Different modes of observations highlight different aspects that can give a better understanding of the nature of the PDs.

We have detected and studied the nature of PDs along active region coronal loops when those were at the off limb and on disk positions, combining EUV images from TRACE and spectroscopic data from CDS. PDs have been detected near the foot points of the loop from the TRACE images. The spectral parameters, peak intensity, Doppler velocity, and line width, at the foot points or at another position along the loop, have been analyzed to conclude further about their nature.

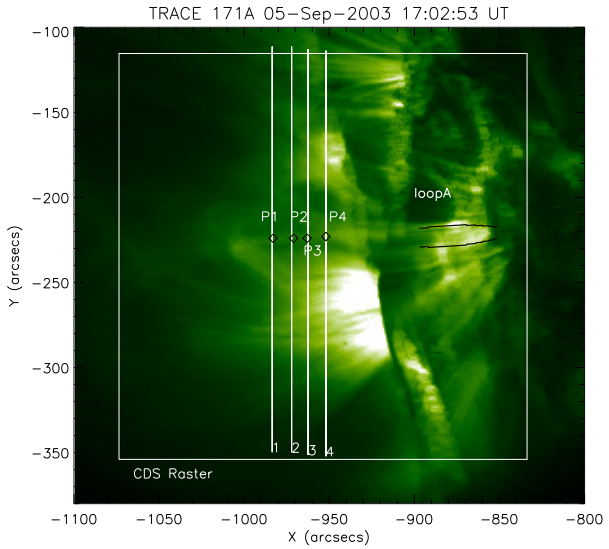

FIGURE 3.1: TRACE image showing AR 10457 at an off limb position on 5th September, 2003. A section of the loop under investigation is marked as Loop A with black lines. The white box indicates the field of view of CDS raster scan and the vertical lines mark the sit and stare slit positions. Black diamonds indicate the pixel positions on different slits where Loop A intersects.

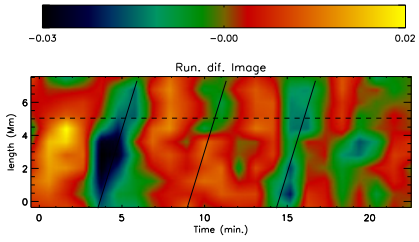

FIGURE 3.2: Enhanced space-time map created from the section of Loop A marked by black lines in Fig.3.1. The scale of the color bar indicates the percentage oscillation. The dashed line marks the location where wavelet analysis is done to determine the periodicity. Slope of the slanted solid lines drawn along the dark ridges gives an estimate on the propagation speed.

3.2 Propagating Disturbances along A Coronal Loop at an off limb position

3.2.1 Data

The data used in this analysis are part of a Joint Observational Programme (JOP 165). In this campaign an active region (AR 10457) was followed over a period of 12 days (5th September, 2003 to 17th September, 2003) during its journey from one limb to the other and involves observations from *Transition Region and Coronal Explorer* (TRACE), *Coronal Diagnostic Spectrometer* (CDS) and *Michelson Doppler Imager* (MDI) on board SOHO. TRACE collects images of solar plasma at different temperatures ranging from 10^4 to 10^7 K, using several UV/EUV/visible channels. CDS performs EUV spectroscopy for plasma temperatures ranging from 2×10^4 to 3×10^6 K. The data obtained on 5th September, 2003, when the active region was at an off limb position is used in the current work. The TRACE data consist an image sequence of 28 frames of 512 pixel square, recorded in Fe IX/Fe X 171Å channel, during 17:02 UT to 17:32 UT. The field of view is centered at (-980″,-132″). This data have been reduced using the routine *trace_prep.pro* of **sswidl** following the standard procedure. The final pixel size and cadence of the data are 1.0″and 60 s respectively. The CDS data consist of a raster scan and five sit and stare observations. The raster scan was taken during 15:10 UT to 15:32 UT using Mg IX (368.07 Å) line. This 60×72 pixels scan has its lower left corner at (-1081″, -363″). The sit and stare observations are taken during 16:02 UT to 18:02 UT, with half an hour observing time at each of the slit positions. All the slit positions are separated by 10″with the one closest to the limb being located at solar-X ≈ -949″. Four out of the five sit and stare observations taken in the coronal Si XII 520.6 Å(log T_e = 6.3) line, are used in this analysis. The observations were made in 5 other lines which were not useful either because they were transition region lines with a poor signal off limb or because the oscillations in those lines were inconsistent. Standard CDS software are used for the initial preparation of the data. Since the data were observed in the post recovery phase

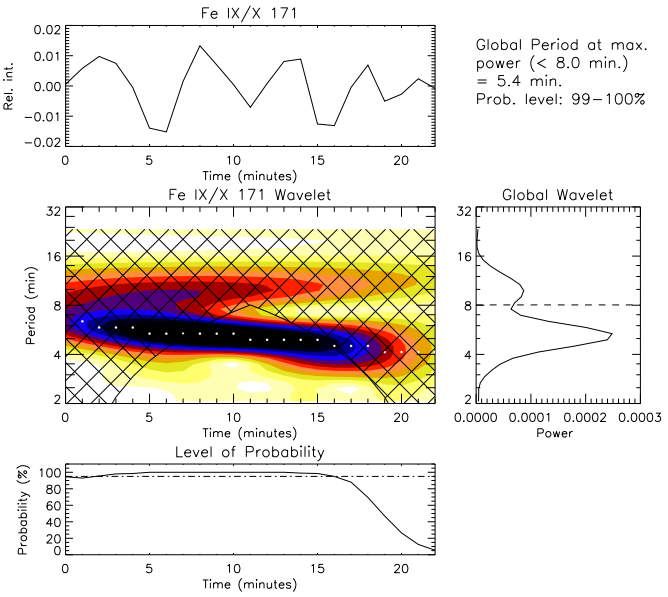

FIGURE 3.3: Wavelet plot for intensity variations observed from TRACE at an arbitrarily chosen pixel location along LoopA (Fig.3.1). Each panel consists the detrended light curve (top left), wavelet spectrum (middle left), level of probability (lower left) and power spectrum (right).

of SOHO, the spectral profiles were fitted with a broadened Gaussian[2]. The final pixel resolution and the cadence of the data are 4.0″× 3.3″and 21 s, respectively. Proper alignments between different data sets play a major role when observations from multiple instruments are used in the analysis. The CDS raster in Mg IX line and the corresponding sub field from the TRACE image, are co-aligned using intensity cross correlation and the slit positions are corrected by the appropriate offset. The final CDS slit positions and the field of view of the raster scan are shown on a sub field of the TRACE image in Fig. 3.1.

[2]After the recovery of SOHO, the line profiles of CDS were found to have acquired substantial wings. A function was then developed to accommodate these enhanced wings over a Gaussian and named broadened Gaussian. Refer to CDS Software Notes #53 (http://solar.bnsc.rl.ac.uk/swnotes/cds_swnote_53.pdf) for more information.

TABLE 3.1: Periodicities and amplitudes of oscillations along Loop A as obtained from wavelet analysis. Results from TRACE 171 images and from 4 CDS sit and stare observations are listed.

Emission line/ Channel	Approximate distance from the footpoint (Mm)	Intensity		Velocity		Line width	
		amplitude (%)	period (min)	amplitude (km s^{-1})	period (min)	amplitude (%)	period (min)
Fe IX/Fe X 171Å	5	0.5	5.4	-	—	-	—
Si XII 520.6 Å	64	1.4	4.1	1.5	3.5	0.5	5.3
Si XII 520.6 Å	71	1.6	5.8	1.6	5.8	0.5	5.3
Si XII 520.6 Å	78	2.4	4.9	1.6	9.0/4.1	0.8	7.5/3.5
Si XII 520.6 Å	86	-	—	1.5	6.3	-	—

3.2.2 Analysis and Results

In this section we discuss the techniques used to detect the PD, to determine the periodicities of oscillations and other properties, from both TRACE and CDS/-SOHO data.

We have chosen an active region loop, marked as Loop A in Fig. 3.1, for this study. The loop foot point is located at solar-X ≈ -860″. A section of the loop close to its foot point is analyzed to find PDs from the TRACE data. A space-time map is created following a method similar to that explained in Krishna Prasad *et al.* (2012a) and De Moortel *et al.* (2000). From each time frame, we create a 1-d array of intensity along the loop, by averaging and normalizing over pixels along the cross section of the loop which are then stacked together to generate the desired map. This map was then processed by detrending and normalizing, to enhance the visibility of the bands. An 8 point running average has been used for detrending, which should filter out oscillations with periodicities more than 8 min. The final processed space-time map is shown in Fig. 3.2. Alternate bright and dark fringes visible in this map with positive slope indicate the presence of PDs propagating outward. To determine the periodicity, we have done wavelet analysis (Torrence and Compo 1998) at an arbitrarily chosen pixel (shown by the dotted line on this map) approximately at a distance of 5 Mm from the loop foot-point. The results of this analysis are shown in Fig. 3.3. A running average of 15 points (≈ 15 min) has been subtracted from the original TRACE light curve to eliminate the background trend. This detrended light curve is then subjected to the wavelet analysis which

is shown in the upper panel of the wavelet plot. The Morlet function, a complex sine wave modulated by a Gaussian, is chosen as the Mother wavelet function. The middle left panel shows the actual wavelet plot which displays the presence of oscillations at different periodicities and their evolution with time. The cone of influence (Torrence and Compo 1998) is marked by the cross hatched region. The periodicities, obtained in this region, are not reliable due to edge effects. The power at different periods averaged over time is shown in the global wavelet plot, in the right panel. A probability estimate was calculated using the randomization method with 200 permutations as outlined in detail by Banerjee *et al.* (2001). The variation of the probability estimate associated with the maximum power at each time in the wavelet-power spectrum is shown in the lower left plot. The dash-dot line in this plot marks the 95% probability level. The periodicity of the PD is found to be 5.4 min. To calculate the propagation speed, a straight line is drawn parallel to the ridges and its slope is estimated. Three parallel slanted lines were drawn on the space-time map in Fig. 3.2, to indicate this. The positioning of these lines along the adjacent dark bands confirms the periodicity , which is obtained from wavelet analysis. The estimated propagation speed is about 39 km s^{-1}.

Spectral data from CDS sit and stare observations are also analyzed to understand the nature of the detected PDs along Loop A. The sit and stare slits of CDS are crossing Loop A perpendicularly. The pixel locations of the crossing points of the loop and CDS slits are identified and marked as P4 (on Slit 4, Solar-X= $-949''$), P3 (on Slit 3, Solar-X= $-959''$), P2 (on Slit 2, Solar-X= $-969''$) and P1 (on Slit 1, Solar-X= $-980''$) in Fig. 3.1. Wavelet analysis is done at these locations to detect oscillatory behavior in spectral line intensity, Doppler velocity and line width. The analysis procedure followed is similar to the one described above. CDS time series are smoothed over 2 temporal points (which removes variation less than 42 s) and a running average of 25 points ($\approx$9 min) has been subtracted to eliminate the background trend before applying the wavelet technique. The results corresponding to the intensity, Doppler velocity, and line width, at location P4 are shown in Fig. 3.4. The primary periods of oscillation were found to be 4.1 min and 3.5 min for intensity and Doppler velocity, respectively. The wavelet plots show the presence of a few other periodicities in both the cases. The line width at this location display a strong oscillation of 5.3 min. Location P3 demands a special attention, as the observation time (17:02 UT to 17:32 UT) matches with

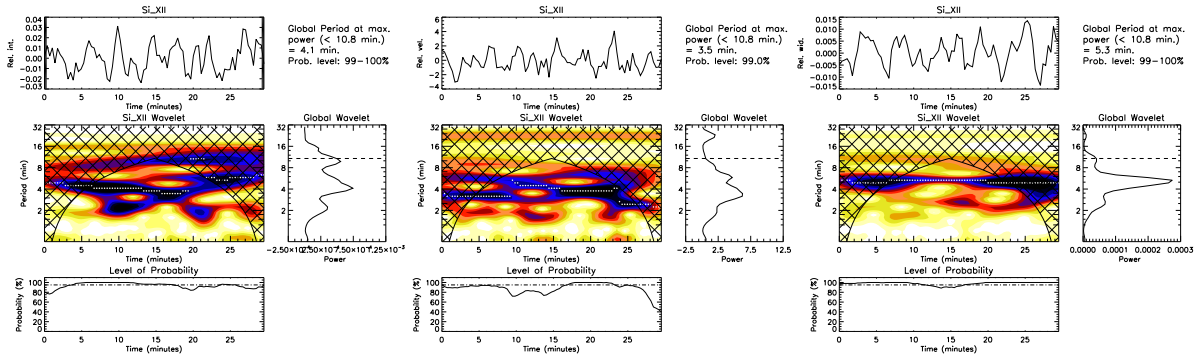

FIGURE 3.4: Wavelet analysis of variations in intensity (*left panel*), Doppler velocity (*middle panel*) and line width (*right panel*) from CDS Slit4. Panel descriptions are same as explained in Fig.3.3.

that of the TRACE image sequences. Here, we found oscillations of period 5.8 min for both line intensity and Doppler velocity. The line width variation also show a periodicity of 5.3 min close to this value. Corresponding wavelet plots are shown in Fig. 3.5. These values are also close to that found from the TRACE image analysis. By combining TRACE and CDS in our study, we are able to determine the periodicities of PDs simultaneously at the foot point and at a distance of approximately 71 Mm away from the foot point. At location P2 ($\approx$ 78 Mm away from the loop foot-point), the intensity and Doppler velocity variations show periodicities of 4.9 min and 9.0 min respectively, as shown in Fig. 3.6. The Doppler velocity oscillation also show a second peak at 4.1 min. The oscillations in line width show the presence of two periods 7.5 min and 3.5 min with a broadened peak at the latter period. The broadened peak indicates the distribution of power over a range of periodicities, while the sharp peak in the global wavelet plot at P4 supports the presence of a dominant period in the line width oscillation. As we move towards the loop apex, at location P1, a 6.3 min oscillation is observed in Doppler velocity while line intensity and line width do not show any clear sign of oscillation. The periodicities and amplitudes of the oscillations found at these locations along the loop are summarized in Table 3.1 for all the line parameters.

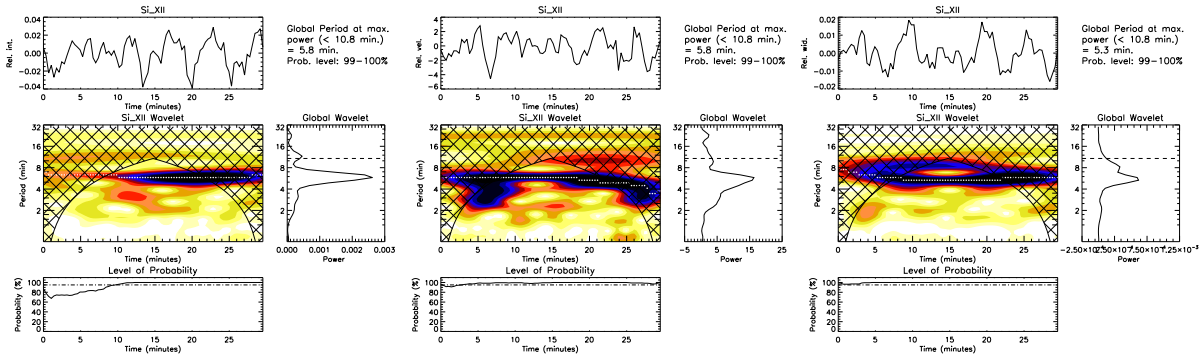

FIGURE 3.5: Wavelet analysis of variations in intensity (*left panel*), Doppler velocity (*middle panel*) and line width (*right panel*) from CDS Slit3. Panel descriptions are same as explained in Fig.3.3.

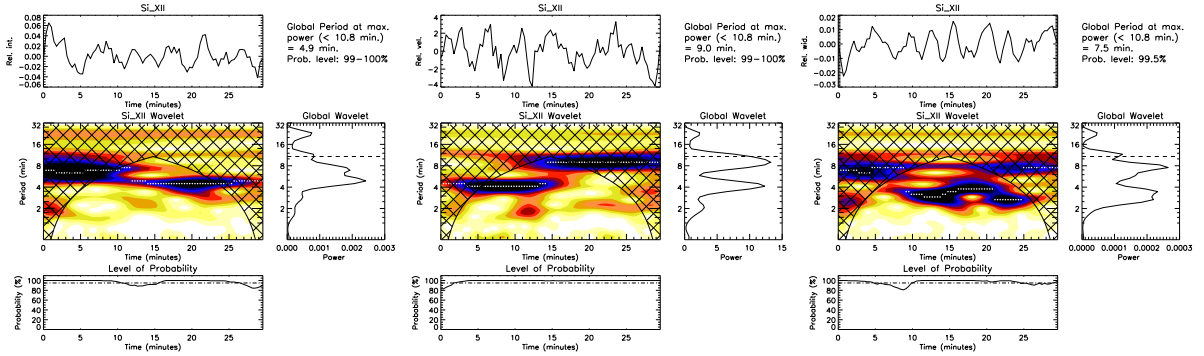

FIGURE 3.6: Wavelet analysis of variations in intensity (*left panel*), Doppler velocity (*middle panel*) and line width (*right panel*) from CDS Slit2 .

3.3 Propagating Disturbances along Coronal Loops at on disk position

The active region was at an on disk position on 8th September, 2003. We have analyzed two image sequences from TRACE, along with co-temporal and co-spatial CDS spectroscopic data.

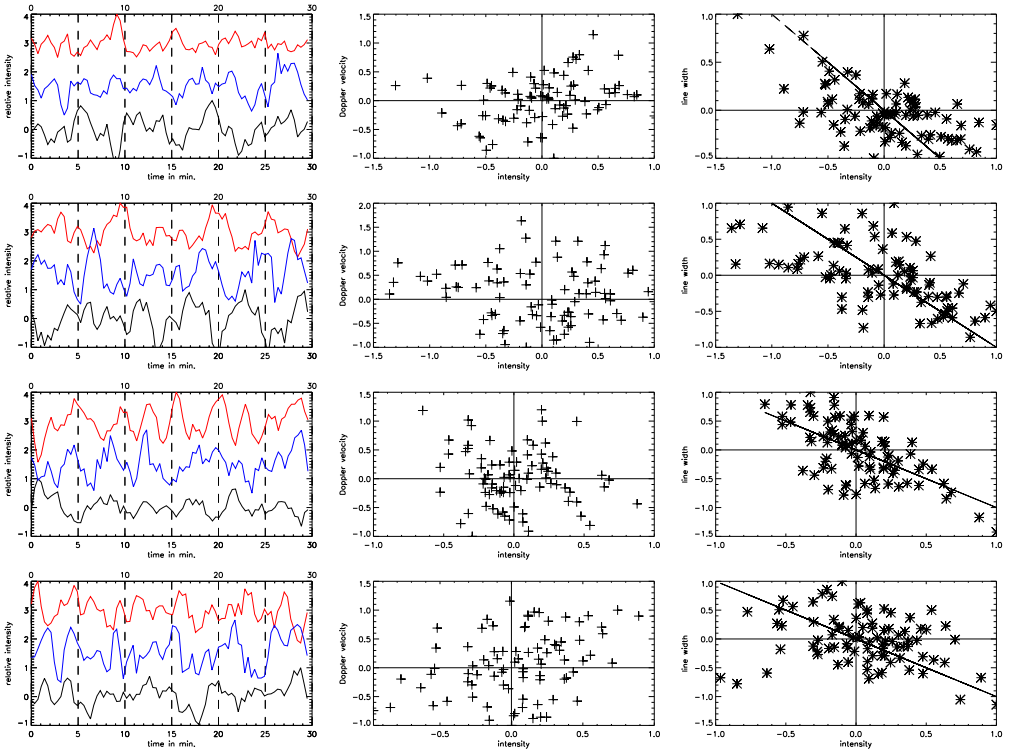

FIGURE 3.7: Left panels show the oscillations in intensity (black), Doppler velocity (blue) and line width (red) at different positions along the loop. All the curves are background subtracted and normalized by corresponding maximum value. The curves for Doppler velocity and line width are shifted along Y-axis for clarity. Positive values of Doppler velocity indicate blue shift. The middle panels show the relationships between normalized intensity and Doppler velocity. The right panels show the relationships between normalized intensity and line width. The black line indicates 180° phase difference. The rows from top to bottom display the results for locations P4, P3, P2, and P1 respectively.

3.3.1 PD along a coronal loop

3.3.1.1 Data

The data consist TRACE image sequence of 40 frames of 600 pixel square, recorded in Fe IX/Fe X 171Å channel, during 11;28 UT to 12:08 UT. The field of view is centered at (-550″,-290″). The final pixel size and cadence of the data are 0.5″and 60 s respectively. The CDS data consist of a raster scan and one sit and stare observation. The raster scan was taken during 07:44 UT to 08:06 UT using Mg IX (368.07 Å) line. This 60×72 pixels scan has its lower left corner at (-605″,

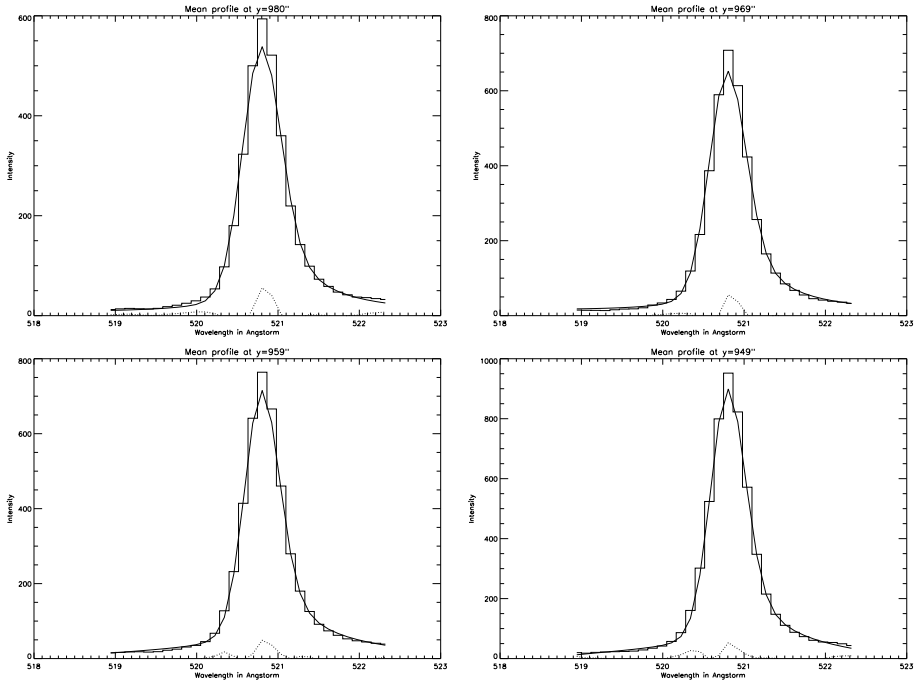

FIGURE 3.8: Time averaged spectral profiles of Si XII 520.6 Å line at the four analysis locations P1 (*upper left*), P2 (*upper right*), P3 (*lower left*) and P4 (*lower right*). The solid line displays the best fit to the data using a broadened Gaussian function. The dotted line indicates the residual.

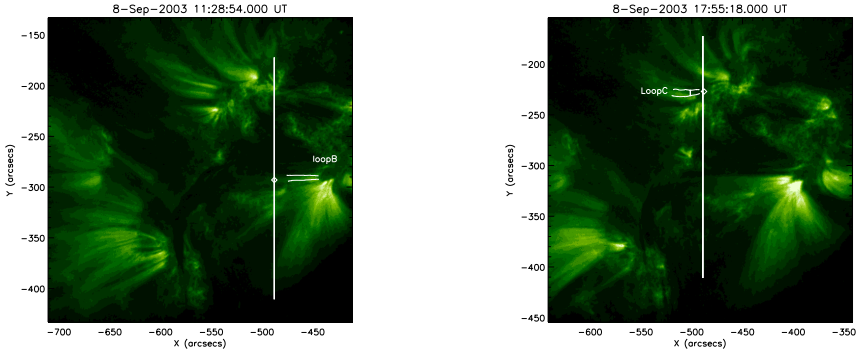

FIGURE 3.9: (*Left panel*)TRACE image showing AR 10457 at on disk position on 8th September, 2003. Loop B is marked with white lines. The vertical line mark the sit and stare slit position. White diamond indicate the pixel position where Loop B and CDS slit intersect. (*Right panel)* Position of Loop C and CDS slit on TRACE image.

TABLE 3.2: Periodicities and amplitudes of oscillations along Loop B and Loop C as obtained from wavelet analysis. Results from TRACE 171 images and from CDS sit and stare observations are listed.

Along	Emission line/ Channel	Intensity		Velocity	
		amplitude (%)	period (min)	amplitude (km s^{-1})	period (min)
Loop B	Fe IX/Fe X 171Å	4.0	4.1	-	—
	Si XII 520.6 Å	2.0	4.1	4.0	4.9
	Mg X 624.9 Å	3.0	4.5	3.0	5.8
Loop C	Fe IX/Fe X 171Å	4.0	5.4	—	—-
	Si XII 520.6 Å	2.5	6.3	2.0	5.8
	Mg X 624.9 Å	4.0	5.3	4.0	3.8
	O V 629.5 Å	5.0	6.3	4.0	6.5
	He I 584.3 Å	3.0	6.3	2.0	5.3

-413″). The sit and stare observation is taken during 11:36 UT to 12:05 UT, and is located at solar-X ≈ -489″. The coronal Mg X 624.9 Å(log T_e = 6.0) and Si XII 520.6 Å(log T_e = 6.3) lines, are used in this analysis. Data are reduced and aligned following the same procedure as in Section 3.2.1. The final pixel resolution and the cadence of the data are 4.0″× 3.3″and 21 s, respectively. For the

3.3.1.2 Analysis and results

The active region consist several fan loops. One of the loops, Loop B, marked in Figure 3.9, is chosen for the study, as CDS sit and stare slit is intersecting it at a position away from the foot point. PD is detected along this loop from TRACE images. We have followed similar method as in Section 3.2.2. The periodicity of TRACE line intensity is found to be 4.1 min and the estimated propagation speed is 32 km s^{-1}. The CDS slit is intersecting the loop B at the location (-489″,-291″). The Si XII and Mg X lines of CDS show oscillation of periodicities 4.1 min. and 4.5 min. respectively. The periodicities of Doppler velocity for these lines are 4.9 min. and 5.8 min. respectively. Mg X show oscillation in line width also. The periodicities and oscillation amplitudes are tabulated in Table 3.2. Due to the perpendicular alignment of the CDS slit, it can not be concluded that the signals from the transition region belong to the loop under consideration. So, we have restricted our analysis in coronal lines.

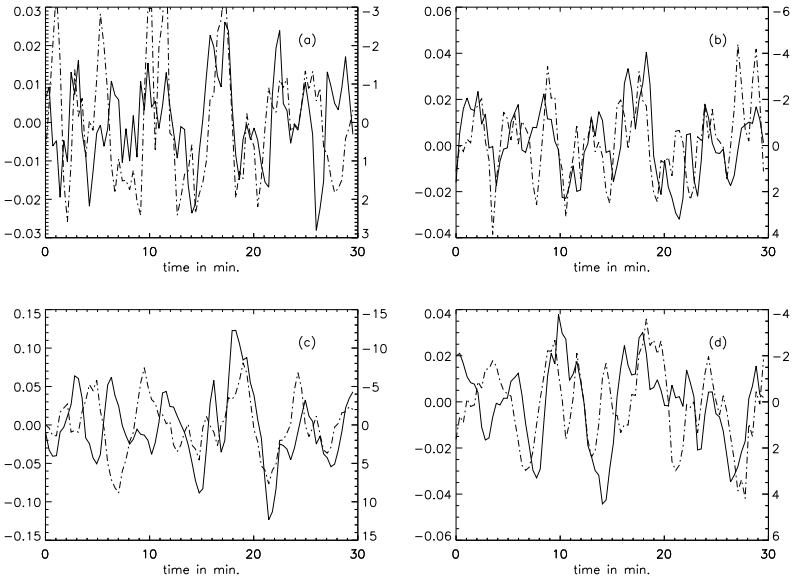

FIGURE 3.10: Variations in line intensity at the foot point of Loop C, in CDS (a) Mg X, (b) Si XII, (c) O V, and (d) He I lines. Corresponding variations in Doppler velocity is overplotted in dashed line. left hand y axis of each panel shows relative intensity and right hand y axis shows the Doppler velocity.

3.3.2 PD near the foot point of a coronal loop

3.3.2.1 Data

For this study TRACE image sequence of 40 frames of 600 pixel square, centered at (-489″,-300″), recorded during 17:55 UT to 18:25 UT is used. CDS data consist of raster scan, taken during 22:33 UT to 22:56 UT, using Mg IX and sit and stare observation, taken during 18:04 UT to 18:34 UT. Two transition region lines, He I 584.3 Å(log T_e = 4.1) and O V 629.5 Å(log T_e = 5.4), and coronal Mg X 624.9 Åand Si XII 520.6 Ålines, are used in this analysis. The positions of CDS raster scan, and sit and stare observation are the same as those of the first sets.

3.3.2.2 Analysis and results

The foot point of Loop C (right panel of Figure 3.9) is at (-489″,-226″). The CDS sit and stare slit intersects this loop at the foot point. We find PD of periodicity 5.4 min. along this loop. PD is propagating outward with an estimated speed of 16 km s^{-1}. The primary period of oscillation in line intensity of Mg X line is found to be 5.3 min., while periodicities of line intensity variations of other three lines are 6.3 min. All the line show Doppler velocity variations of similar periodicities (Table 3.2). We do not find significant oscillation in line width variation for any of the four CDs lines. We also find that oscillations in the line intensity are in phase with the oscillations of Doppler velocity, for the four CDS lines under consideration.

3.4 Discussion

We studied the properties of PDs along an active region loop using data obtained through simultaneous imaging and spectroscopy. The periodicity and propagation speed of the PDs, as obtained from the imaging data, were found to be 5.4 min and 39 km s^{-1}, respectively. Although the imaging data do not show the PDs extending far along the loop the spectroscopic data at four different locations away from the foot point, show oscillations in all the three line parameters roughly at a similar period. It is possible that the broadband filters and a different sensitivity of the imaging instrument (TRACE) might have led to a non-detection of these low-amplitude oscillations at such distances (Krishna Prasad *et al.* 2012a). For instance, Wang *et al.* (2009b) observed PDs in the spectroscopic data obtained from *Hinode*/EIS but could not find them in the corresponding TRACE data, which they attribute to lower sensitivity of the instrument. So we believe the oscillations observed in the spectroscopic data (away from the foot point) and the PDs found from the imaging data (close to the foot point) are related particularly since the periodicities are similar. The ≈5 min periodicity and the subsonic propagation speeds might suggest the PDs are due to propagating slow magneto-acoustic waves but the spectroscopic data show clear oscillation in line

width as well. However, the oscillations in line width were prominent at location P4 which is relatively closer to the foot point and tend to show other periods as we move to P2 and no significant oscillation was detected at location P1. The Doppler velocity oscillations, on the other hand, show clearer peaks as we move towards P1. This might imply that wave-like behavior is more evident away from the foot point while the locations close to the foot point are affected by flows or some similar events. A cross-correlation analysis between intensity and Doppler velocity at these locations show no clear correlation except at P3 where a phase lag of $\approx 84^{\circ}$ was found (Figure 3.7). The lack of clear correlation (which is expected) might be due to the presence of multiple periods but the phase lag found at P3 is difficult to interpret. The time averaged spectral line profiles at locations P1 to P4 are shown in Fig. 3.8. The data are fitted with a broadened Gaussian function along with a polynomial background. The overplotted solid lines in the figure represent the best fits to the data and the dotted line represent the residual. These profiles do not show much asymmetry apart from the inherent red asymmetry expected for the post recovery NIS-2[3] spectra. It may be noted that averaging over time reduces the asymmetry caused by periodic upflows unlike the case of strong persistent uplfows. So, we inspected a few individual profiles and they seem to show similar behaviour. However, a clean spectral profile (with no blends and inherent asymmetries) with very good signal-to-noise is required to identify the low-amplitude blue wing enhancements due to quasi-periodic upflows. Simultaneous imaging and spectroscopic observations with better signal-to-noise are therefore crucial to improve our understanding on these PDs.

We find PDs near the foot point of Loop B from the imaging data. The estimated propagating speed is found to be lower than the acoustic speed. We also find oscillations in line intensity and Doppler velocity variations in coronal Mg X and Si XII line at a position away from the foot point of the same loop. The similar periodicities of all the oscillations, which are found near the foot point (from the imaging data), as well as at a distance along the loop (from the spectroscopic data), indicate that these oscillations are related. A propagating speed lower than the acoustic speed suggests that this PD along the Loop B might be an example of slow magneto-acoustic wave. For Loop C we observe PD near the foot point

[3]NIS stands for Normal Incidence Spectrometer of CDS. NIS-2 refers to the second detector that records the wavelength range 513-613 Å.

from imaging data, and simultaneous spectroscopic data. For this case, we observe oscillations in line intensity and Doppler velocity variations. But none of the four line shows any significant oscillation in line width of the spectral lines. The absence of oscillation in line width indicates that the observed PD is due to slow magneto acoustic mode. We may recall here that the propagating speed along Loop C is found to be much lower than those along Loop A and B. We can also conclude that this is an example of propagating slow mode, as oscillations of line intensity and Doppler velocity are in phase for all the spectral line under consideration (Figure 3.10). He I intensity oscillation has strong cross correlation with intensity oscillations in O V, Mg X and Si XII. The cross correlation factros are 0.76, 0.93 and 0.70 respectively. Combining all these, we conclude that this is an eample of propagating slow magneto acoustic wave from the transition region to the upper corona.

The origin and damping of these disturbances is another important aspect that might require simultaneous observations in different layers from photosphere to corona. The recent launch of IRIS (De Pontieu *et al.* 2014) seem to complete the current available instruments to provide such coverage.

Chapter 4

Wave Damping along Polar Plumes

Polar plumes are the open magnetic structures which expand radially outwards. Regions between the plumes, are known as 'interplumes'. Plumes are found to be brighter and cooler compared to the interplumes. Polar plume/interplume regions are important for their contribution towards acceleration of solar winds. These structures, both plumes and interplumes, are known to host the propagating intensity disturbances. The presence of these disturbances, in such structures, have been shown from imaging data (Deforest and Gurman 1998) as well as from spectroscopic observations (Ofman *et al.* 1997). These disturbances are mainly concluded as slow magneto acoustic waves as the propagating velocities of these waves are very close to the sound speed at those temperatures (Ofman *et al.* 1999; Banerjee *et al.* 2009; Krishna Prasad *et al.* 2011). In an another interpretation, these propagating disturbances are also identified as quasi periodic upflows (De Pontieu and McIntosh 2010; Tian *et al.* 2011). Such conclusions are based on primarily on the existence of strong 'red-blue' asymmetries in the line profiles. However, the absence of blue ward asymmetry in the line profile, higher up in loops (Krishna Prasad *et al.* 2012a; Gupta *et al.* 2012) and the subsonic propagation speed (Kiddie *et al.* 2012) again indicate the nature of these disturbances to be of slow magnetoacoustic waves.

These waves, when propagate through loops, decay very rapidly. The main damping mechanism of these waves, is the anisotropic thermal conduction (De Moortel and Hood 2004, 2003).Though it has been shown that there are contributions, though very small, from the other dissipative mechanisms, like the compressive viscosity, area divergence, mode coupling and gravitational stratification (de Moortel (2009) and references there in). Using the AIA imaging data, Gupta (2014) showed that these waves damp heavily within a distance of 10 Mm and the damping rate reduce significantly afterwards. Krishna Prasad *et al.* (2012b) found that the damping of these slow waves has a frequency dependence. Using imaging data, Krishna Prasad *et al.* (2014) showed that the frequency dependence of such damping, is different for different structures such as active region fan loops/plumes and polar plumes. A linear damping theory, with thermal conduction as the primary damping agent, predicts a slope of 2 in a log-log wave period vs damping length plot. Upon finding different values of this slopes ($\sim$1 for active region and $\sim$ - 0.3 for the polar cases), Krishna Prasad *et al.* (2014) concluded thermal conduction, alone may not be able to produce the observed nature of these frequency dependent damping. Mandal *et al.* (2016) used a 3-D simulations, followed by a forward modelling to show that such different nature of the slope, as found in the active region fan loops, can still be explained by a linear wave damping theory where thermal conduction is the main damping agent. Here, we must highlight that these authors still could not reproduce the negative slope as found in the polar plumes/interplumes observations.

Our main aim in this work is to do a statistical study of the polar plumes and interplumes and to obtain the slope, for the log-log period vs damping length plot, for each of the cases. With this study, we will be able to get a range of this slope.

4.1 Data

We use two sequences of EUV images taken by the Atmospheric Imaging Assembly (AIA) on board the *Solar Dynamics Observatory* (SDO) in 171 Å channel for this study. The date of observations are 1 November 2015 and 14 October 2015.

Coronal hole was present near the southern pole on both days. On 1 November 2015, we have considered an area of 1820 pixels by 540 pixels near the south pole, centered at (-31.9″, -1034.4″). A sequence of 600 images of 2 hours duration, starting from 16 : 00 UT are used for the study (Figure 4.2). The other image sequence of 2 hours duration is observed on 14 October, 2015. A 1727 pixel by 596 pixel subfield, centered at (59.4″, -1021.2″), near the coronal hole at the southern pole is chosen for this study. The standard *aia_prep.pro* routine is used to process the initial level 1.0 data for correction of roll angles. The final cadence of the data is 12 s. with a pixel scale of $\approx 0.6''$.

4.2 Analysis and Results

In-order to find out the global behavior of these waves in the field of view (FOV) (in plumes and interplumes), we make use of the powermaps of those regions. One such examples is shown in Figure 4.1. The powemap has been constructed by using the wavelet transformation (Torrence and Compo 1998) at every pixel in the FOV and then summing the wavelet power across different period bands. We see that the longer periods are propagating higher compared to the smaller periods (in accordance with Gupta (2014)). We also notice that the finer structures are revealed more clearly as we mover towards longer periods.

Next, we used artificial slits of length 350 pixels on plumes and interplumes as shown by rectangular boxes in Fig. 4.2 to generate the time-distance maps. The width of the slits has been varied (30 or 20 pixels) depending on the width of the structure. In a time distance map, the intensity along the slit is stacked over time. One of such examples, for one of the plume and the interplume structures, is shown in different panels of Figure 4.3.

To bring out the features more clearly, these time-distance maps are enhanced by subtracting a running average of 100 frames (20 mins) from the orginial map. The enhanced map (Figure 4.3) shows the presence of the disturbances as alternating bright and dark inclined ridges. The ridges are slanted with a positive slope

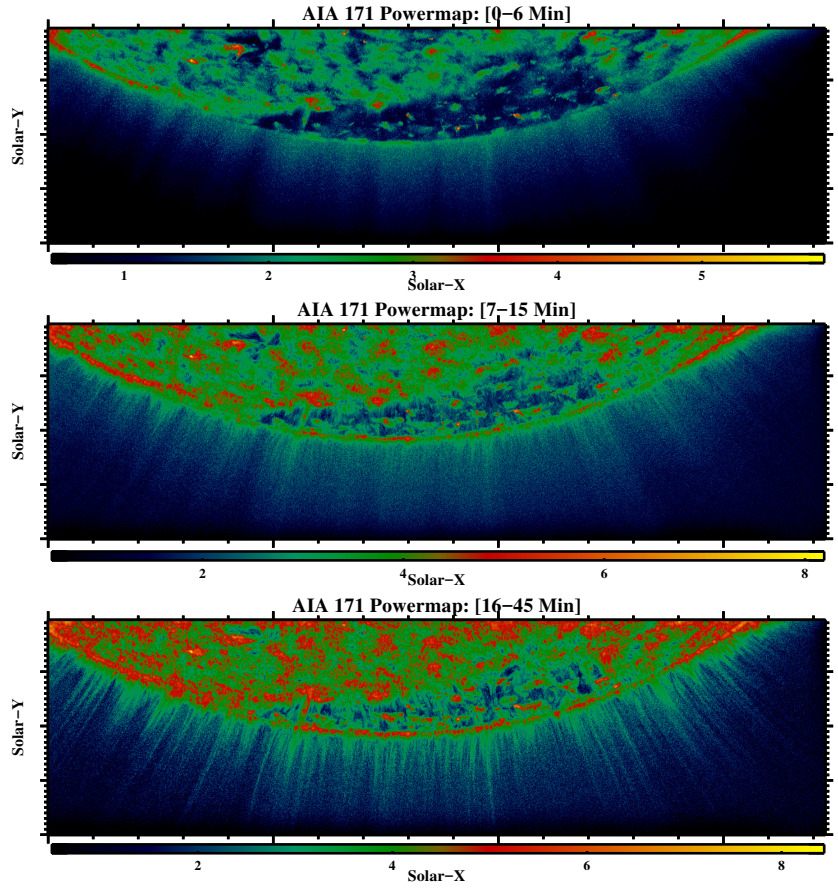

FIGURE 4.1: Powemaps showing the overall power distributions in the specific period bins. The date of observation is 14 Oct.

indicating the direction of propagation as radially outwards (along the slits). A closer look at the figure reveal the ridge intensities are higher near the limb (i.e near the zero length of the time-distance map) and then the intensities gradually decrease as distances from the limb increase. This highlights the fact these waves decay as they propagate along the structure.

As our main aim is to investigate the frequency dependent damping of these waves, we convert these time-distance maps into period-distance maps by performing wavelet analysis at each spatial position in the time-distance map. Total power, of a given period, over the entire duration of observation is calculated at each spatial position and is presented in the upper left panel of Figure 4.4. From the plot, we notice that the power is highest, for any given period, at the bottom of this plot (solar limb) but it fades away as one moves away from it. We also note that the power is not evenly distributed at all periods, rather it is concentrated at

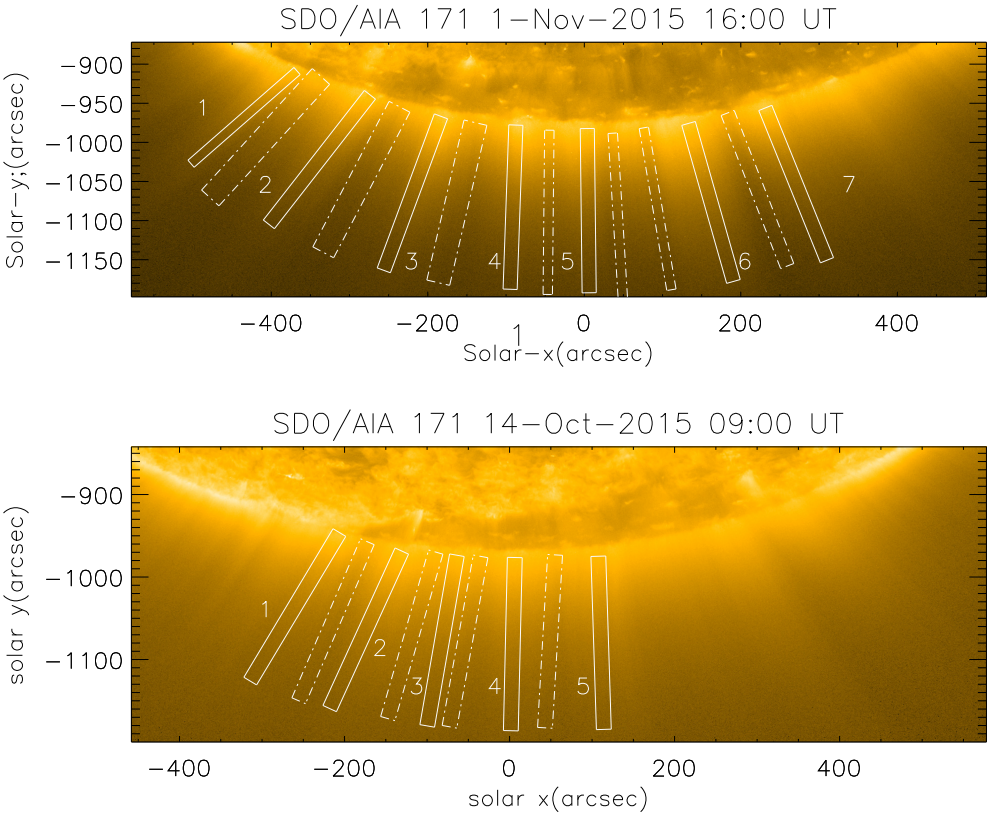

FIGURE 4.2: Snapshots of the regions of ineterst on 2015 November 1 (left panel) and that on 2015 October 14. The position of the artificial slits on plumes (marked by solid boxes) and interplumes (marked by dashed boxes) are shown. Damping of slow magnetoacoustic wave along these structures are studied.

some specific periods with some distribution. To identify these periods with significant powers, we constructed a 'template spectrum' by using the average light curve from bottom 5th to 10th pixels and over-plotted it (solid black curve) on the period-distance map of Figure 4.4. The peaks, of this template spectrum, are estimated using a routine `gt_peaks.pro` available in Solar-Soft pacakge. After identifying the peaks, we have binned 3 pixels around the peak, and computed the amplitude variation with the distance for the identify periods individually. The amplitude is defined as the square root of power. Such variations of the amplitude with the distance, for different identified periods, are shown in Figure 4.4.

We see that the amplitude falls off very rapidly with the distance and also these

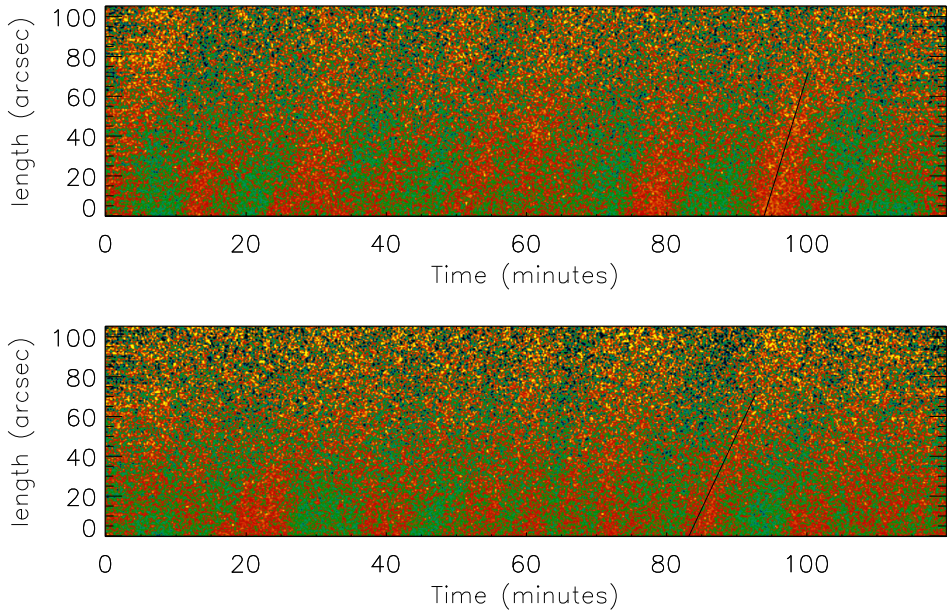

FIGURE 4.3: The time distance maps along plume and interplume structure on 1 November 2015. The alternate bright and dark ridges with positive slopes indicate upwardly propagating waves. The Black line on the ridge gives estimation of propagation speed. The *Upper Panel* shows the variation along plume (slit 1), *Lower Panel* is for the variation along interplume (slit 4).

rate of decrements are different for different periods. In order to get a quantitative measure, we fit these amplitude-distance curves with an exponential function (following Krishna Prasad *et al.* (2014); Mandal *et al.* (2016)) of the form $A(y) = A_0 e^{-y/L_d} + C$. L_d is taken as the measure of damping length (Fig.4.4). The period of oscillation and corresponding damping lengths are indicated in each panel. The oscillation periods along with the fitted parameters, as obtained for both the datasets, are listed in Table 4.1 and Table 4.2.

4.2.1 Slope Measurements

As we have obtained the damping lengths for the individual periods, in this section we calculate the slopes from the log-log period vs damping length plot.

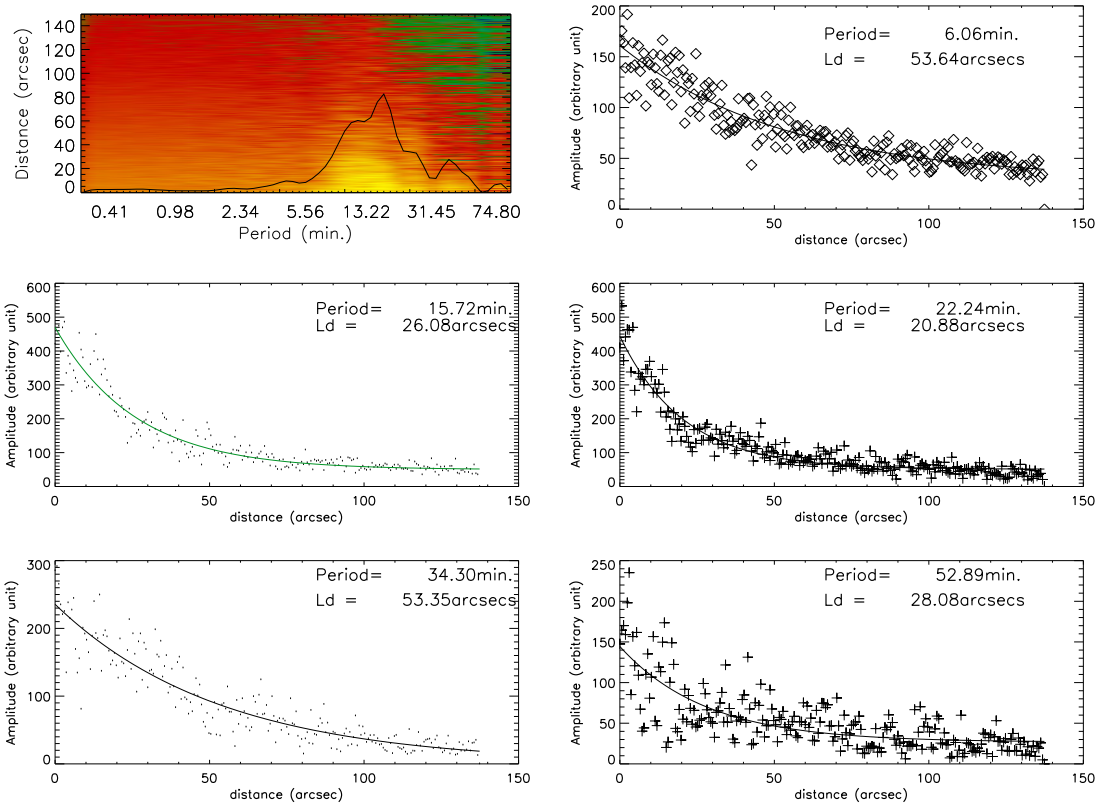

FIGURE 4.4: The period distance map along Slit 1 on plume structure on 1 Nov 2015, is shown in the top left panel. The average light curve, used to identify peak periodicities is overplotted. The other panels show the variation of damped intensity for different periods. The fitted curves are overplotted and corresponding damping lengths are indicated in each panel.

The damping length versus periods of oscillations, for both plumes and interplumes, are plotted in a log-log scale for both of the observations in Fig.4.6. Different symbols are used to highlight the measurement from the plume interplume regions. In order to calculate the slope, the points are fitted with a straight line. The slopes are found to be -0.177 ± 0.021 for 1 Nov 2015 and -0.219 ± 0.019 for 14 Oct 2015. The slope values indicate that the damping lengths decrease as the period of oscillation increases. These values are also consistent with the result obtained by Krishna Prasad *et al.* (2014).

In order to check for the individual contributions of the plumes and interplumes towards the slope values, we separately draw the log-log period vs damping length plots as shown in Fig. 4.8. Upon calculating the slopes from these curves, we note that there no significance differences (considering the error bars) on the nature of

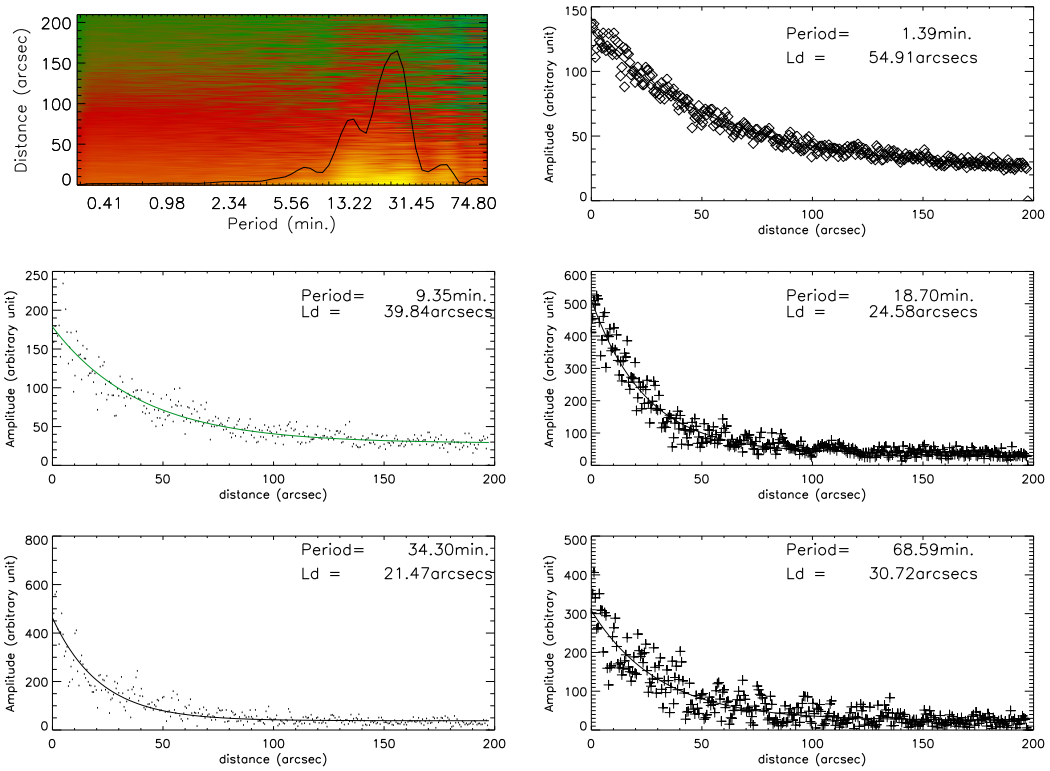

FIGURE 4.5: The period distance map along 3rd interplume from the left on 14 Oct is shown in the top left panel. The average light curve, used to identify peak periodicities is overplotted. The other panels show the variation of damped intensity for different periods. The fitted curves are overplotted and corresponding damping lengths are indicated in each panel.

frequency dependency for damping along these structures. The slopes are found to be -0.222 ± 0.017 along plumes and -0.183 ± 0.034 along interplumes. The variations show similar nature as seen along plumes (Fig. 4.9) and interplumes (Fig. 4.10) on different observation days.

4.3 Summary and Conclusions

Study of frequency dependent damping of slow magneto-acoustic waves are important inorder to understand their contribution towards the solar wind acceleration. In this work we analyzed multiple data sets indorer to probe this frequency dependent damping scenario in polar plumes and inter-plumes. Below we summarize

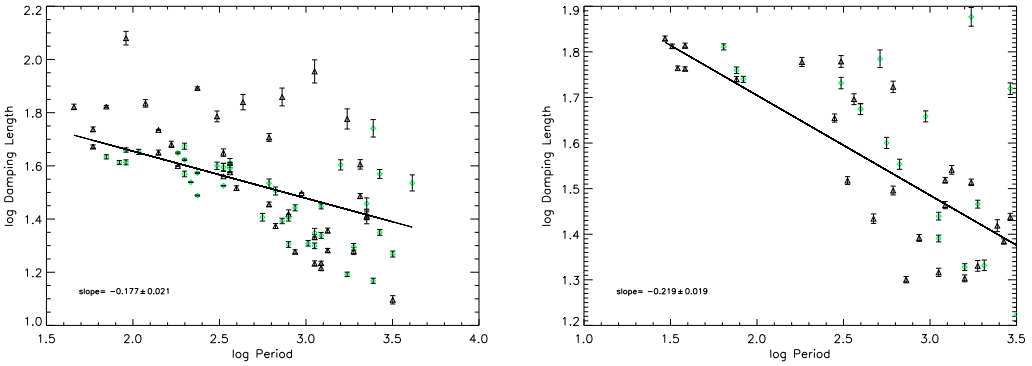

FIGURE 4.6: The period (sec.) versus damping length (arcsecs) in log-log scale. The slope value and error is indicated. Triangles are for plumes, diamonds are for interplumes. The *Left Panel* shows the variation on 1 nov 2015, *Right Panel* is for 14 Oct 2015.

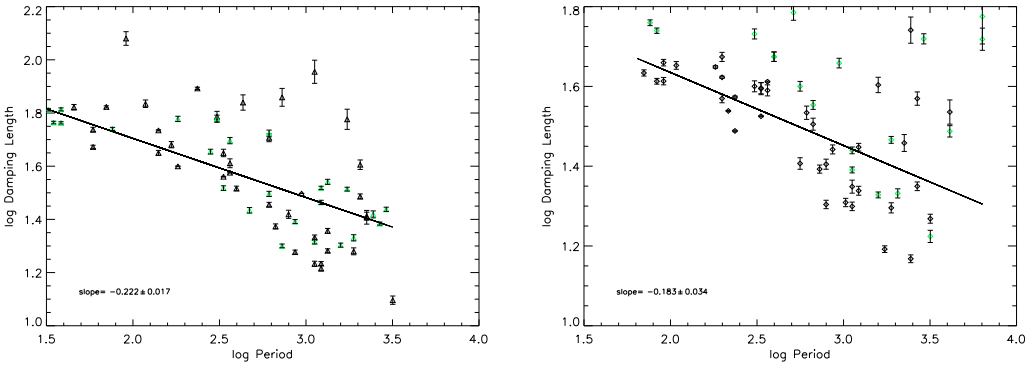

FIGURE 4.7: The period (sec.) versus damping length (arcsecs) in log-log scale. The slope value and error is indicated. Triangles are for plumes, diamonds are for interplumes, 'Black' is for observations on 1 Nov and 'green' is for observations 14 Oct. The *Left Panel* shows the variations along Plumes , *Right Panel* is along interplumes.

the key findings from our analysis:

• We have identified 12 polar plume and interplume structures using AIA 171Å image sequences. In both the datasets, we spot the presence of coronal holes.

• Powermap analysis shows that the long period oscillations are able to reach greater heights from the solar limb. On the otherhand, the oscillations with smaller periods decay fast. This shows the frequency dependent nature of the wave damping.

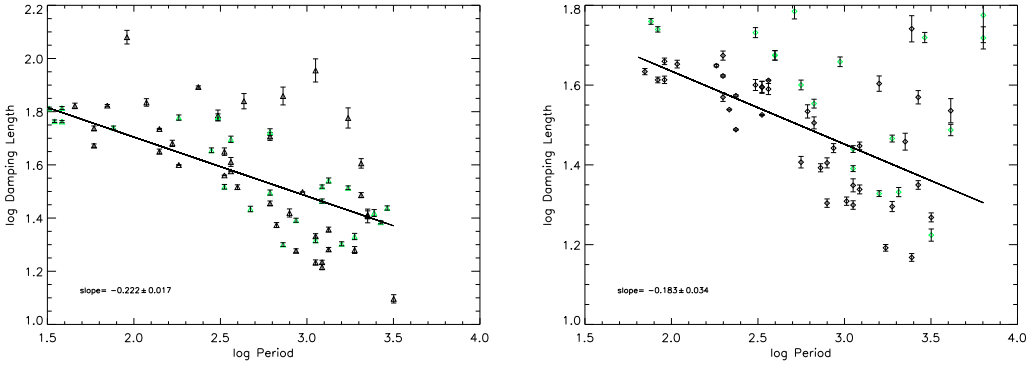

FIGURE 4.8: The period (sec.) versus damping length (arcsecs) in log-log scale. The slope value and error is indicated. Triangles are for plumes, diamonds are for interplumes, 'Black' is for observations on 1 Nov and 'green' is for observations 14 Oct. The *Left Panel* shows the variations along Plumes , *Right Panel* is along interplumes.

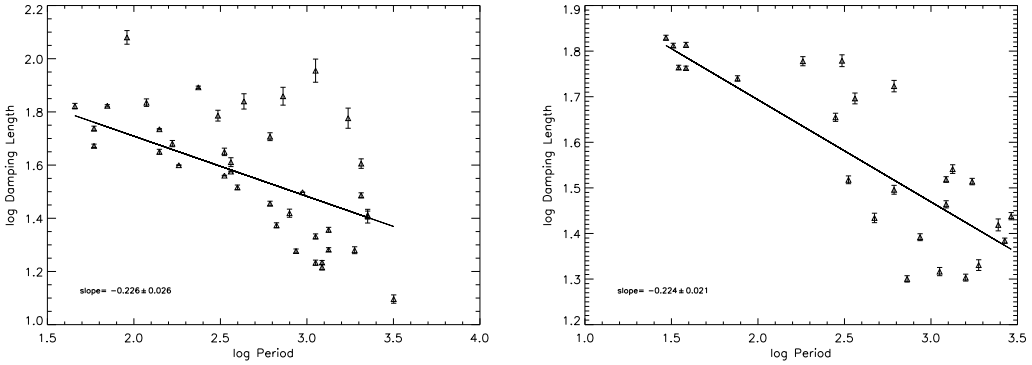

FIGURE 4.9: Variation of damping length with periods in log-log scale,as obtained for plumes. *Left Panel* For observations on 1 Nov 2015 and *Right Panel* for those on 14 Oct 2015.

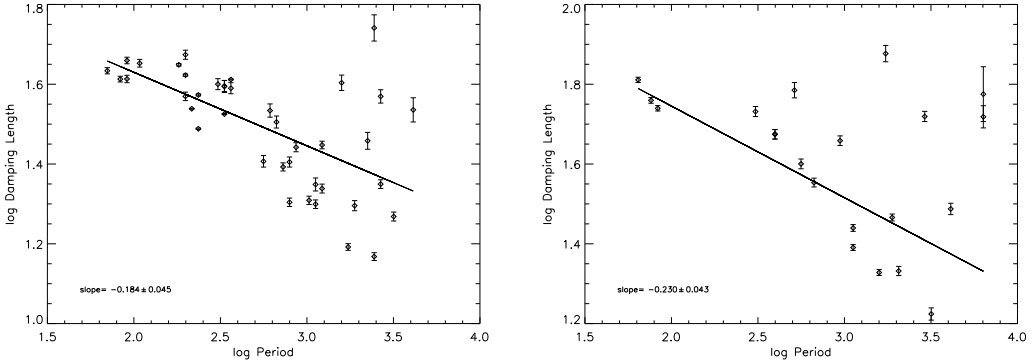

FIGURE 4.10: Variation of damping length with periods in log-log scale,as obtained for interplumes. *Left Panel* For observations on 1 Nov 2015 and *Right Panel* for those on 14 Oct 2015.

• We have generated the period-distance maps inorder to separate and compute the power for individual periods. This also allows us follow the evolution of the power, for a given period, along these plume/interplume structures. We fit a exponentially decaying function to model this power/amplitude decrement along the loop.

• To find out the powerlaw, we draw the log-log period vs damping length plots and found these slope value to be small but negative (-0.177 to -0.226). When the slopes are calculated separately, for the plume and the interplume regions, we note that the values are not significantly different from the previous values where both have been considered at once. This hints towards a common mechanism working on both these regions though the physical properties of the plumes and interplumes are quiet different (Wilhelm 2006). Since the expected slope value, from the linear wave damping theory (taking thermal conduction as dominant mechanism), is 2, we conclude that there must be different damping agent, other than the thermal conduction, working on these structures.

In conclusion, we have used modern high resolution solar images to perform a statistical analysis on the frequency dependent damping of the slow magnetoacoustic waves on the polar plumes/interplumes. Our analysis confirms the differences in the damping mechanisms acting on these structures compared to their ondisc counterparts. Since all the data sets used in this study have coronal holes, we would want to explore the similar scenario in the polar structures when there are no coronal holes. Thus we will be able to estimate the contribution of the local magnetic topology in the calculatuion of the powerlaw index apart from improving the overall statistics.

TABLE 4.1: The damping lengths for different periodicities are listed. This is for the observations on 1 Nov 2015.

Structure/ Slit no.	Period (minutes)	L_d (arcsec)	Structure/ Slit no.	Period (minutes)	L_d (arcsec)
Plume/1	6.0	40.83 ± 1.57	Interplume/1	1.8	44.94 ± 1.00
Plume/1	15.7	31.47 ± 0.04	Interplume/1	3.3	41.97 ± 0.27
Plume/1	22.2	22.74 ± 0.48	Interplume/1	5.1	39.83 ± 1.26
Plume/1	34.3	40.33 ± 1.66	Interplume/1	13.2	20.14 ± 0.49
Plume/1	52.8	12.48 ± 0.45	Interplume/1	20.4	28.03 ± 0.62
Plume/2	2.7	47.95 ± 1.30	Interplume/1	44.5	37.11 ± 1.43
Plume/2	6.0	37.65 ± 0.15	Interplume/2	1.5	45.66 ± 0.86
Plume/2	10.2	28.53 ± 0.58	Interplume/2	3.0	44.54 ± 0.33
Plume/2	18.7	17.10 ± 0.38	Interplume/2	5.5	39.41 ± 1.27
Plume/2	34.3	30.64 ± 0.67	Interplume/2	9.3	25.51 ± 0.85
Plume/3	0.9	54.63 ± 1.13	Interplume/2	17.1	20.37 ± 0.49
Plume/3	2.3	54.30 ± 0.28	Interplume/2	37.4	28.72 ± 1.40
Plume/3	5.5	44.64 ± 1.44	Interplume/3	1.1	43.03 ± 0.77
Plume/3	10.2	50.91 ± 1.73	Interplume/3	3.9	37.43 ± 0.22
Plume/3	22.2	19.15 ± 0.32	Interplume/3	6.0	38.91 ± 1.24
Plume/3	37.4	25.83 ± 0.89	Interplume/3	10.2	34.20 ± 1.31
Plume/4	0.9	47.03 ± 0.70	Interplume/3	28.8	15.56 ± 0.30
Plume/4	3.0	39.77 ± 0.14	Interplume/4	3.3	47.20 ± 1.24
Plume/4	6.6	32.83 ± 0.66	Interplume/4	6.0	40.92 ± 0.13
Plume/4	14.4	18.92 ± 0.33	Interplume/4	13.2	25.41 ± 0.74
Plume/4	20.3	17.14 ± 0.29	Interplume/4	20.4	21.80 ± 0.56
Plume/5	2.3	44.68 ± 0.95	Interplume/4	44.5	22.37 ± 0.56
Plume/5	5.5	36.35 ± 0.11	Interplume/5	3.3	37.12 ± 0.91
Plume/5	11.1	23.64 ± 0.51	Interplume/5	5.5	33.52 ± 0.10
Plume/5	18.7	21.47 ± 0.47	Interplume/5	11.1	32.01 ± 1.11
Plume/5	31.4	19.05 ± 0.57	Interplume/5	18.7	19.92 ± 0.49
Plume/6	1.5	120.28 ± 7.10	Interplume/5	40.7	14.72 ± 0.33
Plume/6	3.9	78.09 ± 0.78	Interplume/6	1.3	41.01 ± 0.68
Plume/6	7.2	69.10 ± 4.58	Interplume/6	3.6	34.56 ± 0.09
Plume/6	13.2	26.25 ± 0.92	Interplume/6	14.4	27.67 ± 0.72
Plume/6	20.3	16.43 ± 0.38	Interplume/6	31.4	19.75 ± 0.58
Plume/6	37.4	25.58 ± 1.52	Interplume/7	1.5	41.04 ± 0.88
Plume/7	0.7	66.33 ± 1.58	Interplume/7	3.9	30.79 ± 0.13
Plume/7	1.1	66.52 ± 0.63	Interplume/7	5.5	39.29 ± 1.36
Plume/7	1.9	68.36 ± 2.22	Interplume/7	12.1	24.70 ± 0.58
Plume/7	5.1	61.08 ± 2.86	Interplume/7	18.7	22.32 ± 0.84
Plume/7	12.1	72.27 ± 5.59	Interplume/7	26.4	40.15 ± 1.78
Plume/7	18.7	90.18 ± 9.04	Interplume/7	40.8	55.10 ± 4.17
Plume/7	28.8	59.75 ± 5.22			

TABLE 4.2: The damping lengths for different periodicities are listed. This is for the observations on 14 Oct 2015.

Structure Slit no.	Period (minutes)	L_d (arcsec)	Structure/ Slit no.	Period (minutes)	L_d (arcsec)
Plume/1	0.6	57.92 ± 0.35	Plume/5	0.5	67.51 ± 0.85
Plume/1	1.3	54.96 ± 0.48	Plume/5	12.1	19.97 ± 0.32
Plume/1	5.5	32.94 ± 0.74	Plume/5	26.4	20.10 ± 0.35
Plume/1	18.7	20.72 ± 1.73	Plume/5	44.5	24.22 ± 0.32
Plume/2	0.5	64.92 ± 0.43	Interplume/1	6.6	47.26 ± 1.29
Plume/2	5.1	60.11 ± 1.27	Interplume/1	15.7	45.55 ± 1.27
Plume/2	10.2	52.87 ± 1.61	Interplume/1	28.8	75.30 ± 3.55
Plume/2	20.4	32.99 ± 1.60	Interplume/1	52.9	16.75 ± 0.59
Plume/2	28.8	32.65 ± 2.12	Interplume/2	1.1	64.71 ± 0.99
Plume/3	0.6	65.11 ± 0.48	Interplume/2	8.6	60.96 ± 2.70
Plume/3	3.0	59.96 ± 0.85	Interplume/2	26.4	21.28 ± 0.36
Plume/3	6.0	49.68 ± 0.94	Interplume/3	1.4	54.91 ± 0.85
Plume/3	10.2	31.32 ± 0.95	Interplume/3	9.3	9.84 ± 1.12
Plume/3	22.2	34.77 ± 1.91	Interplume/3	18.7	24.58 ± 0.42
Plume/3	48.5	27.41 ± 0.50	Interplume/3	34.3	21.47 ± 0.57
Plume/4	0.6	58.10 ± 0.65	Interplume/4	1.3	57.49 ± 0.96
Plume/4	4.7	45.17 ± 0.93	Interplume/4	5.1	53.89 ± 1.56
Plume/4	7.8	27.17 ± 0.65	Interplume/4	11.1	35.77 ± 0.91
Plume/4	14.4	24.65 ± 0.43	Interplume/4	18.7	27.52 ± 0.54
Plume/4	20.4	29.10 ± 0.53	Interplume/4	31.4	29.24 ± 0.58
Plume/4	31.4	21.41 ± 0.58	Interplume/4	48.5	52.39 ± 1.54
Plume/4	40.8	26.23 ± 0.79			

Chapter 5

Flows and Waves in Braided Solar Coronal Magnetic Structures

We study the high frequency dynamics in the braided magnetic structure of an active region (AR 11520) moss as observed by High-Resolution Coronal Imager (Hi-C). We detect quasi periodic flows and waves in these structures. We search for high frequency dynamics while looking at power maps of the observed region. We find that shorter periodicites (30 - 60 s) are associated with small spatial scales which can be resolved by Hi-C only. We detect quasi periodic flows with wide range of velocities from 13 - 185 km s^{-1} associated with braided regions. This can be interpreted as plasma outflows from reconnection sites. We also find presence of short period and large amplitude transverse oscillations associated with braided magnetic region. Such oscillations could be triggered by reconnection or such oscillation may trigger reconnection[1].

[1]This study has been published in Pant *et al.* (2015)

5.1 Introduction

The understanding of the heating mechanism/s of the solar corona is one of the main challenges in solar physics. Two types of mechanisms are well accepted, namely impulsive heating by nanoflares (Parker 1988) and wave heating by dissipation of waves.

High Resolution Coronal Imager (Hi-C) (Kobayashi *et al.* 2014) provided unprecedented details of active region moss at small spatial scales. It has diffraction limited spatial resolution of 0.3″and cadence of ∼5.5 s. Hi-C has revealed many new features of the corona at small spatial scales (Peter *et al.* 2013; Morton and McLaughlin 2013; Winebarger *et al.* 2014). Antiochos *et al.* (2003) reported weak intensity variation ∼10% in active region moss over period of hours using Transition Region and Coronal Explorer (TRACE). They rule out the possibility of impulsive heating and also conjectured that high-frequency heating could be the source of observed variability. Brooks and Warren (2009) confirmed the findings of Antiochos *et al.* (2003) using Hinode, EIS observation. They did not find strong flows and short term variability in moss region and concluded that heating is quasi-steady. High temporal and spatial resolution of Hi-C gave a new insight in understanding the mechanism of coronal nanoflare heating. Winebarger *et al.* (2013) studied inter-moss loops using Hi-C and reported that these cool and dense loops are the result of impulsive heating of magnitude similar to that of coronal nanoflares. Testa *et al.* (2013) have reported the variability ∼ 15–20 s in the active moss region at the foot points of bright hot coronal loops and attributed these as the signature of impulsive nanoflare events. Hi-C observations have revealed small scale brightening in EUV of duration 25 s and of length scale 0.68 Mm (Régnier *et al.* 2014). Cirtain *et al.* (2013) have reported the first evidence of magnetic field braiding and axial twist from Hi-C observations. They have estimated the free energy available ∼ 10^{29} ergs. The release of this energy due to magnetic reconnection can heat up the loop. A non-linear force free field reconstruction of magnetic field lines corresponding to the same field of view of Hi-C reveals the braiding and twisting of magnetic fields (Thalmann *et al.* 2014). They estimated ∼ 100 times more free energy than estimated by Cirtain *et al.* (2013). Recently Tiwari *et al.* (2014) has observed a subflare event at this region just after the Hi-C observations

from different channels of Atmosphearic Imaging Assembly (AIA) on board Solar Dynamic Observatory (SDO).

Transverse oscillations in corona have been reported by Tomczyk *et al.* (2007) using Coronal Multi channel Polarimeter (COMP) data and McIntosh *et al.* (2011) using AIA on Solar Dynamic Observatory (SDO). They have reported the typical velocity amplitude of $\sim$5 km s^{-1}. After the advent of Hi-C Morton and McLaughlin (2013, 2014) reported transverse waves in active region moss with velocity amplitude as high as 11 km s^{-1} and mean periodicity of $\sim$ 50 s. They have estimated that about 15% of wave energy is carried to transition region from chromosphere.

We focus on high frequency dynamics of active region moss and braided magnetic region as seen from Hi-C, with particular emphasis on the reconnection sites. Recurrent reconnections and waves both can contribute significantly to the heating. We search for the presence of flows which can be attributed as a signature of reconnection within the braided magnetic region.

5.2 Observations and Data Analysis

Hi-C took high resolution images of the Solar corona in Fe XII 193 Å passband. The observations were performed on 11 July 2012 at 18:52:09 UT with the cadence of $\sim$ 5.5 s and pixel resolution of $\sim$ 0.103 $''$pix^{-1} for a duration of 200 s. We used level 1.5, 4K X 4K dataset. This dataset is corrected for pointing drift, spacecraft jitter and atmospheric absorption (Kobayashi *et al.* 2014). We align datacube using cross correlation to remove residual drifts and to achieve sub-pixel accuracy (Morton and McLaughlin 2013, 2014).

We also use simultaneous imaging data as recorded by AIA/SDO with EUV narrow band ($\sim$0.6$''$pixel^{-1}, 12 s cadence).

Fig. 5.1 (a) shows AIA 193 Å full disk image. Small black rectangle shows full Hi-C field of view (FOV). Figs.5.1 (b) and (d) show the zoomed view of region marked

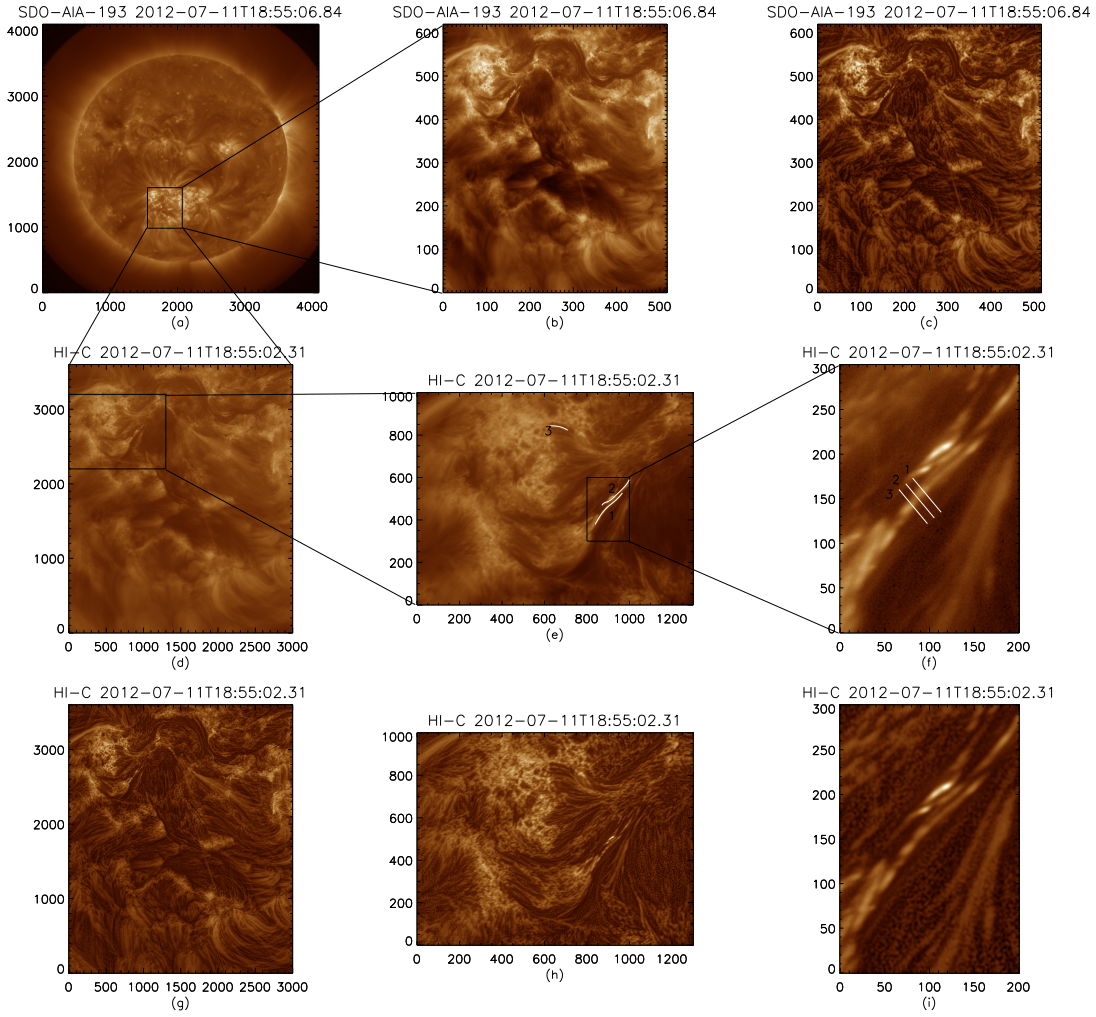

FIGURE 5.1: *Top panel*: (a):AIA 193 Å full disk image. Black rectangle represents the full Hi-C FOV. (b): AIA 193 Å having same FOV as Hi-C. (c):Reconstructed image, using multi gaussian normalized filter, with the same FOV as shown in (b). *Middle Panel*:(d): Full FOV of HI-C image. Region under consideration is indicated with black rectangle. (e): Three curved slits positions, indicated by white curves, are shown which are used for time distance maps. (f): Three slits are placed perpendicular to the threads as indicated with white lines for the detection of transverse motions. *Bottom panel*: Reconstructed images, using multi gaussian normalized filter, with the same FOV as shown in middle panel.

with black rectangle in Fig.5.1 (a) as seen in AIA and Hi-C respectively. Black rectangle in Fig.5.1(d) marks the region of interest (ROI) for further analysis. Fig.5.1(e) shows the zoomed view of ROI and curved white slices which are used for creating time-distance maps. Fig.5.1(f) shows zoomed view of subfield of ROI as marked in Fig.5.1(e). Due to high noise in the Hi-C images we filter each image into high and low spatial frequency components. High frequency image shows significant small scale structures therefore, we filter high frequency component further. We iterate it up to three times and the resulting high frequency image contains only uncorrelated noise. Finally, we subtract high frequency image from original image. Furthermore, in order to bring out structures at different spatial scales, we use normalized multi gaussian filter (Morton and McLaughlin 2014) to filtered images. We choose width of gaussian filter to be 11, 21, 41 and 81 pixels for ROI and 21, 41, 101, 201 and 1001 pixels for Hi-C full FOV. We add gaussian filtered images of different spatial scales with equal weight to obtain a single multi gaussian filtered image. Above procedure is repeated for AIA 193 Å image with width of gaussian filter to be 11, 21, 41 and 81 pixels and filtered image is shown in Fig.5.1 (c). Filtered images of the corresponding images of Hi-C in Fig. 5.1 (middle panel) are shown in the bottom panel of Fig.5.1.

5.3 Results

First we will focus on the distribution of power as calculated from wavelet methods to identify the locations where the high frequency dynamics are present.

5.3.1 Power and Wavelet maps

We perform wavelet analysis at each pixel location of Hi-C ROI and corresponding FOV of AIA 193 Å . Fig. 5.2 top left panel shows the power map of Hi-C ROI in 30- 60 s and filtered image of Hi-C overplotted with the pixel positions marked in green where global significance level of power is greater than 95 % confidence level (Torrence and Compo 1998) for a white noise process (see, Fig. 5.2 bottom

left panel). We limit ourselves to 30- 60 s interval because we note that for higher frequencies (15-30 s), wavelet starts picking up noise and it is difficult to distinguish between noise and true signal variation. To limit the noise we discard isolated pixel locations and set threshold as 9 pixels on the size of detected regions over global significance level. We carry out similar analysis for AIA 193 Å . Cadence of AIA is low (12 s) as compared to Hi-C (5.4 s) thus the data points will be less due to finite duration of time series. Therefore we choose longer time series of 10 minutes starting from 18:50:00 UT to 18:60:00 UT for AIA 193 Å . We find that even after choosing longer time series significant power in shorter periodicities (30-60 s) is absent in AIA FOV (Fig. 5.2 bottom middle panel) while significant power is present in longer periodicities (120-180 s) as shown in Fig. 5.2 bottom right panel. For AIA we set the threshold as two pixels on the size of detected regions over global significance level.

Wavelet maps of pixel locations marked as A and B in Hi-C FOV (see Fig. 5.2 bottom left panel) are shown in Figs. 5.3 (a) and (b) respectively. Fig. 5.3 (a) Top panel shows original Hi-C light curve without any smoothing at position marked as A with error bars. Errors in data points are calculated as $\sqrt{0.23F + 588.4}$ (Morton and McLaughlin 2013), where F is the intensity value at pixel position A. The bottom left panel shows wavelet result which displays temporal evolution of different periodicities. Power is plotted in inverted colours therefore, black indicates the region of strongest power. Cross hatched region is called cone of influence. This region can suffer from edge effects therefore, periods observed in this region are not reliable. Bottom right panel is the global wavelet plot which is the time average of the wavelet plot. The horizontal dashed line is the cutoff above which edge effects come into play and dotted line marks 95 % significance level for a white noise process. We find that significant power peaks at ∼52 sec followed by a second highest peak ∼13 s. The second peak is not significant and it could be due to small variations in light curve which are within the error limits. Similar analysis is repeated for pixel position B where maximum significant power is ∼48 s and second peak ∼22 s (see Fig. 5.3 (b)). This analysis reveals that there is an indication of periodicities of around 15-30 s but they are not significant. Such periodicities could be the manifestation of small variation of intensities which are within error limits.

Fig. 5.3 (c) shows the wavelet map of AIA 193 Å at pixel location marked as C (see Fig. 5.3 bottom right panel). We choose longer time series of ten minutes starting from 18:50:00 UT. Fig. 5.3 (c) top panel shows the AIA light curve with error estimates. Errors are calculated as $\sqrt{0.06F + 2.3}$ (Yuan and Nakariakov 2012), where F is the intensity value at a given pixel position. Intensity values marked in red are co-temporal with Hi-C observations. We find that significant power peaks $\sim$ 140 s. However, shorter periodicities are also present as small peaks at $\sim$ 59 s and 30 s. To investigate the presence of shorter periodicities below 60 s, we perform wavelet analysis of pixel location at C for the duration co-temporal with Hi-C observations as shown in Fig. 5.3 (d). We note that periods $\sim$ 60 s do exist but they are below significance level.

It is worthwhile to note that power map reveals the finer structures in moss and braided magnetic region where power is concentrated. In Fig 5.2 (bottom left panel) it is evident that the significant power (pixels marked in green) within 30-60 s are lying over active moss and braided magnetic field region in Hi-C FOV while significant power at these periods is absent in AIA 193 Å (Fig. 5.2 (bottom middle panel)). However significant power at longer periods (120-180 s) are lying over active moss and braided magnetic field region in AIA FOV (Fig. 5.2 (bottom right panel)). It suggests that shorter periodicities (30- 60 s) are present in smaller spatial scales which can not be resolved by AIA. Therefore, such short periodicites are almost absent in AIA 193 Å FOV.

5.3.2 Quasi periodic flows and Transverse Oscillation

To study the flow within the braided magnetic region, we place three artificial curved slices along some specific threads as marked in Fig. 5.1 (e). Corresponding to each of three slices a two dimensional time-distance diagram (x-t) is created (see Fig. 5.4), where x axis represent the time in seconds and y axis represent the distance along slit in Mm. Thick black region in x-t map (Fig. 5.4 top panel) represents the data gap. Ridges where structures can be resolved, gaussian curve along the column is fitted and the mean values with one sigma error bars is estimated. The ridge is then fitted with straight line. For extended or faint ridges

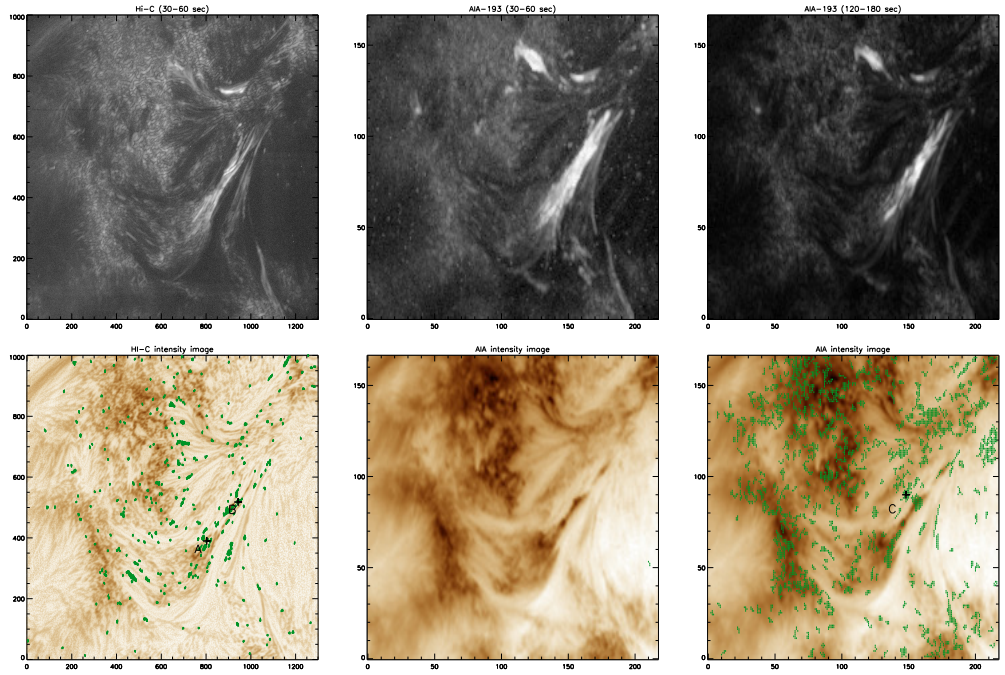

FIGURE 5.2: *Top panel*: left: Power map of Hi-C region of interest plotted in logarithmic scale for 30-60 s. Middle: Power map of AIA 193 Å region of interest plotted in logarithmic scale for 30-60 s periods. Right: Power map of AIA 193 Å region of interest plotted in logarithmic scale for 120-180 s. *Bottom panel*: left: Filtered inverted intensity image of Hi-C overplotted with pixels positions having significant power greater than 95% confidence level in green. Middle and Right: inverted intensity image of AIA 193 Å overplotted with pixels positions with significant power greater than 95% confidence level in green.

the gaussian curve fitting is not feasible thus we fitted them visually with straight line. Fig. 5.4 bottom panel shows running difference x-t maps corresponding to maps in Fig. 5.4 top panel.

Several ridges are seen in x-t maps with different slopes at different times and with different lifetime as shown in Fig. 5.3. Slopes of the ridges gives an estimate of velocities of plasma outflow. The plasma outflows are found to be quasi periodic with large range of velocities from 13 km s^{-1} - 185 km s^{-1} (see Fig. 5.4) within our ROI which could be closely associated with reconnection sites .

Due to high spatial resolution Hi-C also helps us to probe transverse oscillations associated with fine threads. For that we place three transverse slices across one highly braided structure as marked in Fig. 1 (f). For transverse slices, method of

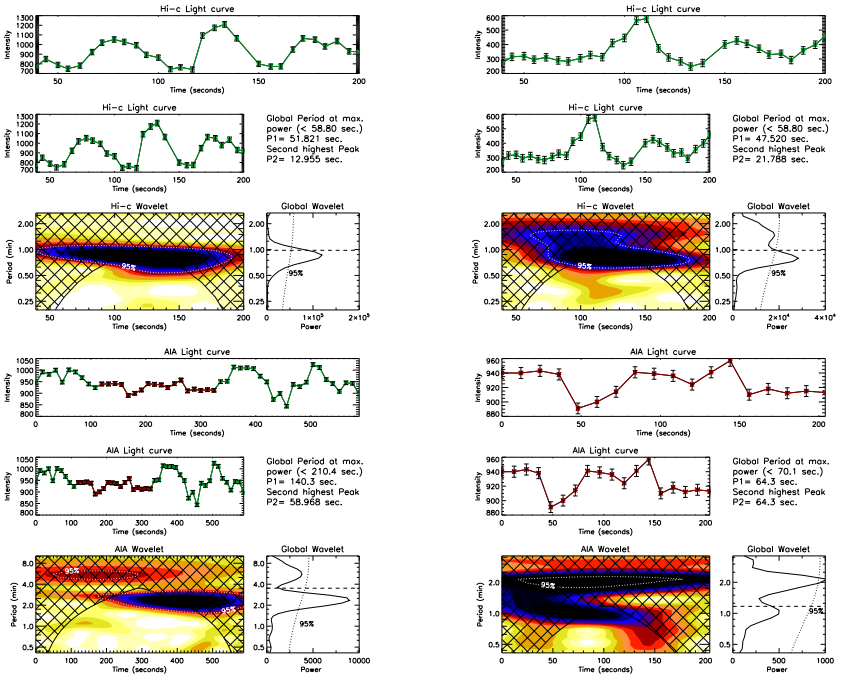

FIGURE 5.3: (a): Wavelet map of Hi-C intensity at pixel position 'A' marked in Fig. 2 bottom left panel. (b): Wavelet map of Hi-C intensity at pixel position 'B' marked in Fig. 2 bottom left panel. (c): Wavelet map of AIA intensity at pixel position 'C' marked in Fig. 2 bottom Right panel. Data points marked in red are co-temporal with Hi-C duration. (d): Wavelet map of AIA intensity at pixel position 'C' marked in Fig. 2 bottom Right panel co-temporal with Hi-C duration.

analysis is same as we adopted for curved slices. The x-t map (Fig. 5.5) is fitted with harmonic curve represented by the formula

$$y = a + bsin(\omega t + \phi), \tag{5.1}$$

where a is constant, b is amplitude, ω is the frequency and ϕ is the phase. The amplitude of oscillation is found to be 110±109 km (111±102 km and 67±105 km) and period of oscillation is found to be 73±33 s (63±17 s and 53±22 s) for first (second and third slice). The velocity amplitude is found to be 9.4±13 km s^{-1} (11±13 km s^{-1} and 8 ± 15 km s^{-1}). We note significant brightening along the loop, quasi periodic flows and transverse oscillations occur almost at same time for curved slice 1. The large error bars in velocity is because of large errors in the amplitude measurement. Errors in the amplitude estimation is large because one sigma error bars in the x-t map columns are larger than the observed amplitude of structure. Since we have aligned the data with sub-pixel accuracy so

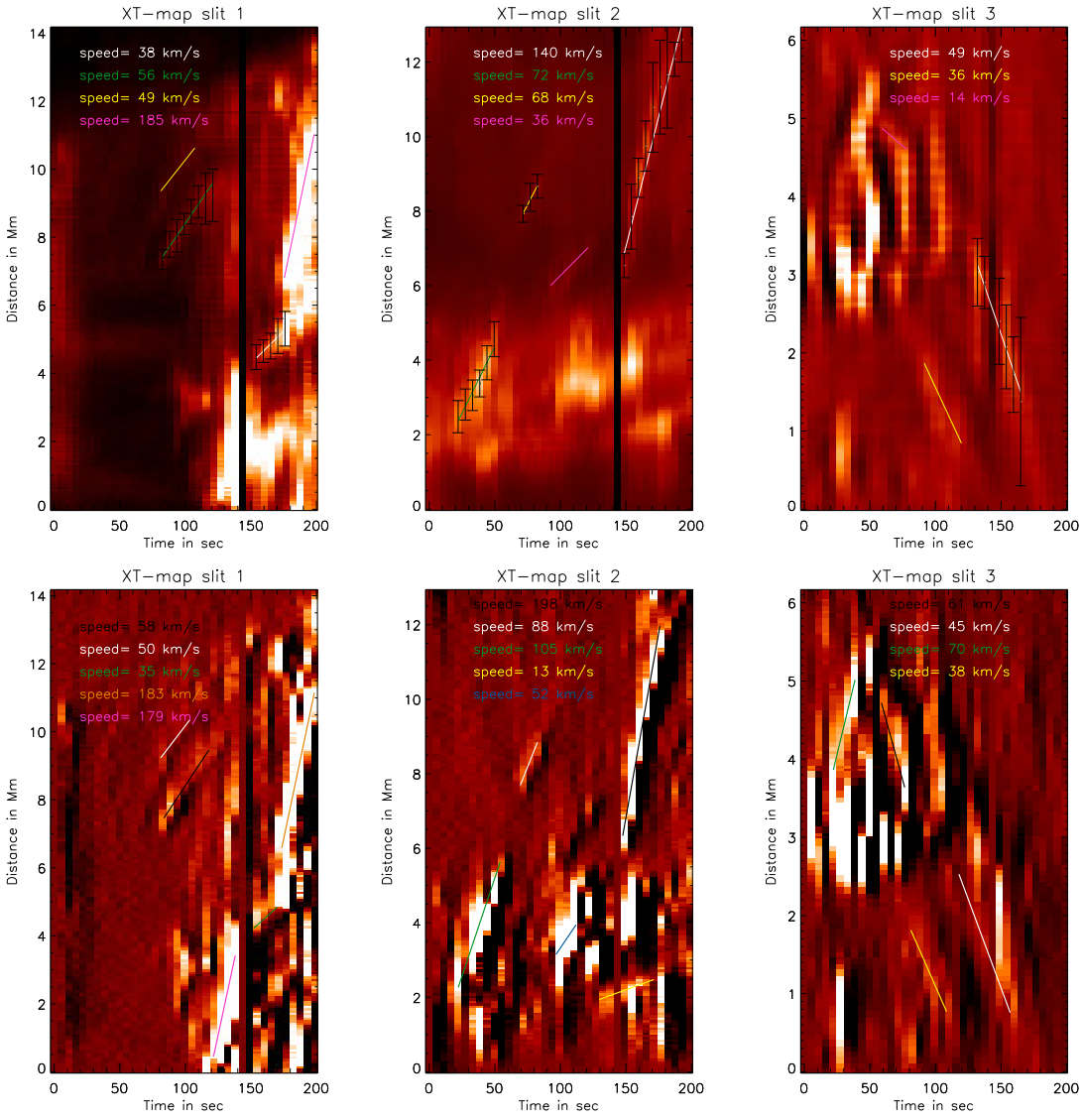

FIGURE 5.4: *Top panel*: Time - distance (x-t) maps corresponding to the three curved slices marked as 1, 2 and 3 in Fig. 5.1(e) overplotted with best fit straight lines on the observed ridges. The slopes of the fitted lines provide an estimate of the speeds are also printed. Black vertical strip represent the data gap of one frame. *Bottom panel*: Time - distance (x-t) maps of running difference images corresponding to x-t maps in top panel.

the amplitude observed is due to the displacement of structure along the slit and not due to shifts and jitter (Morton and McLaughlin 2013, 2014). Therefore, We find the evidence of short period, large velocity amplitude oscillations associated with braided magnetic structure.

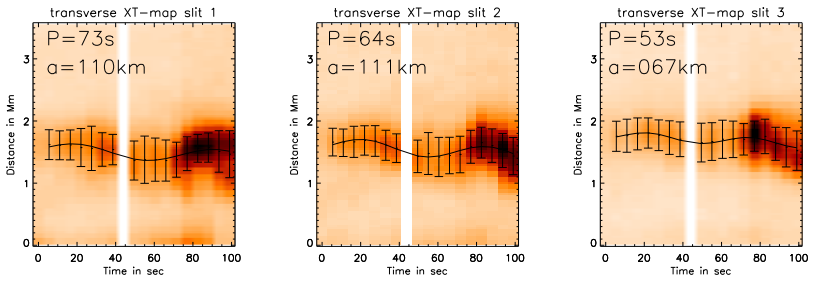

FIGURE 5.5: Inverted intensity x-t maps corresponding to the transverse slices marked as 1, 2 and 3 in Fig. 5.1(f) overplotted with best fit sine curves. P and a are time period and amplitude of oscillations. White vertical strip represent the data gap of one frame.

5.4 Conclusion

In this study we investigate the high frequency dynamics of braided magnetic region as seen from Hi-C. Our filtered images reveal finer structures in contrast to the original images. These filtered images allows us to focus on the braided region and identify the threads within them. We produce power maps for periods in the 30- 60 s interval and find that such periodicities are present in small spatial scales and can be detected with high temporal and spatial resolution only. Furthermore the power maps reveal the finer structuring within the moss region. We find that significant power is present in active moss and braided region as revealed by Hi-C. One can conjecture that high frequency power if they are due to waves are very much localized in the magnetic structures and are probably using them as wave guides for propagation. They seem to be restricted within these structures only. Testa *et al.* (2013) reported that the intensity variation in moss region is due to coronal nanoflares and estimated its timescale to be $\sim$ 15-20 s. In this study wavelet analysis reveal that shorter periodicities ($\sim$ 15-30 s) do exist but they are within the 95 % significance level for a white noise process. Therefore, we can not distinguish white noise with periodic signal variation. We find periodic intensity variation with time period of 30- 60 s above significance level which could be due to recurrent plasma outflows associated with repeated magnetic reconnection in these regions or due to magnetoacoustic waves propagating along these fine structures which can generate periodic variation in intensity. It is worthwhile to note that we can not distinguish between flows or waves without spectroscopic observations. Therefore, in this study by flow we mean apparent motion in plane of sky.

Braided magnetic region as shown in Fig. 5.1(f) is known to manifest sufficient amount of magnetic free energy to heat the corona and to explain the observed brightening (Thalmann *et al.* 2014). Tiwari *et al.* (2014) reported subflares occurring in this region by analysing intensity in AIA images. They showed that such subflares are the consequences of magnetic reconnection. Cirtain *et al.* (2013) reported outflow velocities to be 100-150 km s^{-1} in this region driven by plasma pressure along the field as the plasma is heated locally because free energy released due to magnetic field dissipation due to reconnection. We have focused our attention to a highly probable reconnection site (see Tiwari *et al.* (2014)). We find that the reconnections occurring in this region can drive plasma to a wide range of velocities from 13 km s^{-1} - 185 km s^{-1} projected in plane of sky depending on the strength of reconnection. Outflow velocities for most of them are lower than sound speed (100 km s^{-1} for 1 MK plasma) while some of them are greater than sound speed.

Morton and McLaughlin (2013, 2014) reported the period of transverse oscillations in moss region peaking around 50 s, displacement around 40 km and velocity amplitude peaking around 3 km s^{-1}. In this study we focussed on short period and large amplitude oscillation and we find that short period and large velocity amplitude oscillations are associated with braided magnetic region where reconnection happens (Thalmann *et al.* 2014). McIntosh *et al.* (2011) reported the velocity amplitude of 5±5 km s^{-1} using Monte-Carlo simulation in active region of the Sun at coronal heights. Such low frequency waves are not energetic enough to heat active corona. They have conjectured the presence of shorter period waves in active region which can not be resolved by SDO/AIA. Our analysis confirms the presence of large amplitude ($\sim$ 8–11 km s^{-1}) high frequency ($\sim$53–73 s) transverse waves in braided magnetic region. The amplitude of these oscillations are $\sim$67–110 km which is far below the spatial resolution limit of AIA. Therefore such oscillations can not be resolved by AIA. Such waves could be responsible for heating active corona. Since significant brightening and plasma outflows observed in braided magnetic region and transverse oscillation happens at same time it is not yet clear if reconnection is driving the transverse waves or if transverse waves cause magnetic field lines to reconnect. Further studies are required to confirm this. Our results confirms the necessity of high temporal and spatial resolution combining imaging with spectroscopy for future missions.

Chapter 6

Evolution and Dynamics of Different Structures during Prominence Eruption

A quiescent prominence was observed at north–west limb of the Sun using different extreme ultraviolet (EUV) channels of Atmospheric Imaging Assembly (AIA) onboard *Solar* **Dynamics** *Observatory* (SDO) and Extreme UltraViolet Imager (EUVI) onboard *Solar TErrestrial RElations Observatory* (STEREO). We report and analyse twisting/untwisting motions during and after a prominence eruption. The twisting-untwisting of two footpoints and a tornado like swirling motion near the footpoints of the prominence are studied. The prominence erupted asymmetrically. We segregate the observed rotational motions into small and large scale. Small scales manifest as the rotating funnel/tornadoes. Large scales manifest as the roll motion during the eruption. We note that the prominence threads untwist after eruption and the twist propagates upward with the speed of $\sim$83 km s^{-1}. The signatures of the swirling motions of the plasma along different circular paths in the cavity of the prominence are found. The rotational velocities of the plasma moving along different circular paths are estimated to be $\sim$ 9–40 km s^{-1}. Finally, we find the signatures of the twist built up in the prominence, being carried away

by the Coronal Mass Ejection (CME) as seen in LASCO/C2 coronagraph. We conclude that small scale rotational motion in prominence destabilize the prominence and give rise to large scale rotational motions.

6.1 Introduction

Prominences and/or filaments are ubiquitous in solar corona. They manifest as cool plasma structure embedded in the hot corona. The temperature of the prominences can range from 7500 K to 9000 K (Labrosse *et al.* 2010; Parenti 2014; Mackay *et al.* 2010). They are observed as a bright arcade structure off the limb, in chromospheric lines, *e.g.* Hα (6562.8 Å) or He II (304 Å), where as appear dark in hot coronal lines (Fe IX 171 Å, Fe XII 193 Å). On disk they appear darker compared to the background due to presence of plasma absorption processes, and are known as filaments (Parenti 2014). Polarimetric measurements reported the strength of magnetic field of quiescent prominences between 8 to 10 G for filaments (Lin *et al.* 1998), and for prominences (Paletou *et al.* 2001). High resolution observations in Hα show that prominences have finer thread like structures (see Lin *et al.* 2009; Lin 2011, and references therein). Observations of a active region prominence in Ca II 396.8 nm H line also reveal the finer structures (Okamoto *et al.* 2007).

Prominences can remain stable for a long time. Depending on different parameters like twist in the magnetic field, mass loading and ambient magnetic field they become unstable and erupt (Moore and Labonte 1980; Moore *et al.* 2001; Antiochos 1998; Antiochos *et al.* 1999). There are mainly two different models (tether cutting and magnetic breakout) that can trigger prominence eruptions. In tether cutting model, the overlying magnetic structures open up due to reconnection and lead to the eruption of the prominence (Moore and Labonte 1980; Moore *et al.* 2001). In this model a highly sheared magnetic bipole is involved. Magnetic tension is released by a reconnection at deep inside the core. In breakout model magnetic energy is released by two reconnections. The expanding central arcade

reconnects with the anti-parallel overlaying magnetic field, followed by the reconnection underneath the filament (Antiochos 1998; Antiochos *et al.* 1999). Breakout model reqiures a multipolar magnetic system and a overlaying sheared arcade . Magnetohydrodynamic (MHD) instabilities can also trigger the eruptions in some models. Decay of the magnetic field with expansion of FR causes torus instability (Kliem and Török 2006). Kink instability triggers the eruption when twist of the FR increases above a critical value (Török and Kliem 2003; Fan and Gibson 2003; Török and Kliem 2005; Fan and Gibson 2007). Observational studies of prominence eruptions support different models, while some events show evidences of more than one model.

Swirling motions have been observed in the solar atmosphere. Chromospheric swirls or small scales magnetic tornadoes have been observed by Wedemeyer-Böhm and Rouppe van der Voort (2009) and Wedemeyer-Böhm *et al.* (2012). The authors suggested that these swirls provide a channel to transfer energy from lower to upper atmosphere. Several giant tornado like structures have been reported in solar atmosphere. Such structures have been associated with the vertical structure and barbs of the prominences/filaments (Li *et al.* 2012; Su *et al.* 2012; Wedemeyer *et al.* 2013). There are few reports on the estimation of the rotational speed of the plasma in the giant tornadoes (Li *et al.* 2012). Mghebrishvili *et al.* (2015) studied dynamics of a solar tornado using 304 , 171, 193, and 131 Å channels of *SDO/AIA*. They estimated the rotational speed of threads around a tornado axis as $\sim$ 6 km/s. A study of a tornado like prominence from *Hinode/EIS* and *SDO/AIA* indicates rotation of plasma around the tornado axis (Su *et al.* 2014). A new model of vortex-filament is suggested by the authors according to which, the vortex motion twist the magnetic field. Plasma may be transported from the photosphere through this twisted magnetic field. This gives rise to highly twisted flux rope (FR) structure, which eventually becomes unstable after a large twist built up (Wedemeyer *et al.* 2013; Su *et al.* 2014). Yan *et al.* (2014) studied the eruption of an active region filament. The twist build up was found to be enough for kink instability. Authors also confirmed that the magnetic helicity was transferred from the photosphere to the corona. In addition to small scale twisting motions discussed above, large scale twists (roll motion) are also reported during a prominence eruption (see Panasenco *et al.* 2013).

Prominence eruptions are usually associated with Coronal Mass Ejections (CMEs), which are huge eruptions of plasma and magnetic field into heliosphere and are the main cause of geomagnetic disturbances (see Parenti 2014, and references there in). Erupting prominences form the bright core of a typical three part CME, along with a bright frontal lobe and a dark cavity (Chen 2011; Illing and Hundhausen 1985; House *et al.* 1981).

We study small and large scale twisting/winding/unwinding motions before, during and after a prominence eruption. In sections 6.2 and 6.3, we describe the observation of twisting/untwisting motions of the prominence in different EUV channels, methods of data analysis and results. In section 6.4, we describe the association of the CME with the erupting prominence, which is followed by the discussions in section 6.5 and the conclusions in section 6.6.

6.2 Data and Analysis

A prominence eruption is observed at the north-west limb of the Sun on 2012 November 26, by *Atmospheric Imaging Assembly* (AIA) (Lemen *et al.* 2012) on board *Solar Dynamics Observatory* (SDO) (see, Fig. 6.1a). We use Extreme Ultra Violet (EUV) images, taken by AIA, in three different channels centred at 304 Å, 171 Å, and 193 Å for this study. Images of size 1100 pixels by 1200 pixels, centered at (777″, 751″), of 10 hr duration, starting from 11:00 UT on 2012 November 26 constitute the data set. The time cadence and the spatial resolution of the data are 12 s and 0.6″ respectively. The standard *aia_prep.pro* routine is used to process the initial level 1.0 data for correction of roll angles and to bring data from different channels to a common centre and common plate scale. We use two subfield regions, each of 1 hr duration, for studying twisting and swirling motion. A subfield, ROI B in Fig. 6.1, centered at (897″, 751″) is chosen to study the evolution of the southern footpoint in Section 6.3.6. ROI C in Fig. 6.1, centered at (888″, 487″), is chosen for the study of swirling motions after the prominence ceruption in Section 6.3.7. All data sets are co-aligned using intensity cross-correlation. This prominence eruption was associated with a Coronal Mass Ejection (CME) at a central principal angle,

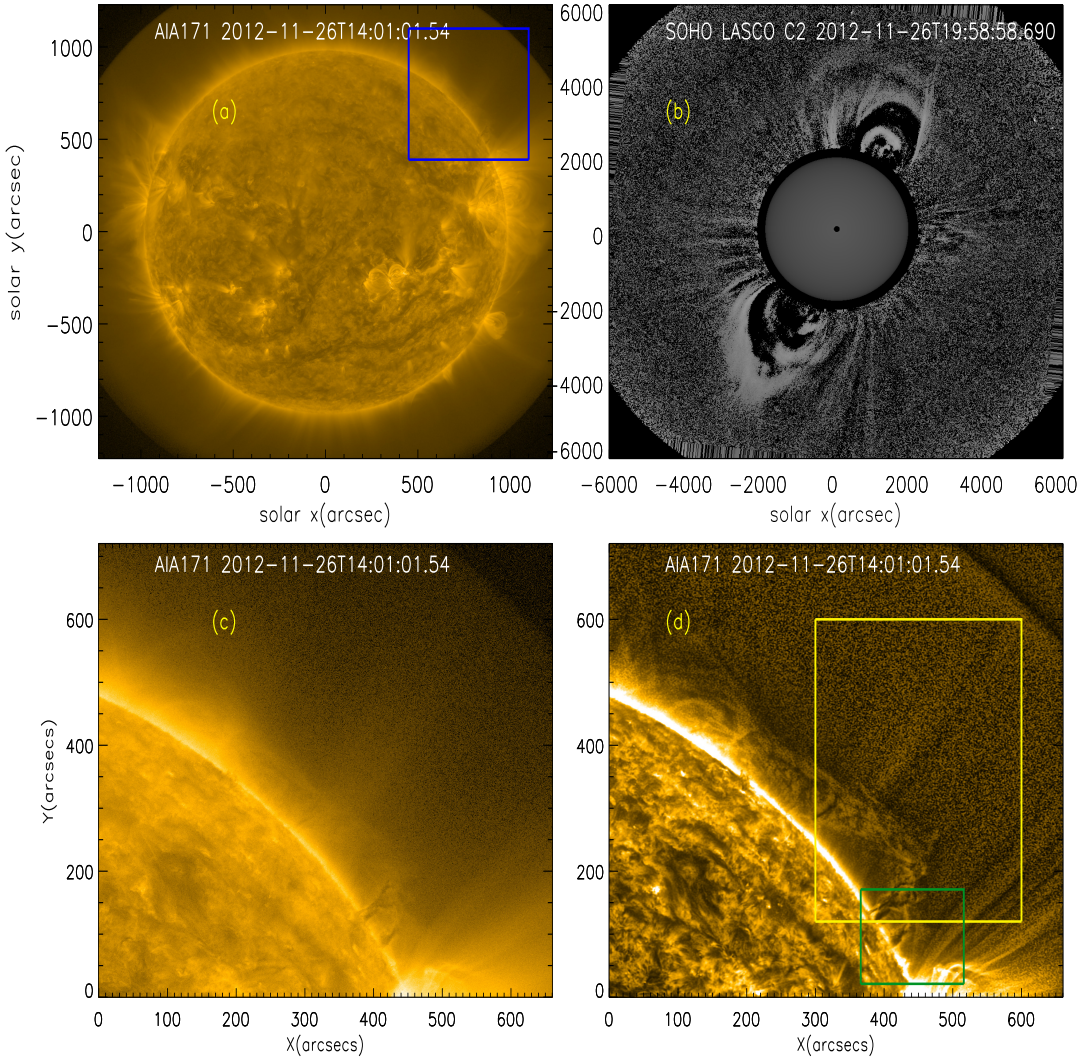

FIGURE 6.1: (a) AIA 171 Å full disk image, the blue rectangle represents the Region of Interest A (ROI A). (b) The CME, which is associated with the prominence. (c) AIA 171 Å image of the ROI A . (d) The ROI after applying multi-gaussian normalized filter. Twisting and swirling are observed in the regions marked by yellow and green rectangles respectively (ROI B and ROI C).

340° (see Fig. 6.1b), as quoted in the SOHO/LASCO CME catalogue (Yashiro *et al.* 2004). The linear speed of the CME was 299 km s^{-1}. CME first appeared in the LASCO/C2 field of view at 17:48 UT. The core of the CME was rotating anti-clockwise. Such CMEs are called 'cartwheel' CMEs and have been reported in the earlier studies (Kliem *et al.* 2012). We discuss prominence-CME association in Section 6.4.

We further process the AIA images to enhance faint structures at different spatial scales. First, we convolve each image with a low pass filter (Gaussian kernel) and subtract the convolved image with the normal intensity image to retain the features that have high spatial frequency. We iterate this process three times to estimate the uncorrelated noise. Then, we subtract uncorrelated noise from the original image. To enhance the finer structure, we use a normalized multi–Gaussian filter to the filtered image (see Morgan and Druckmüller 2014; Pant *et al.* 2015). We choose width of gaussian filter to be 21, 41, and 61 pixels. We add Gaussian filtered images of different spatial scale to the original image. The prominence threads and fine structures in the coronal loops are much clearly visible in the multi–Gaussian filtered images (see Fig. 6.1d). Hereafter, all analysis is done using multi-gaussian filtered images.

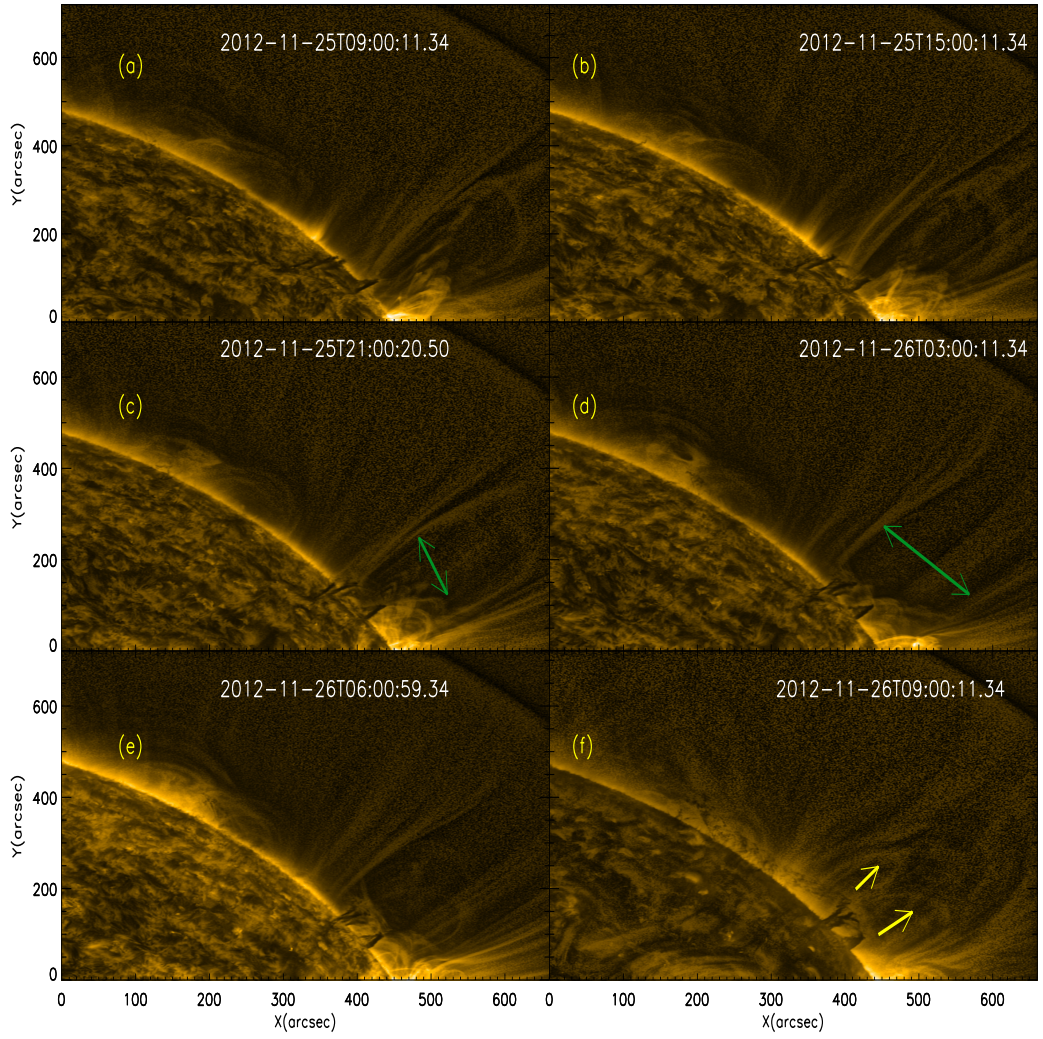

FIGURE 6.2: Overlaying loop system and the prominence as seen in AIA 171 Å channel. (a) Dark funnel like structures present near the limb. (b), (c) and (d) Snapshots of different stages of formation of the background open cavity (marked with green arrows). (e) and (f) Emergence of closed loop in the cavity (marked by two arrows in yellow).

6.3 Observations and Results

The prominence appears as a dark elongated structure near the active region AR 11616 at an on disk position, as seen in AIA 171 Å channel on 2012 November 23. Without any apparent changes, this dark elongated structure moves towards the limb. We follow the prominence from 09:00 UT, 2012 November 25 to 22:00 UT, 2012 November 26. Till 09:00 UT, 2012 November 26 we observe the evolution of the background loops in every 3 hrs. As the prominence starts lifting (09:00 UT 2012 November 26 on wards), we study the various stages of the prominence eruption and after eruption events using image sequence of 12 s cadence.

6.3.1 Evolution of the background loops as seen in AIA 171 Å (2012 November 25; 09:00 UT– 2012 November 26; 09:00 UT):

- *Vertical funnels:* At around 09:00 UT 2012 November 25, near the limb we see the prominence barb consisting of three small dark vertical funnel like structures (Fig. 6.2a). There are overlaying loops (both closed and open) in the background.

- *Broadening of cavity:* These open loops move away from each other with time. As the distance between these loops increases (marked with green arrows in Fig. 6.2 b, c and d), at early hours of 2012 November 26 we notice an open cavity above the prominence barbs.

- *Expansion of closed loops and lifting up of the prominence:* As the filament barbs move towards the limb, around 09:00 UT 2012 November 26, closed loops appear in the open cavity (Fig. 6.2f). Vertical funnels are now attached to elongated spine, which are spreaded in northern direction. The spine consists of many intertwined and spiralled finer dark threads.

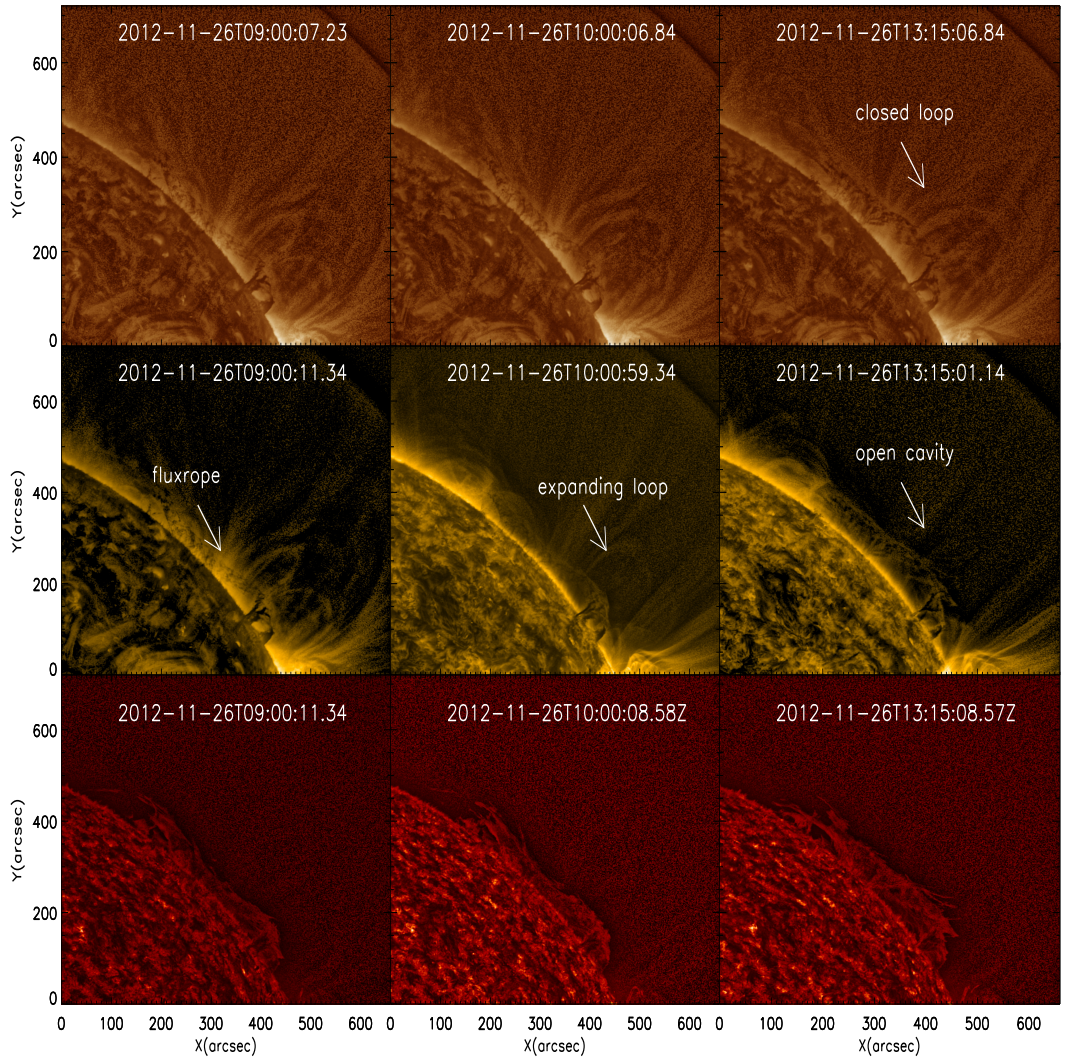

FIGURE 6.3: (Upper panels) Prominence lift off and evolution of background loops as seen by AIA 193 Å channel. (middle panels) Same event by AIA 171 Å channel and (lower panels) by AIA 304 Å channel.

6.3.2 Prominence lift off and the Eruption (2012 November 26; 09:00 UT – 16:00 UT)

After 13:00 UT 2012 November 26, disappearance of the expanding closed loops opens the overlaying cavity (middle right panel of Fig. 6.3). The prominence continue to rise. As the background loops evolve, the prominence twists and rises, finally it erupts around 16:00 UT 2012 November 26. We observe this event in

different channels of AIA.

- *Evolution in AIA 304 Å :* The prominence is visible in AIA 304 Å channel as a bright structure (lower panels of Fig. 6.3). Around 11:00 UT the prominence starts rising slowly, followed by a fast rise phase after 15:00 UT. During the initial phase the height of the footpoints and the spine increases without any rotating or twisting motion, but after 15:30 UT, during the fast rise, the entire southern footpoint rotates around a common axis. While the northern footpoint of the prominece rises without any apparent twist. The prominence erupts and the prominence spine brakes asymmetrically near the southern footpoint aound 16:00 UT. Soon after the eruption, prominece material starts falling along twisted paths.

- *Evolution in AIA 171 Å :* The prominence spine appears as a helical structure consists of many dark winding threads, in hotter AIA 171 Å channel (middle panels of Fig. 6.3). The dark funnels at the southern footpoint twist, devoid of any twist the spine rises slowly. As the background cavity opens (right middle panel of Fig. 6.3), the prominence lifts up with a faster pace after 15:00 UT and by this time the twist of the funnels increases and twist extends to the spine also. As the prominence erupts after 16:00 UT, we observe untwisiting and swirling motion.

- *Evolution in AIA 193 Å :* The evolution in AIA 193 is same as observed AIA 171 apart from the transformation of the overlaying loops (upper panels of Fig. 6.3). These loops do not evolve during the eruption of the prominence (right upper panel of Fig. 6.3).

6.3.3 Small scale twist of the prominence footpoint (2012 November 26; 11:00 UT – 15:00 UT)

The funnel structures of the barb of the prominence twist slowly as the prominence rises. In the initial phase of the prominence rise this small scale twist builds up.

The twisting of individual dark funnels at the southern footpoint during the initial phase of prominence rise, is best seen in AIA 171 Å.

- Three vertical dark funnels are visible around 11:00 UT at the southern footpoint (Fig. 6.4a). During the next one hour time there is steady increase in height of the foot point funnels. Rotation of the funnels around a certain axis is not clear, neither the rotation of the funnels themselves is.
- Around 12:00 UT one of the funnel (f1 in Fig. 6.4b) divides into sub branches. The height of the funnels along with the distance between the sub branches increased with time.
- Around 13:15 UT twist is prominent along f1 (Fig. 6.4c). This time corresponds to the start of the slow rise phase of the prominence. As the time progresses, the twist increase in the funnels. Around 14:38 UT, f1 got entangled with the adjacent funnel, f2 (zoomed view Fig. 6.4d). After this the fast rise phase of the prominence starts (15:00 UT).
- With time twist increases and extent of the twist also increases along the spine. In a way twists propagate from the footpoint funnels to the spine and simultaneously expand the prominence structure.
- It is worth noting that the southern footpoint, where the tornado like structures and twisting motions are seen, is located near the active region while the northern footpoint is anchored at quiet region of the Sun, with no apparent twist.

6.3.4 Roll motion of the spine (2012 November 26; 14:30 UT – 17:00 UT)

In this section, we present the observation of the large scale twisting motion, *i.e,* roll motion, during the prominence eruption.

- As the prominence rises, after 13:00 UT the footpoints (especially the southern footpoint) start rotating as a whole, twisting the prominence spine gradually. The roll motion is visible in AIA 304, 171 and 193 Å channels.

- The anticlockwise motions of the footpoints are apparent from the difference images in Fig. 6.5. In the upper panels of Fig. 6.5, we follow a loop in the foreground (marked by dotted line) of the southern footpoint before eruption. The rotation of this loop from north to south indicates that the southern footpoint rotates anticlockwise. The bright loops at the northern footpoint also move from north to south as shown in the snapshots of the middle panels. Since these loops are also in the foreground, we conclude that northern footpoint of the prominece is also twisting anticlockwise.

- After the eruption a swirling motion is noted near the southern footpoint (ROI C). We follow two plasma blobs, marked by violet and blue arrows (lower panels of Fig. 6.5), as they move along different helical paths. The blobs, show a clear anticlockwise rotation of plasma in the plane of the sky. It indicates that similar twist might have been built before the eruption.

6.3.5 Asymmetric Eruption (2012 November 26; around 17:00 UT)

The anticlockwise twist of both the footpoints twist the spine and around 17:00 UT the spine breaks asymmetrically near the southern footpoint. We may recall that the cavity opens near the southern footpoint (Figures 6.2, 6.3) and dark funnels of cool plasma are present at the southern footpoint only. The opening of the background field lines and uneven distribution of prominence material might have caused the asymmetric eruption.

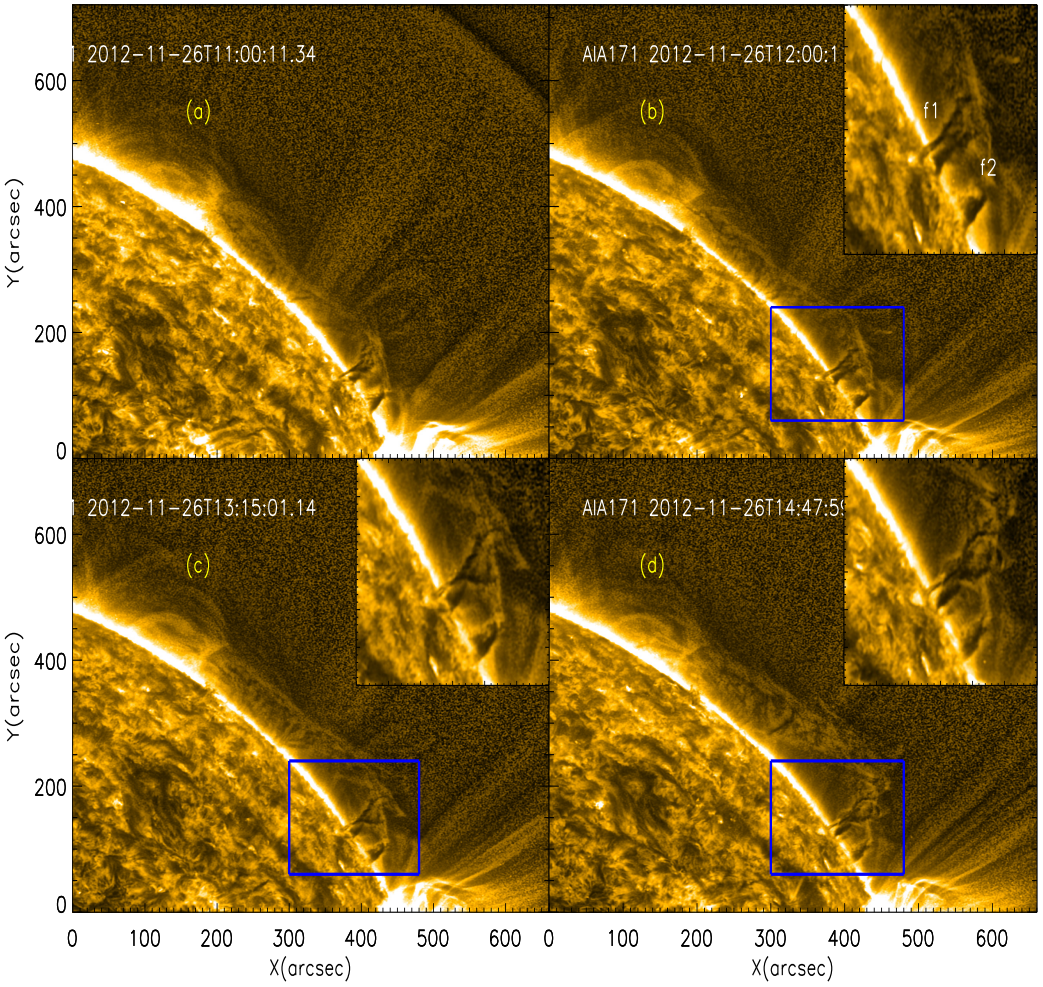

FIGURE 6.4: Rising phase of the prominence along with the twist in the southern footpoint as seen in AIA 171 Å channel. The expansion of the background closed loops are also seen. The vertical dark funnels near the southern footpoint twist during the rising phase. The yellow rectangles in panels (b), (c) and (d) indicate the zoomed area shown in the corner of the corresponding panels. The dark funnels twist, branch and entangle, as they continue to rise.

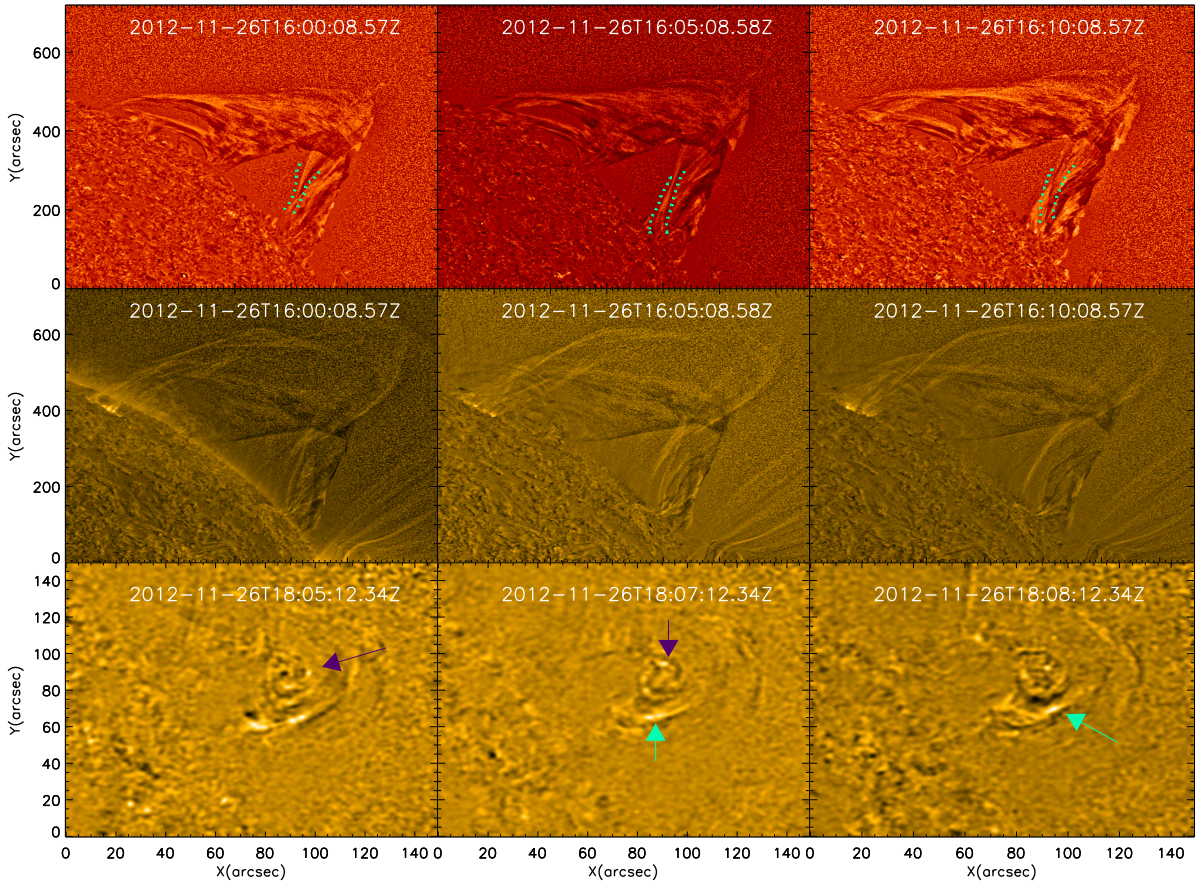

FIGURE 6.5: (upper panels) Difference images before eruption in AIA 304 Å channel showing anticlockwise rotation.Dashed lines show the positions of a foreground loop at southern footpoint in consecutive snapshots (middle panels) Anticlockwise rotation of the northern footpoint before eruption as seen in AIA 171 Å differnce images. (lower panels) Swirling motion of the southern footpoint after eruption in AIA 171 Å channel. Tracked features are marked with arrows in the consecutive snapshots.

6.3.6 Untwisting motions after the Eruption: after 17:00 UT

- After the eruption, both footpoints rotate around certain axes in anticlockwise direction. The prominence plasma fall along twisted magnetic fields near the footpoints. A twist of approximately π is seen at the southern footpoint between 16:20 UT and 16:50 UT. While the plasma follows a path twisted by approximately $3\pi/4$ at the northern footpoint from 16:30 UT to

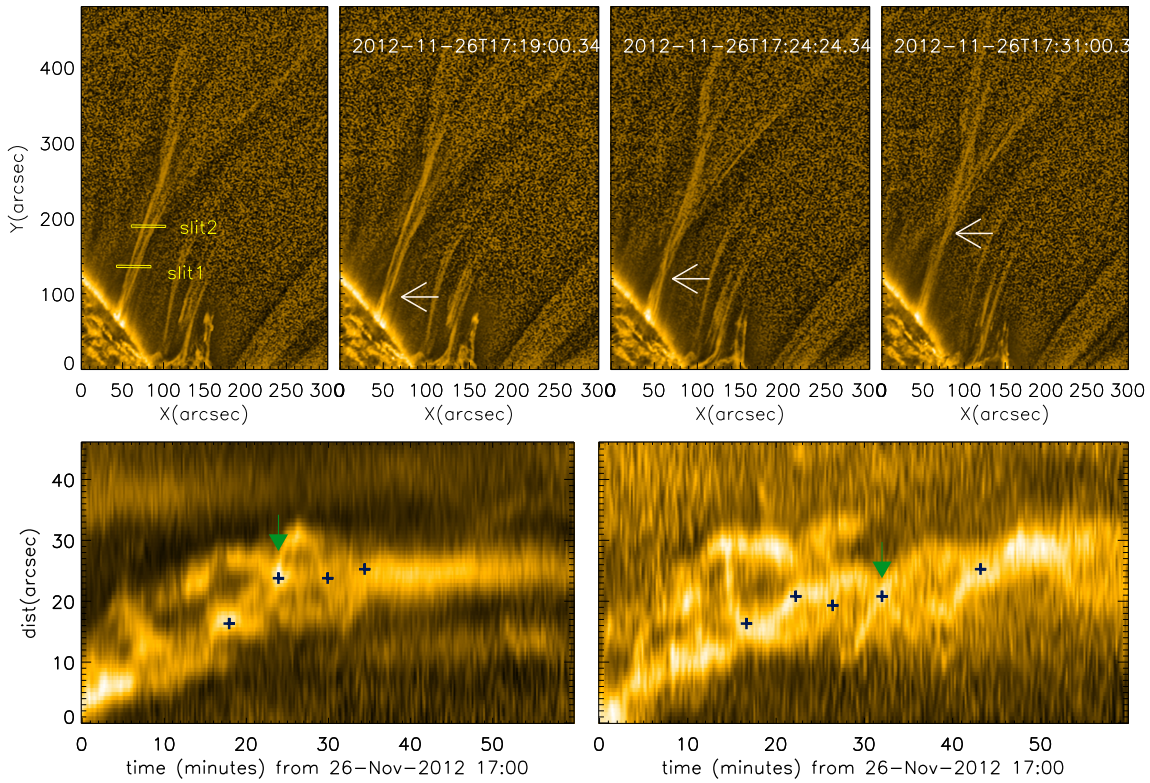

FIGURE 6.6: (upper left panel) Zoomed view of southern footpoint of the prominence (ROI B in Figure6.1d). (upper right panels) Snapshots at three different time show the shift of the twist of finer threads. (lower left panel) Space-time map corresponding to the Slit1. (lower right panel) That of Slit2.

17:30 UT

- Estimation of degree of twist before the eruption is difficult, since the magnetic twist of the prominence might have built up over a long time. Therefore, to estimate the magnetic twist that has built up in the prominence, we study the untwisting motion of the finer loop like structures near the southern footpoint after the eruption (see region enclosed in yellow box in Fig. 6.1d). This way we can assess a lower limit of the magnetic twist that was built up before the eruption of the prominence. The untwisting motion is best observed in AIA 171 Å channel from 17:10 UT to 17:50 UT (Fig. 6.6).

- After remaining entangled for a while, the threads are separated and then again get entangled to some other thread of the prominence. We also note

that the threads are twisted around 17:20 UT near the limb. The twist moves away from the limb with time. The snap shots at 17:19 UT, 17:24 UT and 17:31 UT show the propagation of twist along the threads (three upper right panels of Fig. 6.6). The positions of the twist (i.e, position at which two threads cross over) are marked with the white arrows. The location of the twist is at a height of 76 Mm at 17:19 UT, it propagates to a height of 98 Mm at 17:24 UT and to 136 Mm at 17:31 UT with an average speed of 83 km s^{-1}. This measured speed is the projected speed in the plane of the sky and could be an underestimate of the true speed. Recently Okamoto *et al.* (2016) have studied helical motion of horizontal prominence threads. From the phase delay of prominent thread structure, they have estimated the propagation speed of twist along a helical structure. The propagation speed is found to vary from 270 km s^{-1} to 90 km s^{-1}, which is higher than the propagation speed of twist along the finer threads estimated in our present study.

- We create the space-time map by placing two artificial box slits of dimension 77×5 pixels at the locations of the entangled threads (Slit1 and Slit2 in the left upper panels of Fig. 6.6). The intensity values along each pixel in 'y' direction are obtained by summing all the pixel values in the x direction. Stacking of these values for each time frame creates desired the space-time plot. The untwisting and entanglement of different threads of the prominence barb appear as the crossings of the bright ridges in the space time map, marked with + sign. The twist is at a height of 98 Mm, which is at the postion of Slit1 at 17:24 UT. A crossing of bright ridges is visible at the same time in the space-time map of Slit1, the twist and the crossing both are marked with arrows in the corresponding panels. Another similar bright crossing is observed in the space-time map of Slit2 at 17:31 UT, when the twist has propagated to the height 136 Mm (marked with arrows in lower and upper right panels respectivly). We conclude that other crossings in the space-time map are also due to twist and not an apparent motions of different threads.

- We estimate the angle of twist from the space-time maps. There are $3-4$ prominent crossings of bright ridges along Slit1 and $4-5$ such crossings are present in the space-time map of Slit2. Hood and Priest (1981) showed by

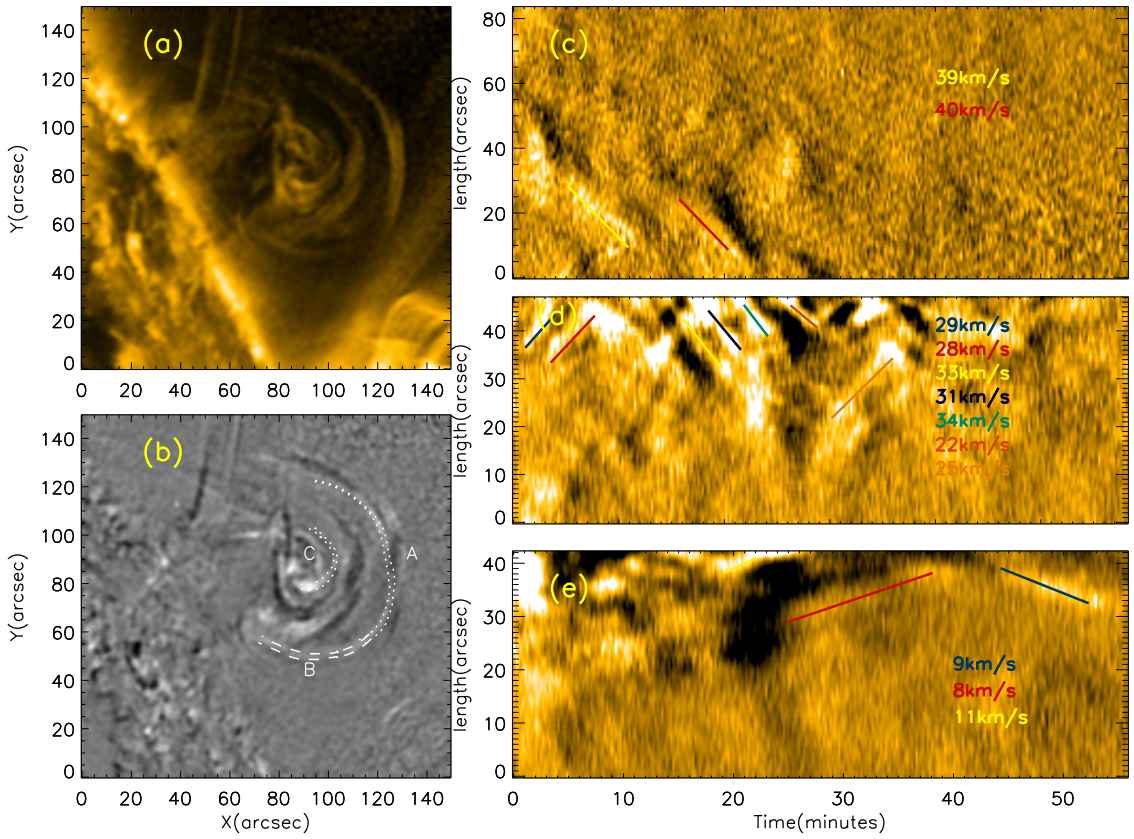

FIGURE 6.7: (a) Tornado like swirl near the right footpoint as seen in AIA 171 Å channel (ROI C in Figure6.1d). (b) Running difference image of the same region. Curved slits A, B, and C are used to study the plasma movement during the swirl. (c), (d), and (e) Running difference images of space-time maps from curved slit A, B and C respectively. Speeds of plasma movement through diffrent channels are calculated from the slope of the bright ridges.

numerical method that a twist $> 2.49\pi$ in the loops can cause kink instability, which is one of the triggering mechanism of prominence eruption. Later Török and Kliem (2003) estimated the critical twist angle required for kink instability as $\phi > 2.75\pi$. Since each crossing represents the twist angle of π, the observed lower limit of twist angle (ϕ) is $3\pi - 4\pi$ in the present study, which is sufficient for onset of the kink instability and to erupt the prominence.

6.3.7 Swirling motion after the Eruption (2012 November 26; after 17:30 UT)

- A swirling motion starts at the southern footpoint (ROI C in Figure6.1d) after 17:30 UT. The movement is best observed in AIA 171 Å channel. The prominence material was moving along different circular paths (Fig. 6.7(a)).

- We observe clockwise, as well as anti-clockwise movement of the plasma along different circular channels. The plasma movements through varoius channels are not synchronized. We choose two curved slits, namely A and B along outer channels, and another curved slit, C, closer to the axis of swirling structure as shown in Fig. 6.7(b).

- A 4 minute running difference images of the space-time maps along these channels exhibit bright and dark ridges (Figures 6.7c,d and e). Bright ridges with negative (positive) slope indicate plasma movement in clockwise (anti-clockwise) direction. Plasma moves in clockwise direction is observed along slit A. Whereas clockwise and anti-clockwise movements are ther along slits B and C. The plasma speeds are estimated from the slope of the bright ridges of the space-time maps. Plasma swirls with higher speeds $35-60$ km/s along A. The speeds are found to be $22-29$ km/s along 'B'. Speeds along the inner curved slit, 'C' are around $11-12$ km/s., which are much lower compared to that along the outer curved slits. We observe that speeds do not vary for two different directions of motion. It seems that the plasma follows the helical or twisted field lines which looks like swirling motion. Later on the magnetic field lines relaxed and spiral structure was no longer present.

- Recently, Xia *et al.* (2014) has simulated the condensation process in a solar prominence, where they have shown that the helical field lines in the cavity of the prominence (see Fig. 5 of Xia *et al.* 2014). After eruption the plasma blobs may follow these helical field lines and cause swirling motions as observed in this study. The helical field lines might be the consequence of the twist that was built up in the southern footpoint of the prominence.

6.4 Prominence eruption and onset of CME

We found out that a CME was associated with this prominence eruption. Even though it seems that most of the prominence material fell back, a part of it was carried away by the CME. We observe that the twist which was built up in the southern footpoint of the prominence, manifests as counterclockwise rotation of the prominence material of the CME. Since the CME was propagating outward and the LASCO/C2 has a cadence of 12 minutes, thus the features rotated and changed rapidly. This makes the quantitative measurement of rotation a difficult task. Nevertheless, it points towards the fact that a part of twist was carried away by the CME. We try to estimate the degree of rotation of the features in the CME by tracking some of the prominent features. In order to estimate the degree of rotation, first we choose a feature which is found to be rotating clearly in the coronagraph images. Then the angular position of the feature is determined. To estimate the angular position of the feature, a circle is chosen such that it passes through the feature. Angular position is the angle that the feature makes with the horizontal direction. In subsequent images as the CME moved outward, we estimate the angular position of the feature at every instant. Therefore, as the feature rotates, the angular position changes. We track the feature until it either disappears from the coronagraph images or becomes too faint to detect. We apply this procedure to two features in coronagraph images (see Figures 6.8 and 6.9) and find that the they rotate by 150° and 64°, respectively. First feature appeared at 19:00 UT and disappeared after 20:24 UT. Second feature appeared at 20:48 UT. The second feature appeared when the first feature disappeared. Therefore, the total degree of rotation is the sum of the degree of rotation of both features, *i.e,* 214° assuming that these two features are the part of same prominence. This is still an underestimate of the total twist because we couldn't see clear features at several instances.

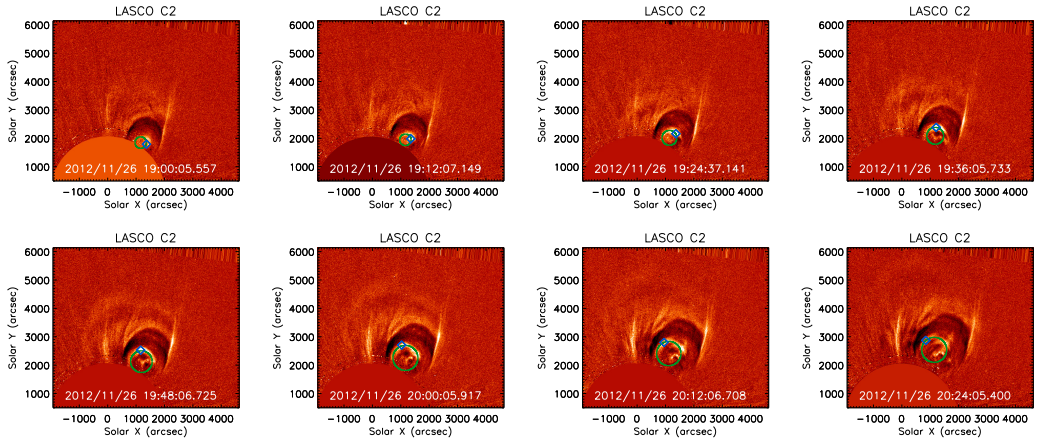

FIGURE 6.8: LASCO/C2 running difference image. Diamond in blue represents the feature that is rotating anticlockwise. Since the feature is extended, diamond symbol represents the location of maximum brightness. Circle in green passes through the feature of interest and is used to estimate the angular position of the feature. The degree of rotation is 150°.

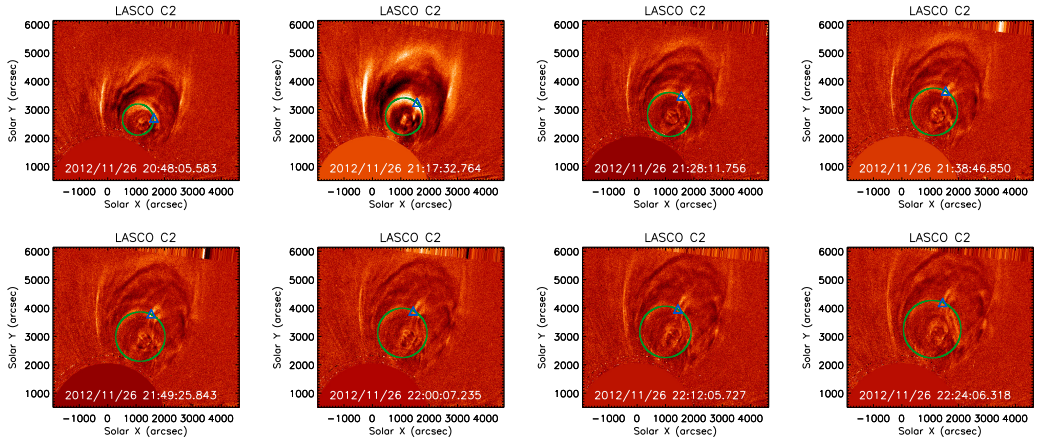

FIGURE 6.9: Same as Fig. 6.8 except for a different feature marked with a blue triangle. Degree of rotation is 64°.

6.5 Discussion

We report twisting/untwisting motions during a prominence eruption. The southern footpoint of the prominence was lying in close proximity to the active region. Photospheric vortex flows are more frequent near the active region as compared to quiet Sun thus it may explain why the southern footpoints has larger twist as compared to the northern footpoint which was rooted at the quiet region of the Sun at higher latitude. Since the photospheric vortex flows may contribute to the

formation of such funnel like structures/tornadoes, the funnels like structures are present in the southern footpoint. Below we discuss few important aspects of the twisting/untwisting motions as observed in Sections 6.2 and 6.4

- *Evolution of overlaying loops*: We find that overlaying loop seen in AIA 171 Å disappeared prior to the prominence lift-off and subsequent eruption of the prominence. Furthermore, to our surprise, neither the signature of Fluxropes nor the evolution of background loops (reconnections) are seen in hotter channels like AIA 94 and 335 Å.

- *Small scale twisting motions*: We call, rotation of the funnel like structures, barbs, as small scale twisting motions. Such rotating structures are termed as giant tornadoes by Wedemeyer *et al.* (2013). The rotation of the tornado could transfer cool material and magnetic twist to upper layers. The magnetic twist increases the coronal magnetic field stress, thus making the prominence unstable. In this study, we find that the barbs were present since 23^{rd} November, 2012. It is therefore, difficult to estimate the twist that had developed in the period of three days. Therefore in order to estimate the twist developed in the southern footpoint of prominence, we estimated the untwisting motion after the prominence eruption. This may give a lower limit on the degree of twist that has built up before the eruption of the prominence. The transferred twist would make the prominence unstable. It is worth noting that unlike Su *et al.* (2012), Panasenco *et al.* (2014) have explained the twist of a dark funnel like structure as the projection effect of oscillatory motion. Authors also suggested that the apparent vortex motion might be a illusion either due to oscillations of individual threads of prominence, or due to counter streaming of plasma.

- *Large scale twisting motions*: Panasenco *et al.* (2013) reported that the twist in the spine propagates down, resulting opposite twist in both the footpoints. However, we find that twist in both footpoints of the prominence was anti-clockwise. Similar sense of twist in footpoints resulted in opposite twist in the prominence spine. We describe this scenario with a cartoon shown in Fig. 6.10.

- *Asymmetric eruption of the prominence*: We note that the prominence erupted asymmetrically near the southern footpoint. Several factors may contribute to the asymmetric eruption. First, we find the signatures of expanding cavity above the prominence in AIA 171 and 193 Å. From Figures 6.2, and 6.3, we note that the magnetic field configuration was different over two footpoints of the prominence. The cavity was located near the southern footpoint and we notice that the prominence started rising at the location of the open cavity. We have not observed any signature of possible reconnection during this event. So the reason behind the change in the magnetic topology is not clear to us. Second, we think that the prominence material was densely distributed at the southern footpoint due to the presence of dark funnel like structures. Combining these two facts, we conjecture that the twist happening in the dark funnel propagated to the filament spine which when exceed beyond certain degree, made the prominence unstable and the prominence started lifting. The open cavity located near the southern footpoint facilitated the easy lift-off of the prominence near the southern footpoint.

- *Swirling motion after eruption*: We find the swirling motion of the plasma along several circular paths after the eruption. It seems that the swirling motion was caused by the falling material along the helical field lines that were located around the dark funnels/tornadoes (Xia *et al.* 2014). After eruption the plasma blobs may follow these helical field lines and cause swirling motions as observed in this study. Untwisting motion might also exist in these helical field lines. In the end, these helical field lines disappeared or the shape may have completely changed, which can explain the disappearance of the dark funnels/tornadoes and spiral structure.

- *Injection of twist to the CME*: We find that a part of the twist is also carried away by the CME associated with the eruption. It should be noted that the degree of rotation will not be affected by the projection in the plane of sky. We find that degree of rotation is 214°. A similar event, nicknamed as 'cartwheel CME' was observed by Thompson *et al.* (2012). A rotation of 115° was estimated at 2.5 solar radii which is much less as compared to the degree of rotation reported in this study. Patsourakos and Vourlidas (2011) observed the same event, but to a height of 15 solar radii using COR2.

6.6 Conclusion

In summary, we observe twisting, untwisting and swirling motions before and after a prominence eruption. The evolution and dynamics, we can divide them in two phases. First, the small scale twist of dark funnels/tornadoes near the southern footpoint before the eruption of the prominence. Secondly, the large scale twist in the footpoints of the prominence during eruption (roll motion). The small scale twist might be a signature of twist injection from the photosphere to higher atmosphere. We also find untwisting motions of finer threads of the prominence after eruption. We analyse the degree of twist in the untwisting motions after the prominence eruption and find the lower limit of twist angle to be 3π at the location of Slit1 and 4π at the location of Slit2, which is large enough to onset kink instability in the prominence. After eruption we find several unwinding/untwisting motions in the threads of the prominence. We find the signatures of the propagation of twist through the threads of the prominence with a speed of 83 km s^{-1}.

We find that the prominence erupts shortly after the spine of the prominence broke, the northern footpoint was rotated by $3\pi/4$ and southern footpoint by π. Later, we note the swirling motions near the southern footpoint. Helical field lines could be the result of the twist which was built up in the prominence threads before eruption. Lastly, we also find the signature of a 'cartwheel' CME that carried a part of the twist associated with the prominence eruption. Thus we conclude from this study that the small scale rotational motions destabilise the prominence and gave rise to large scale roll motions and rotating features inside a CME.

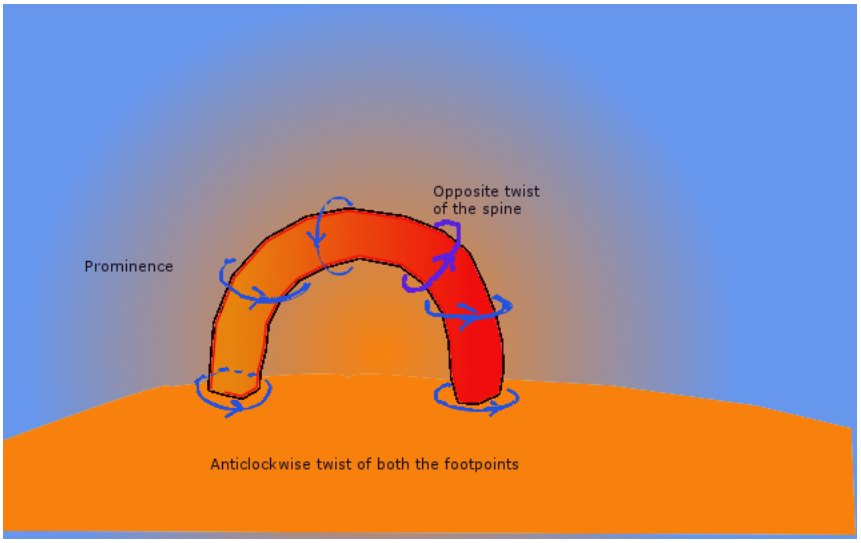

FIGURE 6.10: A cartoon showing the twist at both footpoints of the prominence in the same direction. When the twist propagates upward, it twists two sides of the spine of the prominence in opposite directions which cause prominence spine to break.

Chapter 7

Concluding Remarks

In this thesis we have studied few coronal phenomena with different spatial and time scales and studied their roles in coronal dynamics. Wave phenomenon as observed in different magnetic structures contribute to the heating of the corona and some of the small scale dynamics helps in the process of reconnection which further contributes to the heating. In two chapters we have focussed on spatial scales of several Megameters and time variations of minutes within open magnetic structures. In one of the study we have focused on very short time variations within spatial scales of 100 km or shorter and time variations of several seconds. Finally we have also studied the evolution of a prominence and associated large scale eruption like CME. These evolutions take place within hours.

We have used simultaneous observations of imaging and spectroscopic instruments during the Joint Observational Programme, JOP 165 in an attempt to understand the nature of the propagating disturbances (PDs). We have detected the PDs near the footpoint of an active region coronal loop from imaging data. The periodicity and propagation speed of the PDs, as obtained from the imaging data, were found to be 5.4 min and 39 km s^{-1}, and identified it as slow magnetoacoustic wave. Then we have analyzed the intensity, Doppler velocity and line width oscillations in Si XII 520.6 Å line at four positions along the same active region loop. The similar periodicities in all three spectral parameters confirm the presence of

magnetoacoustic wave in the upper part of the loop. But the clear oscillation in the line width near the footpoint of the coronal loop suggests that there might be quasi-periodic up flows near the footpoint, while in the upper part of loop, waves are dominant. By using emission lines of different layers we have also shown that these waves propagate from the lower atmosphere to the corona. We have used co-temporal and co-spatial imaging and spectroscopic data for the analysis. In this study we have studied different line parameters, namely intensity, velocity and widths and their correlations but have not studied the line asymmetries. One should look at the variations of the line asymmetries and its correlations with other line parameters at different regions of the loop, namely close to the source regions and away from it. Based on the observed properties, one may have a scenario where waves and flows co-exit. These study can be further continued with the help of imaging and spectroscopic instruments with higher spatial and temporal resolution. We should point out that it is very difficult to distinguish these two effects from each other from the intensity images as well as from the spectroscopic observations as presented here. One should generate synthetic spectra to justify one scenario over the other. De Moortel *et al.* (2015) made an attempt to identify waves and flows from observations using a synthetic data set. They have pointed out that with the available imaging and spectroscopic instruments, it is not possible to differentiate between flows and waves. One should also look at the effects of line of sight. Efforts should be made to combine theoretical modelling with observations which will help us to decouple these two phenomena from each.

In the context of wave propagation along polar plumes, open magnetic field structures we have studied the wave damping. The frequency dependence of slow wave mode have been studied and found out that the thermal conduction may not be the main source for damping. Using the highest possible resolution images as taken from the AIA on SDO, statistically we have demonstrated that the wave damping behaviour seems to be acting differently in the polar region in contrast to the on disk open loops. Our datasets are linked to polar coronal holes, this study should be extended to other polar regions that are not linked with coronal holes and one should calculate the power-law indices. This may shed new light on the possible influence of the magnetic topology on wave propagation and dissipation.

Impulsive heating by nanoflares (Parker 1988) is one of the accepted mechanism of coronal heating. It is estimated that nanoflares would cause intensity variations of time scale 15-20 s.. High Resolution Coronal Imager (Hi-C) (Kobayashi *et al.* 2014) provided unprecedented details of active region moss at small spatial scales. We have filtered the images and these filtered images enabled us to see the finer structures compared to the original images. We have concentrated at the braided region. We have found periodic intensity variation with 30-60s. time period, which may be due to plasma flows due to repeated reconnection or may be due to magnetoacoustic wave. We also find repeated plasma flows of velocities 13 km s^{-1} - 185 km s^{-1} in this region, which is a signature of repeated reconnection occurring in this region. Presence of short period waves in the active region were predicted (McIntosh *et al.* 2011). We have confirmed the presence of large amplitude ($\sim$ 8–11 km s^{-1}) high frequency ($\sim$53–73 s) transverse waves in braided magnetic region. These high frequency dynamics could contribute significantly to the energy balance of the moss regions within active region. Our observations were limited to a short duration rocket flight. Future space observations will hopefully be able to confirm our findings. One also need to perform statistical study on these kind of high frequency wave mode identifications for a better estimate on the energetics.

In our next topic we have studied the eruption of a prominence. We have reported and analysed twisting/untwisting motions during and after a prominence eruption. We have observed that small scale twist of prominence footpoint. We have shown that anticlockwise twist of both the footpoints propagated along the spine and induced large scale twist. This lead to eruption of the prominence. We have also reported swirling motion after the prominence eruption and estimated the speed of plasma along different channels. The swirling motion can be considered as a signature of release of the magnetic twist which was built up before the prominence eruption. We have also found that a large amount of twist is transferred to the CME. In this study we have shown the possible magnetic energy transfer through different layers of solar atmosphere. The small scale twist which might be due to photospheric rotations induced large scale roll motion of the prominence spine and lead to the eruption of the prominence. The magnetic twist is then transferred to CME. Prominence seismology can provide informations about different parameters of prominence. The observed swirling and twisting motions can be further explored in this direction. A combination of EUV imaging and coronagraphic images have

allowed us to study the evolution of the prominence eruption at different stages, but it was realised that a co-spatial and co-temporal spectroscopic observation may provide further insight on the evolution and such a study should be attempted in future.

Bibliography

Antiochos, S. K., 1998, "The Magnetic Topology of Solar Eruptions", *Astrophys. J. Lett.*, **502**, L181–L184. [DOI], [ADS], [astro-ph/9806030]

Antiochos, S. K., DeVore, C. R. and Klimchuk, J. A., 1999, "A Model for Solar Coronal Mass Ejections", *Astrophys. J.*, **510**, 485–493. [DOI], [ADS], [astro-ph/9807220]

Antiochos, S. K., Karpen, J. T., DeLuca, E. E., Golub, L. and Hamilton, P., 2003, "Constraints on Active Region Coronal Heating", *Astrophys. J.*, **590**, 547–553. [DOI], [ADS]

Banerjee, D., O'Shea, E. and Doyle, J. G., 2000, "Giant macro-spicule as observed by CDS on SOHO", *Astron. Astrophys.*, **355**, 1152–1159. [ADS]

Banerjee, D., O'Shea, E., Doyle, J. G. and Goossens, M., 2001, "The nature of network oscillations", *Astron. Astrophys.*, **371**, 1137–1149. [DOI], [ADS]

Banerjee, D., Teriaca, L., Gupta, G. R., Imada, S., Stenborg, G. and Solanki, S. K., 2009, "Propagating waves in polar coronal holes as seen by SUMER/EIS", *Astron. Astrophys.*, **499**, L29–L32. [DOI], [ADS], [arXiv:0905.1013 [astro-ph.SR]]

Berghmans, D. and Clette, F., 1999, "Active region EUV transient brightenings - First Results by EIT of SOHO JOP80", *Solar Phys.*, **186**, 207–229. [DOI], [ADS]

Brooks, D. H. and Warren, H. P., 2009, "Flows and Motions in Moss in the Core of a Flaring Active Region: Evidence for Steady Heating", *Astrophys. J. Lett.*, **703**, L10–L13. [DOI], [ADS], [arXiv:0905.3462 [astro-ph.SR]]

Cargill, P. J. and Klimchuk, J. A., 2004, "Nanoflare Heating of the Corona Revisited", *Astrophys. J.*, **605**, 911–920. [DOI], [ADS]

Chen, P. F., 2011, "Coronal Mass Ejections: Models and Their Observational Basis", *Living Reviews in Solar Physics*, **8**. [DOI], [ADS]

Cirtain, J. W., Golub, L., Winebarger, A. R., de Pontieu, B., Kobayashi, K., Moore, R. L., Walsh, R. W., Korreck, K. E., Weber, M., McCauley, P., Title, A., Kuzin, S. and Deforest, C. E., 2013, "Energy release in the solar corona from spatially resolved magnetic braids", *Nature*, **493**, 501–503. [DOI], [ADS]

Datta, A., Krishna Prasad, S. and Banerjee, D., 2015, "Propagating disturbances along a coronal loop from simultaneous EUV imaging and spectroscopic observations", *Research in Astronomy and Astrophysics*, **15**, 1027. [DOI], [ADS]

De Moortel, I., 2008, "Coronal Seismology", in *European Solar Physics Meeting*, (Ed.) Peter, H., European Solar Physics Meeting, 12, [ADS]

de Moortel, I., 2009, "Longitudinal Waves in Coronal Loops", *Space Sci. Rev.*, **149**, 65–81. [DOI], [ADS]

De Moortel, I. and Hood, A. W., 2003, "The damping of slow MHD waves in solar coronal magnetic fields", *Astron. Astrophys.*, **408**, 755–765. [DOI], [ADS]

De Moortel, I. and Hood, A. W., 2004, "The damping of slow MHD waves in solar coronal magnetic fields. II. The effect of gravitational stratification and field line divergence", *Astron. Astrophys.*, **415**, 705–715. [DOI], [ADS]

De Moortel, I. and Nakariakov, V. M., 2012, "Magnetohydrodynamic waves and coronal seismology: an overview of recent results", *Royal Society of London Philosophical Transactions Series A*, **370**, 3193–3216. [DOI], [ADS], [arXiv:1202.1944 [astro-ph.SR]]

De Moortel, I., Ireland, J. and Walsh, R. W., 2000, "Observation of oscillations in coronal loops", *Astron. Astrophys.*, **355**, L23–L26. [ADS]

De Moortel, I., Ireland, J., Hood, A. W. and Walsh, R. W., 2002, "The detection of 3 & 5 min period oscillations in coronal loops", *Astron. Astrophys.*, **387**, L13–L16. [DOI], [ADS]

De Moortel, I., Antolin, P. and Van Doorsselaere, T., 2015, "Observational Signatures of Waves and Flows in the Solar Corona", *Solar Phys.*, **290**, 399–421. [DOI], [ADS], [arXiv:1510.01030 [astro-ph.SR]]

De Pontieu, B. and McIntosh, S. W., 2010, "Quasi-periodic Propagating Signals in the Solar Corona: The Signature of Magnetoacoustic Waves or High-velocity Upflows?", *Astrophys. J.*, **722**, 1013–1029. [DOI], [ADS], [arXiv:1008.5300 [astro-ph.SR]]

De Pontieu, B., Title, A. M., Lemen, J. R., Kushner, G. D., Akin, D. J., Allard, B., Berger, T., Boerner, P., Cheung, M., Chou, C., Drake, J. F., Duncan, D. W., Freeland, S., Heyman, G. F., Hoffman, C., Hurlburt, N. E., Lindgren, R. W., Mathur, D., Rehse, R., Sabolish, D., Seguin, R., Schrijver, C. J., Tarbell, T. D., Wülser, J.-P., Wolfson, C. J., Yanari, C., Mudge, J., Nguyen-Phuc, N., Timmons, R., van Bezooijen, R., Weingrod, I., Brookner, R., Butcher, G., Dougherty, B., Eder, J., Knagenhjelm, V., Larsen, S., Mansir, D., Phan, L., Boyle, P., Cheimets, P. N., DeLuca, E. E., Golub, L., Gates, R., Hertz, E., McKillop, S., Park, S., Perry, T., Podgorski, W. A., Reeves, K., Saar, S., Testa, P., Tian, H., Weber, M., Dunn, C., Eccles, S., Jaeggli, S. A., Kankelborg, C. C., Mashburn, K., Pust, N., Springer, L., Carvalho, R., Kleint, L., Marmie, J., Mazmanian, E., Pereira, T. M. D., Sawyer, S., Strong, J., Worden, S. P., Carlsson, M., Hansteen, V. H., Leenaarts, J., Wiesmann, M., Aloise, J., Chu, K.-C., Bush, R. I., Scherrer, P. H., Brekke, P., Martinez-Sykora, J., Lites, B. W., McIntosh, S. W., Uitenbroek, H., Okamoto, T. J., Gummin, M. A., Auker, G., Jerram, P., Pool, P. and Waltham, N., 2014, "The Interface Region Imaging Spectrograph (IRIS)", *Solar Phys.*, **289**, 2733–2779. [DOI], [ADS], [arXiv:1401.2491 [astro-ph.SR]]

Deforest, C. E. and Gurman, J. B., 1998, "Observation of Quasi-periodic Compressive Waves in Solar Polar Plumes", *Astrophys. J. Lett.*, **501**, L217. [DOI], [ADS]

Del Zanna, G., 2003, "Solar active regions: The footpoints of 1 MK loops", *Astron. Astrophys.*, **406**, L5–L8. [DOI], [ADS]

Fan, Y., 2010, "On the Eruption of Coronal Flux Ropes", *Astrophys. J.*, **719**, 728–736. [DOI], [ADS]

Fan, Y. and Gibson, S. E., 2003, "The Emergence of a Twisted Magnetic Flux Tube into a Preexisting Coronal Arcade", *Astrophys. J. Lett.*, **589**, L105–L108. [DOI], [ADS]

Fan, Y. and Gibson, S. E., 2007, "Onset of Coronal Mass Ejections Due to Loss of Confinement of Coronal Flux Ropes", *Astrophys. J.*, **668**, 1232–1245. [DOI], [ADS]

Filippov, B., Martsenyuk, O., Srivastava, A. K. and Uddin, W., 2015, "Solar Magnetic Flux Ropes", *Journal of Astrophysics and Astronomy*. [DOI], [ADS], [arXiv:1501.02562 [astro-ph.SR]]

Gibson, S. E., Foster, D., Burkepile, J., de Toma, G. and Stanger, A., 2006, "The Calm before the Storm: The Link between Quiescent Cavities and Coronal Mass Ejections", *Astrophys. J.*, **641**, 590–605. [DOI], [ADS]

Gopalswamy, N., Mikić, Z., Maia, D., Alexander, D., Cremades, H., Kaufmann, P., Tripathi, D. and Wang, Y.-M., 2006, "The Pre-CME Sun", *Space Sci. Rev.*, **123**, 303–339. [DOI], [ADS]

Gupta, G. R., 2014, "Observations of dissipation of slow magneto-acoustic waves in a polar coronal hole", *Astron. Astrophys.*, **568**, A96. [DOI], [ADS], [arXiv:1407.1017 [astro-ph.SR]]

Gupta, G. R., Teriaca, L., Marsch, E., Solanki, S. K. and Banerjee, D., 2012, "Spectroscopic observations of propagating disturbances in a polar coronal hole: evidence of slow magneto-acoustic waves", *Astron. Astrophys.*, **546**, A93. [DOI], [ADS], [arXiv:1209.3524 [astro-ph.SR]]

Handy, B. N., Acton, L. W., Kankelborg, C. C., Wolfson, C. J., Akin, D. J., Bruner, M. E., Caravalho, R., Catura, R. C., Chevalier, R., Duncan, D. W., Edwards, C. G., Feinstein, C. N., Freeland, S. L., Friedlaender, F. M., Hoffmann, C. H., Hurlburt, N. E., Jurcevich, B. K., Katz, N. L., Kelly, G. A., Lemen, J. R., Levay, M., Lindgren, R. W., Mathur, D. P., Meyer, S. B., Morrison, S. J., Morrison, M. D., Nightingale, R. W., Pope, T. P., Rehse, R. A., Schrijver, C. J., Shine, R. A., Shing, L., Strong, K. T., Tarbell, T. D., Title, A. M., Torgerson, D. D., Golub, L., Bookbinder, J. A., Caldwell, D., Cheimets, P. N., Davis, W. N., Deluca, E. E., McMullen, R. A., Warren, H. P., Amato, D., Fisher, R., Maldonado, H. and Parkinson, C., 1999, "The transition region and coronal explorer", *Solar Phys.*, **187**, 229–260. [DOI], [ADS]

Harrison, R. A., Sawyer, E. C., Carter, M. K., Cruise, A. M., Cutler, R. M., Fludra, A., Hayes, R. W., Kent, B. J., Lang, J., Parker, D. J., Payne, J., Pike, C. D.,

Peskett, S. C., Richards, A. G., Gulhane, J. L., Norman, K., Breeveld, A. A., Breeveld, E. R., Al Janabi, K. F., McCalden, A. J., Parkinson, J. H., Self, D. G., Thomas, P. D., Poland, A. I., Thomas, R. J., Thompson, W. T., Kjeldseth-Moe, O., Brekke, P., Karud, J., Maltby, P., Aschenbach, B., Bräuninger, H., Kühne, M., Hollandt, J., Siegmund, O. H. W., Huber, M. C. E., Gabriel, A. H., Mason, H. E. and Bromage, B. J. I., 1995, "The Coronal Diagnostic Spectrometer for the Solar and Heliospheric Observatory", *Solar Phys.*, **162**, 233–290. [DOI], [ADS]

Hood, A. W. and Priest, E. R., 1981, "Critical conditions for magnetic instabilities in force-free coronal loops", *Geophysical and Astrophysical Fluid Dynamics*, **17**, 297–318. [DOI], [ADS]

House, L. L., Wagner, W. J., Hildner, E., Sawyer, C. and Schmidt, H. U., 1981, "Studies of the corona with the Solar Maximum Mission coronagraph/polarimeter", *Astrophys. J. Lett.*, **244**, L117–L121. [DOI], [ADS]

Illing, R. M. E. and Hundhausen, A. J., 1985, "Observation of a coronal transient from 1.2 to 6 solar radii", *J. Geophys. Res.*, **90**, 275–282. [DOI], [ADS]

Ionson, J. A., 1978, "Resonant absorption of Alfvenic surface waves and the heating of solar coronal loops", *Astrophys. J.*, **226**, 650–673. [DOI], [ADS]

Kiddie, G., De Moortel, I., Del Zanna, G., McIntosh, S. W. and Whittaker, I., 2012, "Propagating Disturbances in Coronal Loops: A Detailed Analysis of Propagation Speeds", *Solar Phys.*, **279**, 427–452. [DOI], [ADS], [arXiv:1205.0891 [astro-ph.SR]]

Kliem, B. and Török, T., 2006, "Torus Instability", *Physical Review Letters*, **96**(25), 255002. [DOI], [ADS], [physics/0605217]

Kliem, B., Török, T. and Thompson, W. T., 2012, "A Parametric Study of Erupting Flux Rope Rotation. Modeling the "Cartwheel CME" on 9 April 2008", *Solar Phys.*, **281**, 137–166. [DOI], [ADS], [arXiv:1112.3389 [astro-ph.SR]]

Kobayashi, K., Cirtain, J., Winebarger, A. R., Korreck, K., Golub, L., Walsh, R. W., De Pontieu, B., DeForest, C., Title, A., Kuzin, S., Savage, S., Beabout, D., Beabout, B., Podgorski, W., Caldwell, D., McCracken, K., Ordway, M., Bergner, H., Gates, R., McKillop, S., Cheimets, P., Platt, S., Mitchell, N. and

Windt, D., 2014, "The High-Resolution Coronal Imager (Hi-C)", *Solar Phys.*, **289**, 4393–4412. [DOI], [ADS]

Krishna Prasad, S., Banerjee, D. and Gupta, G. R., 2011, "Propagating intensity disturbances in polar corona as seen from AIA/SDO", *Astron. Astrophys.*, **528**, L4. [DOI], [ADS], [arXiv:1102.2979 [astro-ph.SR]]

Krishna Prasad, S., Banerjee, D. and Singh, J., 2012a, "Oscillations in Active Region Fan Loops: Observations from EIS/ Hinode and AIA/SDO", *Solar Phys.*, **281**, 67–85. [DOI], [ADS], [arXiv:1208.1377 [astro-ph.SR]]

Krishna Prasad, S., Banerjee, D., Van Doorsselaere, T. and Singh, J., 2012b, "Omnipresent long-period intensity oscillations in open coronal structures", *Astron. Astrophys.*, **546**, A50. [DOI], [ADS], [arXiv:1209.2536 [astro-ph.SR]]

Krishna Prasad, S., Banerjee, D. and Van Doorsselaere, T., 2014, "Frequency-dependent Damping in Propagating Slow Magneto-acoustic Waves", *Astrophys. J.*, **789**, 118. [DOI], [ADS], [arXiv:1406.3565 [astro-ph.SR]]

Labrosse, N., Heinzel, P., Vial, J.-C., Kucera, T., Parenti, S., Gunár, S., Schmieder, B. and Kilper, G., 2010, "Physics of Solar Prominences: I-Spectral Diagnostics and Non-LTE Modelling", *Space Sci. Rev.*, **151**, 243–332. [DOI], [ADS], [arXiv:1001.1620 [astro-ph.SR]]

Lemen, J. R., Title, A. M., Akin, D. J., Boerner, P. F., Chou, C., Drake, J. F., Duncan, D. W., Edwards, C. G., Friedlaender, F. M., Heyman, G. F., Hurlburt, N. E., Katz, N. L., Kushner, G. D., Levay, M., Lindgren, R. W., Mathur, D. P., McFeaters, E. L., Mitchell, S., Rehse, R. A., Schrijver, C. J., Springer, L. A., Stern, R. A., Tarbell, T. D., Wuelser, J.-P., Wolfson, C. J., Yanari, C., Bookbinder, J. A., Cheimets, P. N., Caldwell, D., Deluca, E. E., Gates, R., Golub, L., Park, S., Podgorski, W. A., Bush, R. I., Scherrer, P. H., Gummin, M. A., Smith, P., Auker, G., Jerram, P., Pool, P., Soufli, R., Windt, D. L., Beardsley, S., Clapp, M., Lang, J. and Waltham, N., 2012, "The Atmospheric Imaging Assembly (AIA) on the Solar Dynamics Observatory (SDO)", *Solar Phys.*, **275**, 17–40. [DOI], [ADS]

Li, X., Morgan, H., Leonard, D. and Jeska, L., 2012, "A Solar Tornado Observed by AIA/SDO: Rotational Flow and Evolution of Magnetic Helicity in a Prominence

and Cavity", *Astrophys. J. Lett.*, **752**, L22. [DOI], [ADS], [arXiv:1205.3819 [astro-ph.SR]]

Lin, H., Penn, M. J. and Kuhn, J. R., 1998, "He i 10830 Angstrom Line Polarimetry: A New Tool to Probe the Filament Magnetic Fields", *Astrophys. J.*, **493**, 978–995. [DOI], [ADS]

Lin, Y., 2011, "Filament Thread-like Structures and Their Small-amplitude Oscillations", *Space Sci. Rev.*, **158**, 237–266. [DOI], [ADS]

Lin, Y., Soler, R., Engvold, O., Ballester, J. L., Langangen, Ø., Oliver, R. and Rouppe van der Voort, L. H. M., 2009, "Swaying Threads of a Solar Filament", *Astrophys. J.*, **704**, 870–876. [DOI], [ADS], [arXiv:0909.2792 [astro-ph.SR]]

Mackay, D. H., Karpen, J. T., Ballester, J. L., Schmieder, B. and Aulanier, G., 2010, "Physics of Solar Prominences: II-Magnetic Structure and Dynamics", *Space Sci. Rev.*, **151**, 333–399. [DOI], [ADS], [arXiv:1001.1635 [astro-ph.SR]]

Mandal, S., Magyar, N., Yuan, D., Van Doorsselaere, T. and Banerjee, D., 2016, "Forward Modeling of Propagating Slow Waves in Coronal Loops and Their Frequency-dependent Damping", *Astrophys. J.*, **820**, 13. [DOI], [ADS], [arXiv:1602.00787 [astro-ph.SR]]

Marsh, M. S., Walsh, R. W., De Moortel, I. and Ireland, J., 2003, "Joint observations of propagating oscillations with SOHO/CDS and TRACE", *Astron. Astrophys.*, **404**, L37–L41. [DOI], [ADS]

Marsh, M. S., Walsh, R. W., De Moortel, I. and Ireland, J., 2004, "Longitudinal Oscillations in Coronal Loops - Joint Observations with SOHO/CDS and TRACE", in *SOHO 13 Waves, Oscillations and Small-Scale Transients Events in the Solar Atmosphere: Joint View from SOHO and TRACE*, (Ed.) Lacoste, H., ESA Special Publication, 547, [ADS]

Martin, S. F., 1980, "Preflare conditions, changes and events", *Solar Phys.*, **68**, 217–236. [DOI], [ADS]

McIntosh, S. W., de Pontieu, B., Carlsson, M., Hansteen, V., Boerner, P. and Goossens, M., 2011, "Alfvénic waves with sufficient energy to power the quiet solar corona and fast solar wind", *Nature*, **475**, 477–480. [DOI], [ADS]

Mghebrishvili, I., Zaqarashvili, T. V., Kukhianidze, V., Ramishvili, G., Shergelashvili, B., Veronig, A. and Poedts, S., 2015, "Dynamics of a Solar Prominence Tornado Observed by SDO/AIA on November 7-8, 2012", *Astrophys. J.*, **810**, 89. [DOI], [ADS], [arXiv:1508.06788 [astro-ph.SR]]

Moore, R. L. and Labonte, B. J., 1980, "The filament eruption in the 3B flare of July 29, 1973 - Onset and magnetic field configuration", in *Solar and Interplanetary Dynamics*, (Eds.) Dryer, M., Tandberg-Hanssen, E., IAU Symposium, 91, [ADS]

Moore, R. L., Sterling, A. C., Hudson, H. S. and Lemen, J. R., 2001, "Onset of the Magnetic Explosion in Solar Flares and Coronal Mass Ejections", *Astrophys. J.*, **552**, 833–848. [DOI], [ADS]

Morgan, H. and Druckmüller, M., 2014, "Multi-Scale Gaussian Normalization for Solar Image Processing", *Solar Phys.*, **289**, 2945–2955. [DOI], [ADS], [arXiv:1403.6613 [astro-ph.SR]]

Morton, R. J. and McLaughlin, J. A., 2013, "Hi-C and AIA observations of transverse magnetohydrodynamic waves in active regions", *Astron. Astrophys.*, **553**, L10. [DOI], [ADS], [arXiv:1305.0140 [astro-ph.SR]]

Morton, R. J. and McLaughlin, J. A., 2014, "High-resolution Observations of Active Region Moss and its Dynamics", *Astrophys. J.*, **789**, 105. [DOI], [ADS], [arXiv:1405.5694 [astro-ph.SR]]

Nakariakov, V. M. and Verwichte, E., 2005, "Coronal Waves and Oscillations", *Living Rev. Solar Phys.*, **2**, 3–+URL: http://www.livingreviews.org/lrsp-2005-3

Nishizuka, N. and Hara, H., 2011, "Spectroscopic Observations of Continuous Outflows and Propagating Waves from NOAA 10942 with Extreme Ultraviolet Imaging Spectrometer/Hinode", *Astrophys. J. Lett.*, **737**, L43. [DOI], [ADS]

Ofman, L., Romoli, M., Poletto, G., Noci, G. and Kohl, J. L., 1997, "Ultraviolet Coronagraph Spectrometer Observations of Density Fluctuations in the Solar Wind", *Astrophys. J. Lett.*, **491**, L111. [DOI], [ADS]

Ofman, L., Nakariakov, V. M. and Deforest, C. E., 1999, "Slow Magnetosonic Waves in Coronal Plumes", *Astrophys. J.*, **514**, 441–447. [DOI], [ADS]

Ofman, L., Wang, T. J. and Davila, J. M., 2012, "Slow Magnetosonic Waves and Fast Flows in Active Region Loops", *Astrophys. J.*, **754**, 111. [DOI], [ADS], [arXiv:1205.5732 [astro-ph.SR]]

Okamoto, T. J., Tsuneta, S., Berger, T. E., Ichimoto, K., Katsukawa, Y., Lites, B. W., Nagata, S., Shibata, K., Shimizu, T., Shine, R. A., Suematsu, Y., Tarbell, T. D. and Title, A. M., 2007, "Coronal Transverse Magnetohydrodynamic Waves in a Solar Prominence", *Science*, **318**, 1577–. [DOI], [ADS], [arXiv:0801.1958]

Okamoto, T. J., Liu, W. and Tsuneta, S., 2016, "Helical motions of fine-structure prominence threads observed by Hinode and IRIS", *ArXiv e-prints*. [ADS], [arXiv:1608.00123 [astro-ph.SR]]

O'Shea, E. and Doyle, J. G., 2009, "On oscillations found in an active region with EIS on Hinode", *Astron. Astrophys.*, **494**, 355–360. [DOI], [ADS]

O'Shea, E., Muglach, K. and Fleck, B., 2002, "Oscillations above sunspots: Evidence for propagating waves?", *Astron. Astrophys.*, **387**, 642–664. [DOI], [ADS]

Paletou, F., López Ariste, A., Bommier, V. and Semel, M., 2001, "Full-Stokes spectropolarimetry of solar prominences", *Astron. Astrophys.*, **375**, L39–L42. [DOI], [ADS]

Panasenco, O., Martin, S. F., Velli, M. and Vourlidas, A., 2013, "Origins of Rolling, Twisting, and Non-radial Propagation of Eruptive Solar Events", *Solar Phys.*, **287**, 391–413. [DOI], [ADS], [arXiv:1211.1376 [astro-ph.SR]]

Panasenco, O., Martin, S. F. and Velli, M., 2014, "Apparent Solar Tornado-Like Prominences", *Solar Phys.*, **289**, 603–622. [DOI], [ADS], [arXiv:1307.2303 [astro-ph.SR]]

Pant, V., Datta, A. and Banerjee, D., 2015, "Flows and Waves in Braided Solar Coronal Magnetic Structures", *Astrophys. J. Lett.*, **801**, L2. [DOI], [ADS], [arXiv:1501.06507 [astro-ph.SR]]

Parenti, S., 2014, "Solar Prominences: Observations", *Living Reviews in Solar Physics*, **11**, 1. [DOI], [ADS]

Parker, E. N., 1988, "Nanoflares and the solar X-ray corona", *Astrophys. J.*, **330**, 474–479. [DOI], [ADS]

Pasachoff, J. M. and Landman, D. A., 1984, "High-frequency coronal oscillations and coronal heating", *Solar Phys.*, **90**, 325–330. [DOI], [ADS]

Patsourakos, S. and Vourlidas, A., 2011, "Evidence for a current sheet forming in the wake of a coronal mass ejection from multi-viewpoint coronagraph observations", *Astron. Astrophys.*, **525**, A27. [DOI], [ADS], [arXiv:1010.0323 [astro-ph.SR]]

Pesnell, W. D., Thompson, B. J. and Chamberlin, P. C., 2012, "The Solar Dynamics Observatory (SDO)", *Solar Phys.*, **275**, 3–15. [DOI], [ADS]

Peter, H., Bingert, S., Klimchuk, J. A., de Forest, C., Cirtain, J. W., Golub, L., Winebarger, A. R., Kobayashi, K. and Korreck, K. E., 2013, "Structure of solar coronal loops: from miniature to large-scale", *Astron. Astrophys.*, **556**, A104. [DOI], [ADS], [arXiv:1306.4685 [astro-ph.SR]]

Porter, L. J., Klimchuk, J. A. and Sturrock, P. A., 1994, "The possible role of MHD waves in heating the solar corona", *Astrophys. J.*, **435**, 482–501. [DOI], [ADS]

Priest, E. R., 1984, *Solar magneto-hydrodynamics*. [ADS]

Reeves, K. K., Gibson, S. E., Kucera, T. A., Hudson, H. S. and Kano, R., 2012, "Thermal Properties of a Solar Coronal Cavity Observed with the X-Ray Telescope on Hinode", *Astrophys. J.*, **746**, 146. [DOI], [ADS]

Régnier, S., Alexander, C. E., Walsh, R. W., Winebarger, A. R., Cirtain, J., Golub, L., Korreck, K. E., Mitchell, N., Platt, S., Weber, M., De Pontieu, B., Title, A., Kobayashi, K., Kuzin, S. and DeForest, C. E., 2014, "Sparkling Extreme-ultraviolet Bright Dots Observed with Hi-C", *Astrophys. J.*, **784**, 134. [DOI], [ADS], [arXiv:1402.2457 [astro-ph.SR]]

Roberts, B., Edwin, P. M. and Benz, A. O., 1984, "On coronal oscillations", *Astrophys. J.*, **279**, 857–865. [DOI], [ADS]

Singh, J., Cowsik, R., Raveendran, A. V., Bagare, S. P., Saxena, A. K., Sundararaman, K., Krishan, V., Naidu, N., Samson, J. P. A. and Gabriel, F., 1997, "Detection of Short-Period Coronal Oscillations during the Total Solar Eclipse of 24 October, 1995", *Solar Phys.*, **170**, 235–252. [ADS]

Singh, J., Hasan, S. S., Gupta, G. R., Banerjee, D., Muneer, S., Raju, K. P., Bagare, S. P. and Srinivasan, R., 2009, "Intensity Oscillation in the Corona as Observed during the Total Solar Eclipse of 29 March 2006", *Solar Phys.*, **260**, 125–134. [DOI], [ADS]

Su, J. T., Liu, Y., Liu, S., Zhang, Y. Z., Zhao, H., Xu, H. Q. and Xie, W. B., 2013, "Simultaneous Observation of Solar Oscillations Associated with Coronal Loops from the Photosphere to the Corona", *Astrophys. J.*, **762**, 42. [DOI], [ADS]

Su, Y., Wang, T., Veronig, A., Temmer, M. and Gan, W., 2012, "Solar Magnetized "Tornadoes:" Relation to Filaments", *Astrophys. J. Lett.*, **756**, L41. [DOI], [ADS], [arXiv:1208.0138 [astro-ph.SR]]

Su, Y., Gömöry, P., Veronig, A., Temmer, M., Wang, T., Vanninathan, K., Gan, W. and Li, Y., 2014, "Solar Magnetized Tornadoes: Rotational Motion in a Tornado-like Prominence", *Astrophys. J. Lett.*, **785**, L2. [DOI], [ADS], [arXiv:1312.5226 [astro-ph.SR]]

Testa, P., De Pontieu, B., Martínez-Sykora, J., DeLuca, E., Hansteen, V., Cirtain, J., Winebarger, A., Golub, L., Kobayashi, K., Korreck, K., Kuzin, S., Walsh, R., DeForest, C., Title, A. and Weber, M., 2013, "Observing Coronal Nanoflares in Active Region Moss", *Astrophys. J. Lett.*, **770**, L1. [DOI], [ADS], [arXiv:1305.1687 [astro-ph.SR]]

Thalmann, J. K., Tiwari, S. K. and Wiegelmann, T., 2014, "Force-free Field Modeling of Twist and Braiding-induced Magnetic Energy in an Active-region Corona", *Astrophys. J.*, **780**, 102. [DOI], [ADS], [arXiv:1311.3413 [astro-ph.SR]]

Thompson, W. T., Kliem, B. and Török, T., 2012, "3D Reconstruction of a Rotating Erupting Prominence", *Solar Phys.*, **276**, 241–259. [DOI], [ADS], [arXiv:1112.3388 [astro-ph.SR]]

Tian, H., McIntosh, S. W. and De Pontieu, B., 2011, "The Spectroscopic Signature of Quasi-periodic Upflows in Active Region Timeseries", *Astrophys. J. Lett.*, **727**, L37. [DOI], [ADS], [arXiv:1012.5112 [astro-ph.SR]]

Tiwari, S. K., Alexander, C. E., Winebarger, A. R. and Moore, R. L., 2014, "Trigger Mechanism of Solar Subflares in a Braided Coronal Magnetic Structure", *Astrophys. J. Lett.*, **795**, L24. [DOI], [ADS], [arXiv:1410.4260 [astro-ph.SR]]

Tomczyk, S., McIntosh, S. W., Keil, S. L., Judge, P. G., Schad, T., Seeley, D. H. and Edmondson, J., 2007, "Alfvén Waves in the Solar Corona", *Science*, **317**, 1192. [DOI], [ADS]

Török, T. and Kliem, B., 2003, "The evolution of twisting coronal magnetic flux tubes", *Astron. Astrophys.*, **406**, 1043–1059. [DOI], [ADS]

Török, T. and Kliem, B., 2005, "Confined and Ejective Eruptions of Kink-unstable Flux Ropes", *Astrophys. J. Lett.*, **630**, L97–L100. [DOI], [ADS], [astro-ph/0507662]

Torrence, C. and Compo, G. P., 1998, "A Practical Guide to Wavelet Analysis.", *Bulletin of the American Meteorological Society*, **79**, 61–78. [DOI], [ADS]

Uchida, Y., 1970, "Diagnosis of Coronal Magnetic Structure by Flare-Associated Hydromagnetic Disturbances", *Pub. Astron. Soc. Japan*, **22**, 341. [ADS]

Verwichte, E., Marsh, M., Foullon, C., Van Doorsselaere, T., De Moortel, I., Hood, A. W. and Nakariakov, V. M., 2010, "Periodic Spectral Line Asymmetries in Solar Coronal Structures from Slow Magnetoacoustic Waves", *Astrophys. J. Lett.*, **724**, L194–L198. [DOI], [ADS]

Wang, T., Ofman, L. and Davila, J. M., 2012, "Propagating Intensity Disturbances in Fan-like Coronal Loops: Flows or Waves?", in *4th Hinode Science Meeting: Unsolved Problems and Recent Insights*, (Eds.) Bellot Rubio, L., Reale, F., Carlsson, M., Astronomical Society of the Pacific Conference Series, 455, [ADS], [arXiv:1101.6017 [astro-ph.SR]]

Wang, T., Ofman, L. and Davila, J. M., 2013, "Three-dimensional Magnetohydrodynamic Modeling of Propagating Disturbances in Fan-like Coronal Loops", *Astrophys. J. Lett.*, **775**, L23. [DOI], [ADS], [arXiv:1308.0282 [astro-ph.SR]]

Wang, T. J., Ofman, L. and Davila, J. M., 2009a, "Propagating Slow Magnetoacoustic Waves in Coronal Loops Observed by Hinode/EIS", *Astrophys. J.*, **696**, 1448–1460. [DOI], [ADS], [arXiv:0902.4480 [astro-ph.SR]]

Wang, T. J., Ofman, L., Davila, J. M. and Mariska, J. T., 2009b, "Hinode/EIS observations of propagating low-frequency slow magnetoacoustic waves in fan-like coronal loops", *Astron. Astrophys.*, **503**, L25–L28. [DOI], [ADS], [arXiv:0908.0310 [astro-ph.SR]]

Wedemeyer, S., Scullion, E., Rouppe van der Voort, L., Bosnjak, A. and Antolin, P., 2013, "Are Giant Tornadoes the Legs of Solar Prominences?", *Astrophys. J.*, **774**, 123. [DOI], [ADS], [arXiv:1306.2661 [astro-ph.SR]]

Wedemeyer-Böhm, S. and Rouppe van der Voort, L., 2009, "Small-scale swirl events in the quiet Sun chromosphere", *Astron. Astrophys.*, **507**, L9–L12. [DOI], [ADS], [arXiv:0910.2226 [astro-ph.SR]]

Wedemeyer-Böhm, S., Scullion, E., Steiner, O., Rouppe van der Voort, L., de La Cruz Rodriguez, J., Fedun, V. and Erdélyi, R., 2012, "Magnetic tornadoes as energy channels into the solar corona", *Nature*, **486**, 505–508. [DOI], [ADS]

Wilhelm, K., 2006, "Solar coronal-hole plasma densities and temperatures", *Astron. Astrophys.*, **455**, 697–708. [DOI], [ADS]

Winebarger, A. R., Walsh, R. W., Moore, R., De Pontieu, B., Hansteen, V., Cirtain, J., Golub, L., Kobayashi, K., Korreck, K., DeForest, C., Weber, M., Title, A. and Kuzin, S., 2013, "Detecting Nanoflare Heating Events in Subarcsecond Inter-moss Loops Using Hi-C", *Astrophys. J.*, **771**, 21. [DOI], [ADS]

Winebarger, A. R., Cirtain, J., Golub, L., DeLuca, E., Savage, S., Alexander, C. and Schuler, T., 2014, "Discovery of Finely Structured Dynamic Solar Corona Observed in the Hi-C Telescope", *Astrophys. J. Lett.*, **787**, L10. [DOI], [ADS]

Xia, C., Keppens, R., Antolin, P. and Porth, O., 2014, "Simulating the in Situ Condensation Process of Solar Prominences", *Astrophys. J. Lett.*, **792**, L38. [DOI], [ADS], [arXiv:1408.4249 [astro-ph.SR]]

Yan, X. L., Xue, Z. K., Liu, J. H., Kong, D. F. and Xu, C. L., 2014, "Unwinding Motion of a Twisted Active Region Filament", *Astrophys. J.*, **797**, 52. [DOI], [ADS], [arXiv:1410.1984 [astro-ph.SR]]

Yashiro, S., Gopalswamy, N., Michalek, G., St. Cyr, O. C., Plunkett, S. P., Rich, N. B. and Howard, R. A., 2004, "A catalog of white light coronal mass ejections observed by the SOHO spacecraft", *Journal of Geophysical Research (Space Physics)*, **109**, A07105. [DOI], [ADS]

Yuan, D. and Nakariakov, V. M., 2012, "Measuring the apparent phase speed of propagating EUV disturbances", *Astron. Astrophys.*, **543**, A9. [DOI], [ADS]